2006

UV-LIGA micro-fabrication of inertia type electrostatic transducers and their application

Seok Jae Jeong
Louisiana State University and Agricultural and Mechanical College, sjeong1@lsu.edu

UV-LIGA MICRO-FABRICATION OF INERTIA TYPE ELECTROSTATIC TRANSDUCERS AND THEIR APPLICATION

A Dissertation

Submitted to the Graduate Faculty of the
Louisiana State University and
Agricultural and Mechanical College
in partial fulfillment of the
requirements for the degree of
Doctor of Philosophy

in

The Department of Mechanical Engineering

by
Seok Jae Jeong
B.S., Chemical Eng., Sungkyunkwan University, 1997
M.S. Chemical Eng., Sungkyunkwan University, 1999
May 2006

To my family

ACKNOWLEDGMENTS

I sincerely thank my advisor and friend, Professor Wanjun Wang, for introducing me to the MEMS field, for giving me priceless advice. This has been one of the most rewarding times of my career. Many thanks also go to my other four thesis committee members, Professor Yitshak Ram, Professor Marcio S. de Queiroz, Professor Elizabeth J. Podlaha-Murphy, and Professor James M. Matthews for reviewing the manuscript, and also to Professor Jin Woo Choi for his helpful discussions. Special thanks also go to Professor Muhammad A. Wahab with whom I worked as a TA and received the Best TA Award of Mechanical Engineering Department in Spring 2005.

I would also like to thank my fellow students and friends: Ren Yang, whose relay research was a starting point for my work, Dong Eun Lee for discussions and helping me test the prototype relay, and Jae Ho Shim for helpful discussions. I also deeply appreciate Dr. Daniel Park's help in dry etching of SU-8 mold for the relay work presented in this dissertation. Device fabrication in this research work was made possible through the efforts of CAMD staff, Yoonyoung Jin, Tracy Morris, Shaloma Malveaux, and the rest of the staff in CAMD.

Finally, I want to thank my parents, my sister and brother, for their love and encouragement during this challenging period of my life.

This research was funded by the National Science Foundation through grant ECS#0104327.

TABLE OF CONTENTS

LIST OF TABLES

LIST OF FIGURES

ABSTRACT

This dissertation discusses the design, working principles, static & dynamic analysis and simulation, mechanics of material, applied MEMS technology, micro-fabrication, and experimental testing of two types of micro-transducers: micro-power relay and micro-accelerometer.

Several possible design concepts were proposed, and the advantages and disadvantages of electrostatic working principles were also discussed. Transducers presented in this research used electrostatic force as a driving force in the micro-relay and capacitance as a sensing parameter in the micro-accelerometer. There was an analogy between the micro-relay and the micro-accelerometer in their theoretical approach and fabrication processes.

The proposed micro-transducers (micro-relay and micro-accelerometer) were fabricated using UV lithograph of SU-8 & SPR and UV-LIGA process. The advantages and disadvantages of these processes were discussed. The micro-relays fabricated by UV-LIGA technology had the following advantages compared with other reported relays: fast switching speed, high power capacity, high off-resistance, lower on-resistance, low power consumption, and low heat generation.

The polymer-based micro-accelerometers were designed and fabricated. Instead of applying SU-8 only as a photo resist, cured SU-8 was used as the primary structural material in fabricating the micro-accelerometers. The great flexibility in size and aspect ratio of cured SU-8 made it feasible to produce highly sensitive accelerometers.

The prototype micro-relays and micro-accelerometers were tested for the dynamic

characteristics and power capacity. The experimental results in micro-relays had confirmed that reasonably large current capacity and fast response speed was able to be achieved using electromagnetic actuation and the multilayer UV-LIGA fabrication process.

CHAPTER 1: INTRODUCTION

1.1 Definition of Transducers: Sensors and Actuators

Transducers are devices that convert one form of energy domain into another. They are energy-conversion devices, and involve at least two energy domains. Typical energy domains are mechanical, electrical, chemical, fluid, thermal, and radiant. Transducers normally measure the physical quantity of interest indirectly through its effect on one of the transducer's parameters, or vice versa. Figure 1-1 illustrates this point.

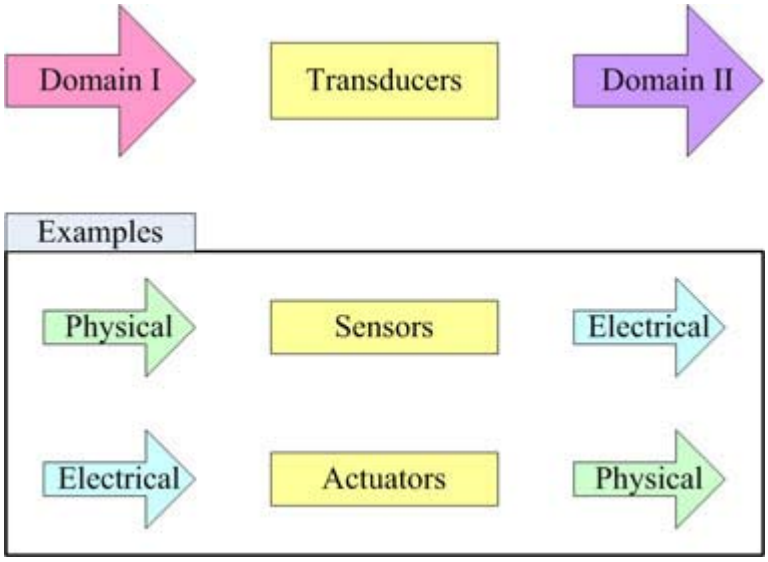

Figure 1-1 Generic view of transducers

Transducers may generally be divided into two classes as shown in Figure 1-1: sensors and actuators. Actuators are devices that impose a state on a system such as force, pressure, fluid velocity, etc. Examples of Microelectromechanical system (MEMS) actuators are relays, motors, pumps, tweezers, and force heads. On the other hand, sensors are devices that monitor a parameter such as acceleration, velocity, position,

pressure, weight, flow rate, force, torque, magnetic field, temperature, sound, gas composition, etc. MEMS sensors are being used in many applications including sophisticated guidance systems, antilock-braking systems, and micro-medical instruments.

1.2 Overview of Micro-transducers: Sensors and Actuators

1.2.1 General Remarks

MEMS field has been one of the fastest developing fields in science and engineering. It may have an impact on our society just as the microelectronics industry has had in the past three decades[1]. The microelectronics revolution brings us to the information age and powerful digital network. However, the physical world we live is an analog one. The MEMS technologies promise to provide us an interface between the digital network and the physical world by making various intelligent sensors and actuators integrated with the microelectronics.

Currently, the overwhelming majority of the MEMS devices have been made with silicon as the structural material by utilizing the technologies developed in microelectronics industry. There are many advantages in using silicon-based MEMS systems and devices. Because being made with silicon based fabrication technologies, they tend to be easy to integrate with the signal processing circuit and can be built on the same substrate[2,3]. From the application point of view, however, most of the silicon-based MEMS devices by microelectronics technology have limitations. For example, the silicon-based MEMS relays cannot be used for applications that require large power capability because they typically have low current capacity, low-off resistance, high on resistance, high power consumption and low dielectric strength[4]. In the case of silicon-

based accelerometers, its out-of-plane dimension is normally limited to about 5 μm and the reduced seismic mass limits the sensitivity. Another disadvantage is the low spring compliance which may result in sticking failure[5].

In this study, in order to overcome these limitations, a new type of micro transducers was studied using UV lithography of SU-8 & SPR and UV-LIGA process. LIGA stems from the German expressions for the major process steps: Lithography, Galvanoformung (electroforming) and Abformung (molding). LIGA micro-fabrication technologies have the unique advantage of producing high aspect-ratio microstructures of polymer, metals, and alloys. It also provides great potential for building microstructures from a broad selection of materials. Any metals or alloys that can be electroplated may be used as a potential candidate material for three-dimensional MEMS structural components[6]. The combination of a broad material selection and the capability of making high aspect ratio microstructures make the technology best suited for fabricating MEMS transducers. Instead of applying SU-8 only as a photo resist, cured SU-8 was used as the structural material in fabricating the MEMS transducers. The great flexibility in size and aspect ratio of cured SU-8 made it feasible to produce truly 3-D and highly sensitive transducers.

1.2.2 Micro-actuators

Since the first micro-machined relay presented by Peterson[7] in 1979, extensive research activities have been done by many groups. The first significant advance on micro-actuators was the development of micro-motors[8]. Micro-motors provide a class of micro-actuators with unrestrained motion in at least one degree of freedom. Polysilicon surface micromachining has provided the fabrication backbone of this class of micro-actuators.

At the same time, there has been increased research on the second class of micro-actuators, which are based on deformable structures. In this class, bulk and surface micromachining of silicon have been used to fabricate a variety of micro-actuators based on suspended micromechanical structures such as beams[9,10], diaphragms[11], and more complex suspensions in single-crystal silicon or in films deposited on a silicon substrate[12]. In conjunction with various actuation mechanisms, these micromechanical structures have formed the basis of a class of micro-actuators, which operate based on flexure; they are generally limited on motion to small deformations since the movable component is physically attached to the substrate.

A number of actuation mechanisms are being studied as well. For example, the volume expansion of a gas upon heating has been used as a source of actuation[13]. Piezoelectric films have been used to provide an actuation in a variety of application such as valves, pumps, positioning devices[14,15], and ultrasonic micro-motors (advantage: considerably low driving voltage)[16]. The Meissner effect of a superconductor has been used to develop a linear micro-actuator[17]. In this dissertation, the novel design of micro power relays based on the electrostatic actuation as well as a multi-layer, multi-step UV-LIGA process was studied as an example of micro-actuator.

Relays are widely used in various industries for many different applications. Traditional mechanical relays are large, slow, noisy devices, but are still widely used in various machines and processes for control purposes. As the microelectronic industry develops in the last few decades, various solid-state switches have been developed. Compared to conventional mechanical relays, solid-state relays have much longer life times, faster response, and smaller sizes. These comparative advantages have made solid-

state switches popular in microwave and millimeter wave integrated circuits (MMICs) for telecommunication applications including signal routing, impedance matching networks, and adjustable gain amplifiers. The state-of-the-art technology uses compound solid-state switches such as GaAs MESFETs and PIN diodes. However, these solid-state switches tend to have low off-resistance, which causes finite current flow leakage in the off-position and high on-resistance which results in high power consumption. Design trade-offs for reducing the on-resistance of solid-state relays tend to increase output capacitance, which introduces additional problems in applications requiring the switching of high frequency signals[4].

Several different prototypes of micro-relays have been reported. Suzuki[10] reported an electrostatically actuated micro-relay for use in automatic test equipment (ATE). Their design, comprised of silicon and glass chips bonded together, tried to combine the isolation and low leakage current qualities of the traditional mechanical relays with the speed and size advantages of solid-state relays. Actuation voltages less than 100 V have been obtained, and on-resistance has been measured to be less than 1 Ω. Yao and Chang[18] reported a surface micromachined micro-switch for telecommunications applications. It was made on a semi-insulating GaAs substrate using a suspended silicon dioxide micro-beam as the cantilever arm, a platinum-to-gold electrical contact, and electrostatic actuation, requiring about 28 V, as the switching mechanism. The relay functions from DC to RF frequencies, and has an electrical isolation of -50 dB and an insertion loss of 0.1 dB at 4GHz. The switch closure time is on the order of 30 μs. Hashimoto et al.[19] reported a thermally controlled magnetization micro-relay. Heating actuates the device with an integral titanium film heater, which changes the local magnetization. The result is

a simple structure that does not require an electromagnetic coil. Permanent magnets are used to obtain self-latching. The device has a response time of more than 10 ms, which is comparable to conventional full-size mechanical relays. Saffer et al.[20] reported an electrostatically actuated micro-relay with a stationary mercury micro-drop at the point of contact. They proposed the use of mercury to solve the contact problems such as surface degradation of the contacts, signal bounce, and unstable contact resistance.

The first effort using the LIGA process for fabrication of micro-relays was made by Rogge et al[21]. In their study, an integrated magnetic core wrapped with a microfabricated planar coil was made with the LIGA process. The footprint of the complete micro-relay is about 4 mm by 2.3 mm, it required a current of 1.4 A to drive. In 1994, Hosaka et al.[22] reported some fundamental works on electromagnetically actuated micro-relays. In their research, a miniature (inch-size) electromagnetic relay was constructed using a microfabricated spring and a large external coil assembled together.

Compared to solid-state switches, MEMS relays have about the same advantages as normal mechanical relays: lower on-resistance, higher off-resistance, higher dielectric strength, higher breakdown voltage, lower power consumption, and lower cost. Furthermore, by using MEMS technology, the size, cost, and switching time of mechanical relays are greatly improved, and they can also be combined with other electronic components. These advantages are even greater with multi-contact relays, such as matrix switches.

However, compared to signal switches, there are not been as much effort reported in developing manufacturable power switching micro-relays. The performance requirements for power micro-switches should include: low-on resistance, high off-resistance, high

reliability, large power capacity, fast response, micro-size, and availability by low cost batch-production. To achieve higher power capacity, a micro-relay based on MEMS technology should have following characteristics: (1) materials of high electric conductivity, for example, metals or alloys such as copper should be used; (2) thick wire pattern should be used to carry larger current, other than thin films as used in silicon based surface fabrication technology.

Compared to more conventional MEMS processes based on silicon technology, the UV-LIGA process based on thick photo resists such as SU-8 has some unique advantages: (1) it allows the fabrication of microstructures of any lateral shape with structural heights up to several hundreds of micrometers in any cross-sectional shape[23]; (2) a wide variety of materials such as plastics, metals, alloys, and ceramics, or a combination of these materials can be used as the structural materials[24]. These advantages make it very suitable for fabricating micro power relays. For example, beryllium-copper can be used for making a micro-spring, high aspect ratio microstructures can be used to achieve stronger force with limited driving voltage, and good electrically conducting materials such as copper and gold can be electroplated as electrodes for better contacting condition.

1.2.3 Micro-sensors

There are hundreds of micro-sensors reported for various applications[25]. The first widespread application of MEMS sensors was in automobiles: a pressure sensor that gauged the air intake of engines. Another MEMS application in automobiles came along with the widespread installation of air bags[26]. The biomedical industry is the second biggest field for MEMS sensors. The first major medical application was a sensor that

measured blood pressure. Before MEMS sensors were developed, doctors had to use fragile, expensive pressure transducers, or periodically monitor a patient's pressure manually. MEMS are also found in infusion pumps, respirators, kidney dialysis machines, and other medical devices[27,28]. Industrial process control is the third largest type of MEMS sensor application. Because pressure sensors are used in virtually all types of control equipment, this area is the most diverse in terms of applications[29]. Some of the most recent innovative applications include accelerometers in navigational-grade guidance systems, rate gyroscopes in antilock-braking systems, and chemical sensors in complex biomedical instruments[30]. In this dissertation, the novel design of a capacitive micro-accelerometer by a multi-layer, multi-step UV-LIGA process was studied as an example of micro-sensors. Basically, the fabrication process and the working principle are the same as those of the micro-power relay.

There are several different sensing schemes used in the accelerometers: piezoelectric, piezoresistive, variable capacitive, resonant beam, and tunneling types[31,32,33]. In 1991, Analog Devices developed the first commercial accelerometer using the polysilicon surface micromachining technology. In 1992 Lucas Novasensor developed an accelerometer with self-testing and over-load protection functions[34]. At the present time capacitive sensing is certainly the most important detection method because of its numerous advantages, e.g. good linearity, low temperature sensitivity, and especially that it is the only design where the position detection can be combined with a closed loop structure based on electrostatic forces without any additional effort.

To date, most of accelerometers that have been developed and reported in the literature have been single-axis ones, and have been fabricated using silicon-based micro-

fabrication technologies with silicon as the structural material[35]. Surface micromachining is more cost effective in fabrication. Surface-micromachined devices tend to be smaller in sizes and can accommodate more on-chip circuitry. However, its out-of-plane dimension is normally limited to about 2 μm and the reduced seismic mass limits the sensitivity. Another disadvantage is the spring compliance is very low and may result in sticking failure. It also is limited to a single-axis design only. A bulk fabrication process using polysilicon is better in the capability to produce larger seismic mass with improved sensitivity, typically 1000 times compared with surface fabrication. It also requires only 12 mask levels[35]. However, the fabrication of seismic mass and the integration with circuitry are more complicated. Efforts have been made to fabricate accelerometers using x-ray lithography based LIGA technology to produce truly 3-D micro-accelerometers[36]. The major disadvantage for the x-ray LIGA technology is its high fabrication cost. It requires many expensive x-ray masks and a highly expensive synchrotron source. The primary reason may be that multi-axis accelerometers cannot be readily made with silicon based micro-fabrication technologies. Efforts have also been made to make 3-D accelerometers[37,38]. Qu et al. [39] also reported a 3-D differential-capacitive accelerometer made of electroplated nickel. They used AZ4562 as a thick resist and electroplated nickel microstructures about 30μm thick. Because the limitation of the resist used, the design of their sensors is still a planetary one, therefore the sensitivity is still limited. Toda et al.[40] reported a 3-D accelerometer made with glass in a spherical design. Their design used a non-silicon material and had a truly three-dimensional structure. However, the process technology involved makes the device very expensive. Ayazi and Najafi[41] also reported a

dry-releasing process to make 3-D microstructures based on silicon fabrication for inertial sensing applications.

As discussed in the previous paragraph, the x-ray LIGA process has the advantage of producing truly 3-D, high aspect-ratio microstructures of different materials. However, the high cost and long time-consuming exposure process make it not very suitable for any products that cannot be insert-molded. As a cheaper alternative, the UV based LIGA process has been getting more popular recently. In UV-LIGA process, a new and popular thick resist called SU-8 (originally developed by IBM and now marketed by Micro Chemicals, Inc., Newton, MA 02164) and ultraviolet light optical lithography are used, instead of the x-ray source. SU-8 based UV-LIGA, therefore, offers microstructures at slightly lower quality but at much lower cost and much higher productivity[42].

In the last few years, significant research efforts have been made worldwide to study the lithography property of SU-8 and to develop suitable micro-fabrication technology using it as thick resist. Limited research efforts have also been made to study the physical, thermal, chemical, and the optical properties[43,44]. Even though not very well studied yet, the limited study has provided enough understanding of the material. It seems that the cured SU-8 polymer has the following unique advantages: (a) Cured SU-8 polymer is highly resistant to solvents, acids, bases, and corrosive environment. (b) Cured SU-8 polymer has excellent thermal stability, making it well suited to be used as structural material. It has a glass temperature more than 200℃, a very low thermal conductivity of 0.2 W/m℃, and low thermal expansion coefficient (21 ppm/℃, SM2070 with 70% filler in the blend, SOTEC MICRO) [45]. This also means that the MEMS systems made with SU-8 as the structural material may be less sensitive to temperature variation. No

significant mechanical hysteresis effect has been reported. It also does not show any plastic domain[42,46]. Compared to silicon, the cured SU-8 polymer also has the following disadvantages: It is sensitive to chlorine environment; it can only take temperature to about 120℃ without significantly affecting the mechanical property; plastic deformation is going to be the primary cause of failure; inherently residual stresses in the structures may cause errors in the sensing results, therefore, careful post-processing steps may be required to eliminate the effects; it has lower physical strength and Young's modulus compared with silicon[47,48,49]. However, due to its reasonably good physical, chemical, and thermal properties, much easier process technology and significantly lower overall production cost, it can be a competitive option for some of the not-so-stringiest applications. In addition, the readily available high-aspect-ratio structures and multi-layer fabrication flexibility may also make some of the complicated inertia sensor systems become relatively easier to make in comparison with the silicon based micro-fabrication technologies.

Very few research efforts have been reported in utilizing the cured SU-8 high aspect-ratio microstructures as structural materials and use SU-8 based UV-LIGA technology for accelerometers and other types of inertial sensors[50]. Therefore, this work may also contribute new category of applications of SU-8 photoresistor.

CHAPTER 2: WORKING PRINCIPLE OF TRANSDUCERS AND THEIR DESIGN

2.1 Working Principle

Generally speaking, there are four types of actuation forces used for MEMS sensors and actuators[51]: electrostatic[7-12], electromagnetic[52], thermal[13], and piezoelectric[53] forces. Electrostatic force is probably the most widely used actuation force first adopted in the MEMS devices. It can be found on applications in such devices as comb-drive actuators[4] and micro-electrostatic motors[8,16] that are one of the most widely reported MEMS devices. The major advantage of electrostatic actuation is the low power consumption. This is particularly important where it is desirable to have the devices operating in a portable-electronics environment.

Electrostatic actuation predominates at small scales for prime movers rather than electromagnetic actuation at larger scales. The reasons are as follows: first of all, the electrostatic force that can be generated between two surfaces held at a fixed potential difference scales with the second power of a characteristic length related with surface area. In contrast, the force that can be generated by an electromagnet operating at a fixed current density scales with the fourth power of the length due to the fact that a permanent magnet made of a particular material scales with the volume. Thus, given that the mass acted on by the force scales as the third power of length, the acceleration achievable by electrostatic actuation benefits from cube-square scaling whereas electromagnetic actuation is either neutral with scale or actually deteriorates at small scales.

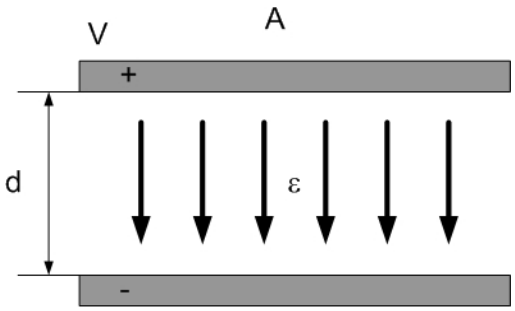

Figure 2-1 Parallel-plate capacitor at fixed potential difference

For example, in a parallel plate capacitor shown in Figure 2-1, the potential energy can be calculated as follows:

$$U = \frac{1}{2} CV^2 \tag{2-1}$$

where C is capacitance ($C = \varepsilon \frac{A}{d}$), V voltage ($V = Ed$), A surface area of the electrical capacitor, ε electric permittivity of the medium (ε =8.85×10^{-12} Farads/meter [F/m] or $C^2/N{\cdot}m$ for free space), d gap between the plates, and E electric field. Then,

$$U = \frac{1}{2} \varepsilon dAE^2 \tag{2-2}$$

The parameters scales as $d = [L]$ and $A = [L^2]$, and the force can be expresses as:

$$F = \frac{\partial U}{\partial x} = \frac{1}{2} \varepsilon \frac{\partial}{\partial x} [dAE^2] \tag{2-3}$$

Therefore, the electrostatic force scales with the second power of a characteristic length related with surface area.

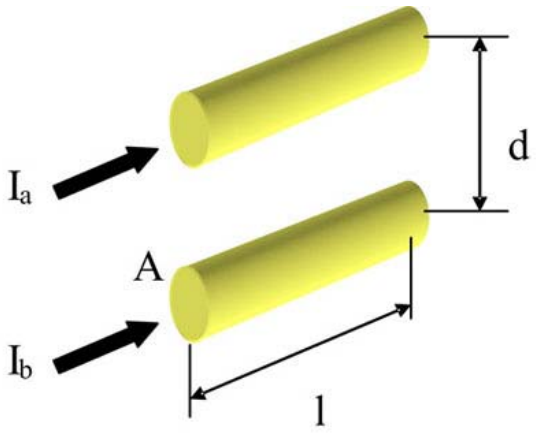

Figure 2-2 Two wire segments of length l are shown separated by d and carrying currents I_a and I_b. The forces on the wires are given by Equation 2-5

In the case of electromagnetic force, at constant current density,

$$I = \int J \cdot dA = JA \tag{2-4}$$

I is the total current through the wire and J is current density. In addition, the current density is assumed to be an intensive variable: its value does not change as the scale size is changed. In terms of our notation, $J = [L^0]$. The area scales as $A = [L^2]$, and $I = [L^0] \cdot [L^2] = [L^2]$, and the force can be expresses as,

$$F = \frac{\mu}{2\pi} I_a I_b \frac{l}{d}. \tag{2-5}$$

It can therefore be seen that the force F scales as L^4. If the scale size decreases by a factor of 10, the force decreases by a factor of 10,000[54]. This regime is quite unattractive. Secondly, the breakdown voltage of an air-gap at the macro-scale (~1cm) is in the order of 3×10^6 V/m. However, reduction of the air gap to dimensions close to the mean free path of air molecules (~1μm) increases the breakdown voltage to 1×10^8 V/m[55]. This increase of nearly two orders of magnitude in breakdown voltage results in a proportional

increase in the scaling of the actuation force. Third, electromagnets require three-dimensional electrical windings, which are not readily achieved via micro-fabrication compared to actuators driven by electrostatic force. Finally, electromagnetic actuators often require large driving current to obtain stronger electromagnetic force than an electrostatic one, which further tilts the balance in favor of electrostatic actuation.

Thermal actuation can produce larger force and small deflection for micro-devices[56]. Thermal force exhibits higher restoring force than contact force. For communicational application of electro-thermal actuators, this is an important advantage because high restoring forces are necessary to unstuck weld contacts. However, they need heaters to produce temperature grades. In addition, the temperature grades produced by heaters affect other structures' work. Other major drawbacks of thermal actuation are the slow switching time and the high power consumption.

Piezoelectric actuators can produce larger force[53], but the working range is too short. Additionally they need very high driving voltage.

The transducers presented in this research rely on the storage of electrical energy in parallel plate capacitor. Electrostatic forces (mutual attraction of two opposite-charged electrodes) were used as a driving force in the micro-relay, and capacitance as a sensing parameter in the micro-accelerometer.

2.2 Design of Structure

2.2.1 General Remarks

To date, most of MEMS devices are lateral or planar (in-plane) motion ones, while in our design vertical (out-of-plane) motion has been applied to drive the micro-relay or

monitor the acceleration. There have been some reported studies on advantages and limitations of the lateral and vertical switches in the MEMS field[57,58]. Vertical actuators have the advantages of providing a larger area for the electrostatic force and help to obtain lower contact resistance. In addition large displacement and small actuation voltage meet stringent telecommunication switching requirements. Some other groups have reported MEMS structures with vertical motion. Selvakumar et al.[59] developed vertical comb array micro-actuators by trench formation in bulk silicon and trench filling of polysilicon. Kim et al.[60] developed vertical actuators by using extended SBM (surface bulk micromachining).

Overall design concept and working principle are quite similar between a relay and an accelerometer. The two or four flat symmetric springs with inertia mass were used, and the capacitance was used to generate driving force in the relay and to measure acceleration in the accelerometer. Springs are among the most important elements in the fabricated transducers. Several different kinds of springs were presented in the literature[61]. In order to reduce the occupied area for the same spring stiffness and overcome the buckling problem produced by the residual stress, the serpentine springs were used in the fabricated transducers.

Another unique property of this design is that the design can be readily modified depending on operating condition. For example, cantilever type transducers have much lower spring stiffness compared to symmetric transducer because they have only one spring as shown in Figure 2-3. This means that cantilever type transducers can be operated in the much lower frequency range. The detail design of transducers is shown in the following two sections.

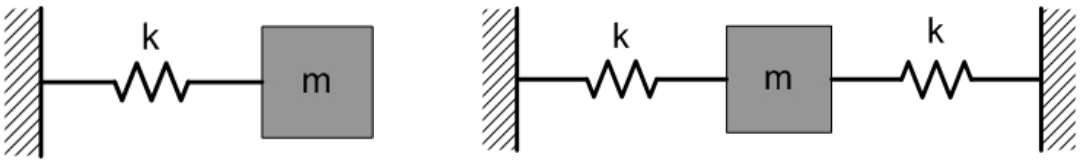

(a) Cantilever type transducer (b) Symmetric type transducer

Figure 2-3 Two types of spring design

2.2.2 Power Relay

The basic design of micro-relay is shown schematically in Figure 2-4. It is comprised of the following components: flat springs for suspension, an electrostatic actuator (parallel plate capacitor) to drive the relay in up and down motion, the switching contacts--two electrodes (input /output), and a connector for each channel to be switched. This kind of spring suspension and electrostatic actuator has been commonly used in MEMS field[23,62]. In the heart of this micro-power relay is the "armature": a moving block (plunger) suspended by the flat springs. The armature is composed of three pieces of metal and two pieces of embedded polymer as marked in Figure 2-4. The four flat springs are symmetrically arranged to maintain dynamic balance. They are also physically and electrically connected to the top plate of the capacitor actuator. All of components are metal or alloys except the polymer connectors, which are made of cured SU-8. The top plate is perforated to allow for the sacrificial layer etching underneath and to reduce air damping effects during operation. The design of the "armature" is a very unique feature for this power relay. The armature functions as both the electrostatic actuator and the switching mechanism. It consists of two (or three as in this two-way switch design) chunks of metal held together by imbedded polymer connectors. The polymer connectors serve two major functions here.

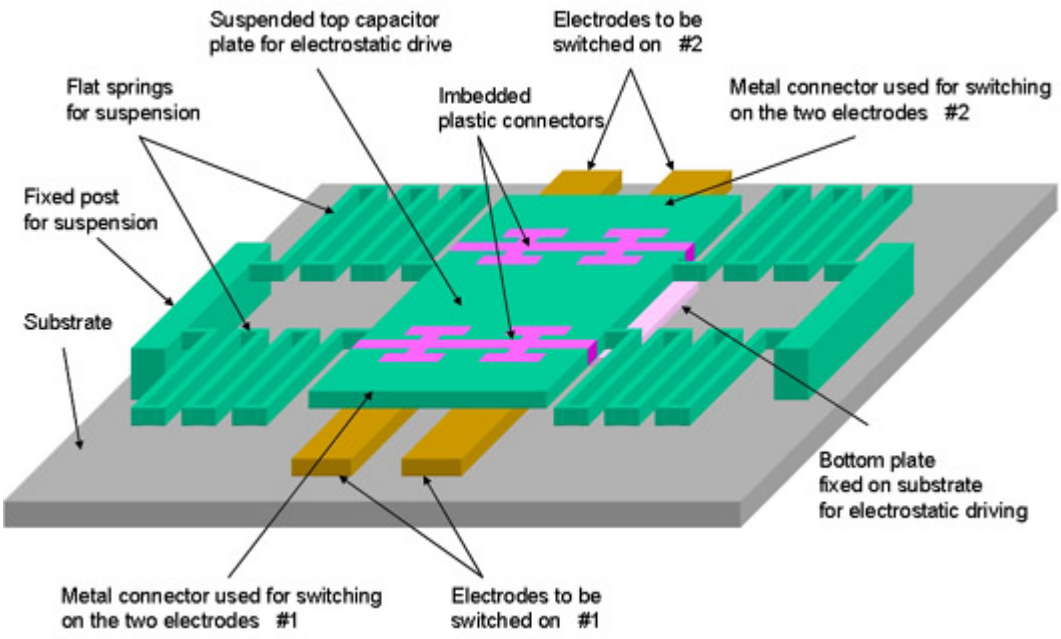

Figure 2-4 Schematic design diagram of the micro power relay. In this basic design, the switch can be used to control two channels, one in the front and one in the back

They physically connect the top plate of the capacitive actuator (the middle piece) and the switching connectors in both the front sides and the back sides (metal parts), and isolate these three sections of the armature electrically. In this arrangement, the control (driving) signal supplied to the top plate of capacitor actuator and the power signal to be switched are completely isolated from each other. This helps to avoid any cross talk between the two sections of the relay.

The control electrical signal is supplied across the top capacitor plate through the supporting pads and springs and the bottom plate shown below the top plate in Figure 2-4 to generate electrostatic force to pull down the top plate. When the top plate of the capacitor is pulled down, it also carries the two pieces of metal connectors (front and back sides of the armature) down, to respectively "close" the two electrodes in the front

side (marked as for switch #1) and the two electrodes in the back side (marked as electrodes for switch #2).

The supporting pads for flat springs are used as electrodes to which the control signal for the actuator is supplied. Springs are free to move together with the armature. The supporting pads fixed on the substrate are used to suspend the flat springs and the armature and to supply control voltage signals. These supporting pads, the bottom plate of the capacitor, and the electrodes (for switch #1 and switch #2) of relay as shown in Figure 2-4 are electrically isolated. This arrangement is necessary because one side of armature is used as electrode for the electrostatic actuator and the other side serves as the switching connector for the power circuit electrodes to be switched.

It also should be noted that the schematic design in Figure 2-4 shows the basic operational principle only. The specified shape and layout of the flat springs and the electrostatic actuator need to be determined based on the specific design requirements such as power capacity, the response speed, as well the control voltage to be supplied.

A typical operation sequence for a normally off relay is as follows [Figure 2-5]:

(1) If there is no control voltage supplied, the spring remains in the neutral position and the relay is off (electrodes do not make contact with the connectors).

(2) If a control voltage is supplied to the capacitor actuator, the electrostatic force drives the armature down until the two electrodes of each switch are electrically connected by the top piece of metal that serves as electrical connector.

(3) To switch off the relay, the control voltage is turn off, and then the spring force will pull the armature to the statically balanced neutral position. Contact is broken and the relay is switched off.

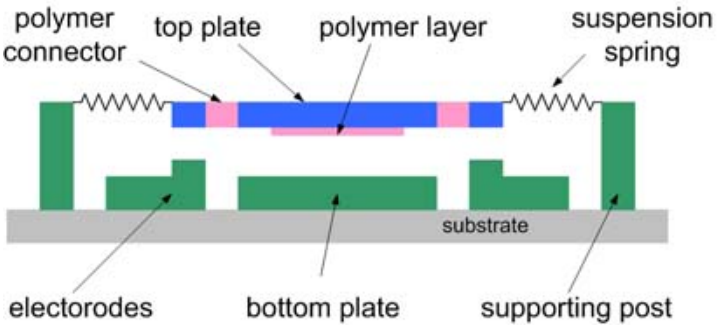

(a) Initial open position

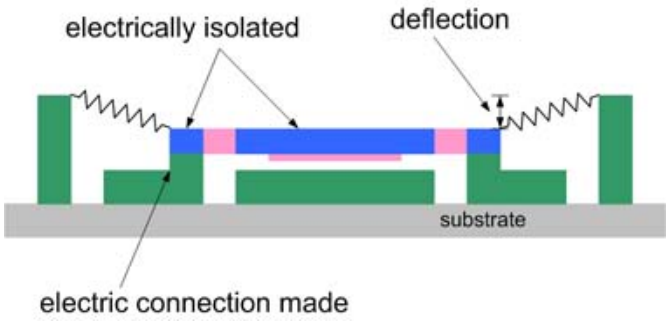

(b) Closed position: electrostatic force pulled down the top plate of capacitor

Figure 2-5 Side-view schematic diagram of relay

There are several major advantages with this design. First, the control signal and the circuits to be controlled are completely isolated. For power applications, this offers great advantages. Second, the design of the relay is truly three-dimensional with vertical motion. The unique simple design of the relay makes it possible to use the UV-LIGA processes for fabricating these high-aspect-ratio metal electrodes for switching connection.

From a mechanical point of view, cross-linked SU-8 has very good physical strength compared with most of the polymers. It is chemically resistant when it is cured to over 100℃ and its thermal stability is over 200℃. It can also withstand most of the standard acidic and alkaline plating solutions. It also has more than enough physical strength to take the small load when the electrostatic force pulled the top plate of the capacitor down. The high temperature stability helps to avoid any malfunction or damages if the relay operates in a relatively high temperature environment up to 100℃ for a short period. From an electrical point of view, it has very high dielectric strength (15 $kVmm^{-1}$) and electric resistance (volume resistivity = 2-14 $\times 10^{15}$ Ohm cm). Because the relay will be packaged in a complete enclosure, humidity is not expected to affect the operation of the relay.

The schematic design shown in Figure 2-4 is for a two-way, "normally-off" relay. Other types of relays may also be designed in a similar fashion by changing the layout of springs and arrange more electrodes as shown in Figure 2-6. Therefore, it is easy to manufacture a relay whose signal lines change in many directions. Suspension springs can also be added on the right side of the switch and can be used as electrodes for the switch [Figure 2-6 (f)]. The geometry of the switching connector on the right side of the relay also can be varied to permit more electrodes to be arranged. Different control voltage can also be supplied to generate actuation for in different direction and different levels. These methods can be used to produce the other types of possible relays, such as three-way relays.

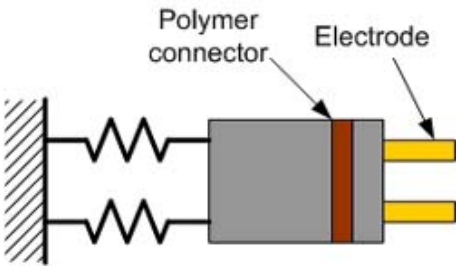

(a) Cantilever type with 1 electrode

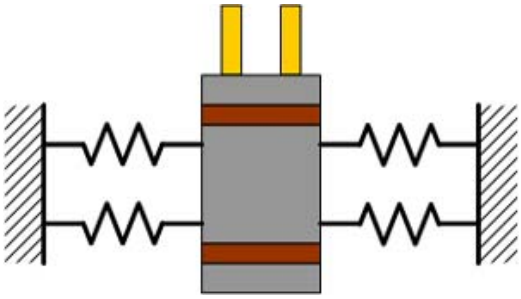

(b) Symmetric type with 1 electrode

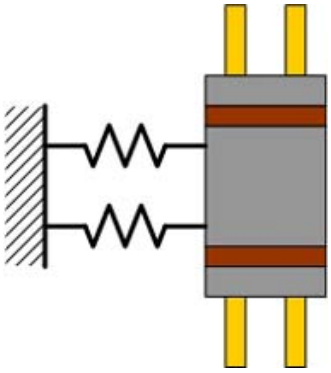

(c) Cantilever type with 2 electrodes

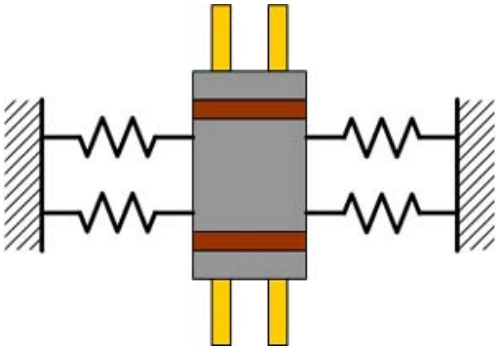

(d) Symmetric type with 2 electrodes

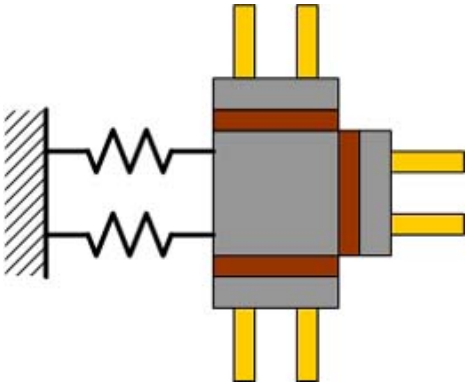

(e) Cantilever type with 3 electrodes

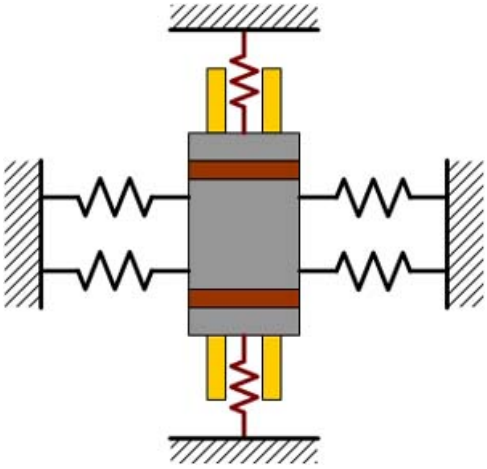

(f) Symmetric type with 3 electrodes

Figure 2-6 Other types of relays

2.2.3 Accelerometer

Several different types of accelerometers for one-axis, tow-axis, and 3-D measurement were designed. The basic design for a single-axis accelerometer is shown

schematically in Figure 2-7. The overall design concept of the accelerometer is pretty much the same as that of the relay. However, the accelerometer was designed such that cured SU-8 was used as the structural material and a very simple fabrication process was required. Green colored sections were made with cross-linked SU-8, and yellow colored parts were made of metals such as chromium or gold. Figure 2-7 (a) shows a one-axis accelerometer using one capacitive sensor. It was comprised of flat springs for suspension and seismic mass; both were made with cross-linked SU-8 polymer, a capacitive deflection sensor formed with two parallel plates, and the insulation and supporting caps. Figure 2-7 (b) shows the schematic design for differential capacitive accelerometer. The sensor has a symmetric design with two identical parts bonded together. The two capacitive sensors of the accelerometer are used in a differential measurement scheme. The mechanical motion of the case is converted to a relative motion between the spring-suspended mass and the sensor case. The top and bottom capacitive sensors then measure the motion. For example, when the mass moves upward, the gap of the top capacitor is reduced and the gap of the bottom capacitor is increased. Other types of multi-axis inertial systems may also be designed and fabricated with the same fabrication technology and using cross-linked SU-8 as the structural material. Figure 2-8 shows the design of 3-axes micro-accelerometer based on using cured SU-8 as the primary structural material. Figure 2-8 (a) shows the bottom part of the accelerometer. It has four vertical sidewalls made of cured SU-8 polymer. The inside-walls of them are coated with thin films of metals which can be either evaporated or sputtered using shadow masks.

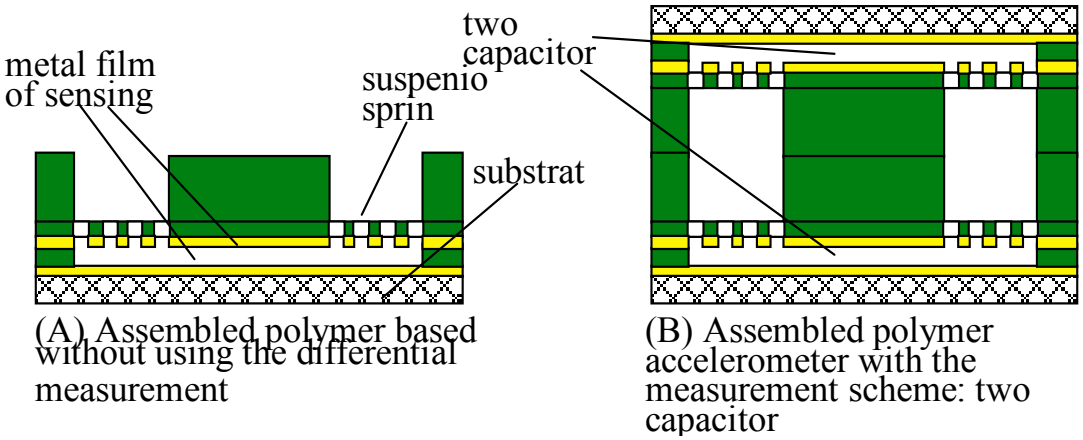

Figure 2-7 The schematic diagram of the proposed one-axis accelerometer: (a) single-output and (b) differential output layout

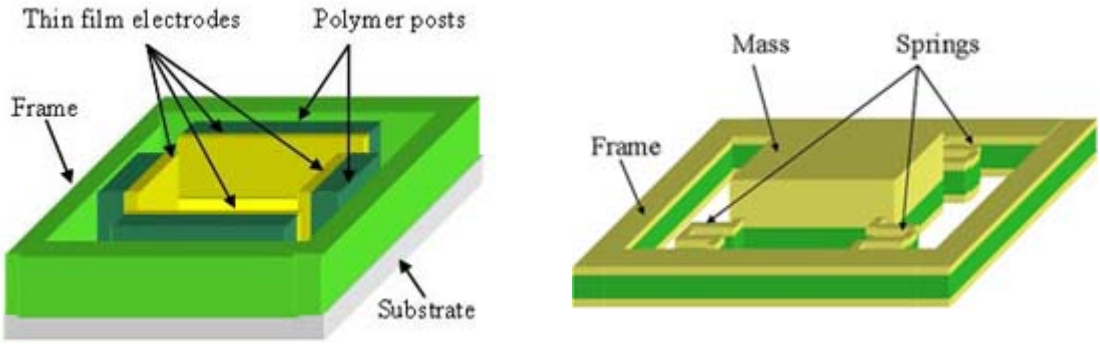

(a) Fixed electrodes on the bottom part. Wire pads are patterned on substrate, and inside-walls of the polymer posts are coated as electrodes.

(b) Top view of suspension springs-seismic mass. Conformal sputtering a thin layer of metal as the common electrode for the capacitive sensors for x-y-z axes (yellow color).

Figure 2-8 The schematic diagram of the 3-axes accelerometer: differential outputs layout

They may also be made by the UV-LIGA approach such as plating nickel or copper into the lithographically patterned plating moulds, which have been done in other published research work[21, 63, 64, 65]. Figure 2-8 (b) shows the design for the top part of the accelerometer. A seismic mass and integrated suspension springs patterned with cured SU-8 are coated with a thin layer of metal film that serves as the common electrode for all three pairs of capacitive sensors. The green colored frame is designed for the purpose

of handling, bonding, and packaging. After the top part of the accelerometer is bonded onto the bottom part, two pairs of capacitive sensors are formed for the two horizontal axes (*x* and *y*) for differential measurement. For the vertical direction (*z*-direction), if a differential measurement scheme is also preferred, a cap with a fixed electrode as shown in Figure 2-7 can also be bonded on the top to form another capacitive sensor.

CHAPTER 3: STATIC & DYNAMIC ANALYSIS AND SIMULATION

3.1 Introduction

The primary objectives of the static and dynamic analysis for the designed transducers are to provide a realistic assessment of the performance and guidance for improvement of the design and control of the transducers. For these purposes, both analytical and numerical analyses were presented. The analytical expressions for the physical features of the structures allow optimizing the relevant design parameters such as force, spring stiffness, capacitance, and occupation of area. In order to verify the analytical relationships, a finite-element simulation using ANSYS was performed. Analysis of the individual components was performed separately, and then followed by analysis of the assembled relay and accelerometer. Comparison of the energies associated with both the electrostatic attraction and the spring deflection provided the design limits for each component. The dynamic response characteristics of the device were simulated using SIMULINK and ANSYS, and compared with test results to demonstrate the effectiveness of the dynamic models presented in Chapter 7.

3.2 Modeling and Analysis of Individual Components

3.2.1 Electrostatic Force

A parallel-plate capacitor was designed to have one movable plate as shown in Figure 3-1. The other plate is formed by a stationary surface which is in close proximity to the mass. The mass moves in response to a pure mechanical force and an electrostatic attractive force. Although actual capacitors exist in a three-dimensional physical

continuum and their behavior is governed by the physical laws, the behavior of the capacitor can be represented using a set of electric circuit elements. This method is known as the lumped modeling with circuit element[66]. Instead of being described by the differential equations of motion of the structure members, by the characteristic equations of the transducer elements, and by a set of boundary conditions, the behavior of electromechanical transducers can be described by the equivalent circuit elements. The approach is based on the analogy that exits between electric and mechanical systems. In this method, the transducer is no longer described by complex differential equations and boundary conditions, but by a lumped element 'electrical' circuit in which the elements are physically representatives of the transducers' properties such as its mass, stiffness, capacitance, and damping. The circuits implicitly contain, because of the way they are constructed, all the equations governing the system represented. Equivalent circuits are particularly useful for the analysis of systems consisting of complex structural members and coupled subsystems with several electrical and mechanical ports. Not only is the strict use of differential equations very difficult for these cases, but this method also often obscures the solution[67]. The equivalent circuit method lends itself to a better visualization of the system, and, once the basic circuit is constructed, it may be used in further analyses to investigate the effects of connecting subsystems or of making modifications to the structure.

In applying this method to the parallel-plate capacitors, there are a couple of advantages. First of all, circuit analogies of this method permit efficient modeling of the interaction between the electronic and the non-electronic components of a micro-system. Therefore, this system can be demonstrated with two ports as shown Figure 3-2: an

electrical port with voltage and current as the conjugate variables, and a mechanical port with force and velocity as the conjugate variables. The state variables associated with the mechanical and the electrical ports are displacement and the electric charge respectively. A further advantage of circuit models is that they are intrinsically correct from an energy point of view since a parallel-plate capacitor is one of energy-conserving transducers.

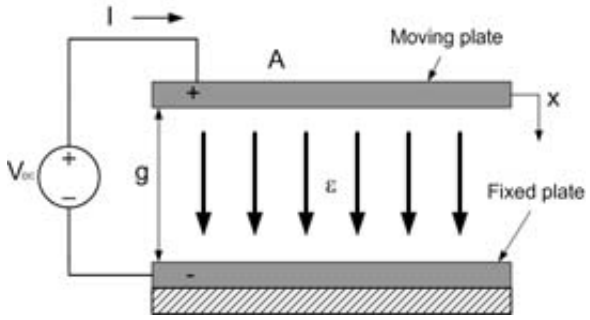

Figure 3-1 Parallel-plate capacitor

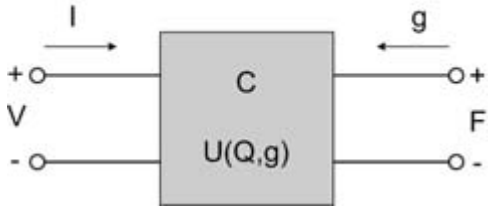

Figure 3-2 Lumped model: a two-port capacitive transducer

The stored energy can be calculated by two ways: fix the gap and increase the charge, and keep the charge fixed and increase the gap. The first method involves charging the capacitor to charge Q at fixed gap *g*. There is no mechanical work done by the external force since the gap is fixed. The total electrical energy stored by the capacitor in Figure 3-1 is

$$U = \int Power\, dt = \int V \cdot I\, dt \tag{3-1}$$

where V is voltage ($V = \frac{Q}{C}$) between the capacitors and I is current ($I = \frac{dQ}{dt}$). Therefore,

$$U = \int V \cdot I dt = \int \frac{Q}{C} \cdot \frac{dQ}{dt} dt = \frac{Q^2}{2C} = \frac{Q^2 g}{2\varepsilon A} \tag{3-2}$$

where A is surface area of the electrical capacitor, ε is electric permittivity of the medium ($\varepsilon = 8.85\times10^{-12}$ Farads/meter [F/m] or $C^2/N\cdot m$ for free space), and g is gap between the plates.

The second method involves charging the capacitor to a total charge Q at zero-gap, and then lifting the upper plate to create the gap g. Because the capacitor is charged at zero-gap, the voltage across the capacitor is virtually zero, there is no electrical energy stored at zero-gap. However, mechanical work needs to be done by the external force to lift the plate to a gap g,

$$U = \int Power\, dt = \int F \cdot \dot{g}\, dt\,, \tag{3-3}$$

where F is force ($F = \frac{Q}{2}E$) and E is electric field ($E = \frac{Q}{\varepsilon A}$). Therefore,

$$U = \int F \cdot \dot{g} dt = \int \frac{Q}{2} E \cdot \frac{dg}{dt} dt = \frac{QEg}{2} = \frac{Q^2 g}{2\varepsilon A}\,. \tag{3-4}$$

Then the work done by force F [Equation 3-4] is the same as the stored energy [Equation 3-2] in the capacitor with fixed gap. This means the stored energy is actually a function of two variables, *U(Q,g)*. Further, a set of differential equations can be constructed to describe how the stored energy changes if either quantity changes, using the basic definitions of stored energy in each energy domain:

$$P = \frac{dU(Q,g)}{dt} = \frac{\partial U}{\partial Q}\cdot\frac{dQ}{dt} + \frac{\partial U}{\partial g}\cdot\frac{dg}{dt} = V \cdot I + F \cdot \dot{g}\,. \tag{3-5}$$

Because *dQ/dt* is the current flow associated with the capacitor, *∂U/∂Q* must be the voltage because the product of these two yields the power. Similarly, *dg/dt* is the velocity

of the plate and $\partial U/\partial g$ is the force associated with it. From these identifications and the Equation 3-5, the constitutive equations for F and v can be determined as:

$$V = \frac{\partial U}{\partial Q} = \frac{Q}{C} = \frac{Qg}{\varepsilon A}, \tag{3-6}$$

and

$$F = \frac{\partial U}{\partial g} = \frac{QE}{2} = \frac{Q^2}{2\varepsilon A}. \tag{3-7}$$

Substitution of Equation 3-6 into 3-7 gives, after routine simplification,

$$F = \frac{\varepsilon A V^2}{2g^2}. \tag{3-8}$$

The physical constants associated with the designed micro-transducers were listed in Table 3-1. Figure 3-3 shows the relationship between the electrostatic force and the displacement of the movable plate with 20-volt increment from 20 to 100 volts. The theoretical electrostatic force existing between the parallel plates at an instantaneous displacement from its initial air-gap can be determined from the respective constant voltage lines. As expected in Equation 3-8, the smaller gap and larger voltage results in a much larger electrostatic force.

Table 3-1 Parameters used in the modeling of the transducer design

Parameters	value
Applied Voltage (V)	20-100 V
Electric permittivity (ε)	8.85×10^{-12} F/m
Surface area (A)	4×10^{-6} m^2
Initial air gap (g_0)	25×10^{-6} m

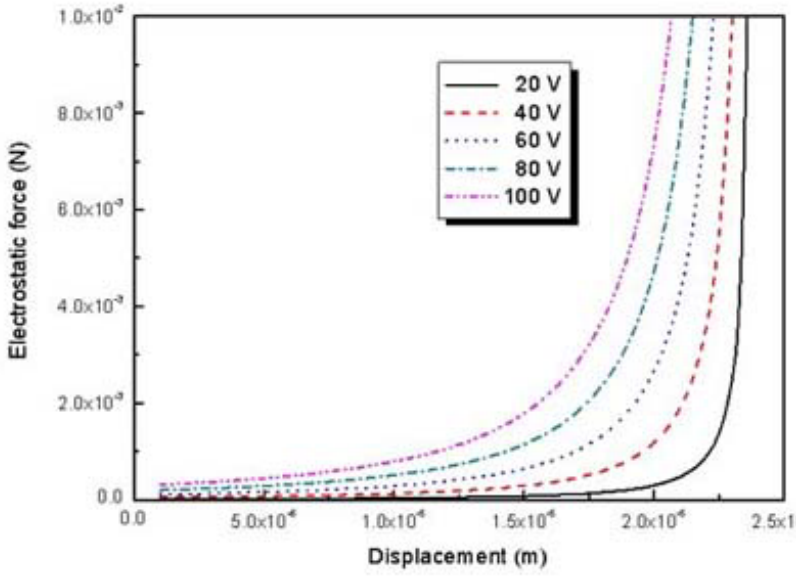

Figure 3-3 Electrostatic force versus displacement of the movable plate with voltage increment

3.2.2 Spring Force

In order to characterize the springs the displacement Δx resulting from the applied force F was calculated first. Then equivalent spring constant K of the springs can be estimated as

$$K = \frac{F}{\Delta x}. \tag{3-9}$$

The elastic deflection involving more than the bending loading can be calculated using Castigliano's method. When a body is elastically deflected by any combination of loads, the deflection at any point and in any direction is equal to the partial derivative of strain energy with respect to a load located at that point and acting in that direction[68],

$$\Delta x\left(\textit{deflection in direction of } F\right) = \frac{\partial U}{\partial F}. \tag{3-10}$$

In all but the simplest case, the expression for U will involve more than one term, each of which expresses the energy associated with one component of loading. In most beam applications, however, deformations from shear and axial loads are negligible. Thus, only displacements from bending and torsion are considered in the analysis. The equations for elastic strain energy associated with the various types of loading are summarized in Table 3-2.

Recently, Iyer[69] and Barillaro[70] reported some extensive studies on the serpentine springs. For the N repeated serpentine springs, it is divided into three parts to calculate the total displacement Δx [Figure 3-4]. The initial and the final parts are used to connect the spring to the anchor and to the movable mass. The required number of N repeated parts is connected to the initial and the final parts. Every spring part is analyzed as the connection of several elementary beams, each one withstanding torsion and bending deformation. The length of each beam is measured along the central axis of the beam between the centers of two consecutive corners. The joints are supposed to be ideal in transferring the forces and torques without significant deformation. Then the equivalent spring constant K of the serpentine springs can be estimated using Equation 3-9. Consequently the spring constant in z-direction is simplified as

$$K \approx \frac{6EI_yGJ}{(N+1)h^3GJ + (16N^3 + 36N^2 + 43N + 3)g^2hEI_y} \quad (if\ h >> g)^{70}. \tag{3-11}$$

Table 3-2 Summary of energy and deflection equations: where P is axial loading, M moment, T torque, V shear force, E modulus of elasticity, G modulus of rigidity, I moment of inertia, J polar moment of inertia, A cross sectional area.

Load type	Factors involved	Energy equation	Deflection equation
Axial	*P, E, A*	$U=\int_0^L \frac{P^2}{2EA}dx$	$\delta=\int_0^L \frac{P(\partial P/\partial F)}{EA}dx$
Bending	*M, E, I*	$U=\int_0^L \frac{M^2}{2EI}dx$	$\delta=\int_0^L \frac{M(\partial M/\partial F)}{EI}dx$
Torsion	*T, G, J*	$U=\int_0^L \frac{T^2}{2GJ}dx$	$\delta=\int_0^L \frac{T(\partial T/\partial F)}{GJ}dx$
Transverse shear (rectangular section)	*V, G, A*	$U=\int_0^L \frac{3V^2}{5GA}dx$	$\delta=\int_0^L \frac{6V(\partial V/\partial F)}{5GA}dx$

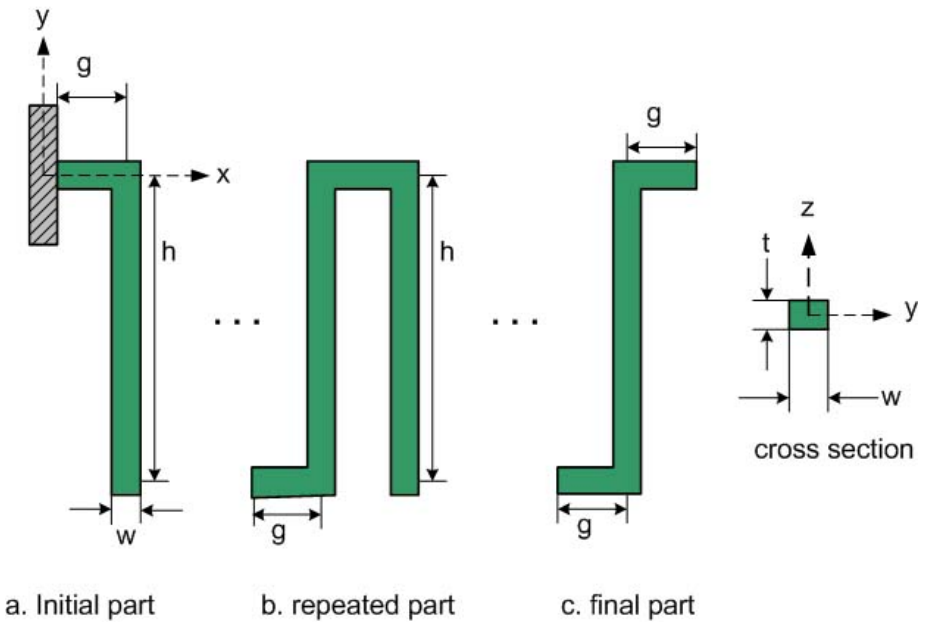

Figure 3-4 Three constitutive parts of spring: the initial and final parts used to connect it to the anchor and to the movable mass, and a central part which can be repeated

The design constants associated with the device are listed in Table 3-3. Particularly, the behaviors of the springs with N=0, 1, 2, 3, and 4 were analyzed. In order to verify the analytical relationships found for the elastic spring constants, a finite-element simulation using the ANSYS program was performed. For the three-dimensional meshing, the element SOLID45 was used. It is a brick element defined by eight nodes having three degrees of freedom (displacements) at each node. Figure 3-5 shows one of the simulation results by the ANSYS. In case the force of 10^{-4} N was applied at the end of spring in the z-direction, the maximum displacement of 20.6 μm was obtained. The ANSYS LOG file associated with Figure 3-5 was attached in the APPENDIX **Error! Reference source not found.**. The geometrical parameters and physical constant associated with simulations for the springs were listed in Table 3-3 and shown in Figure 3-4.

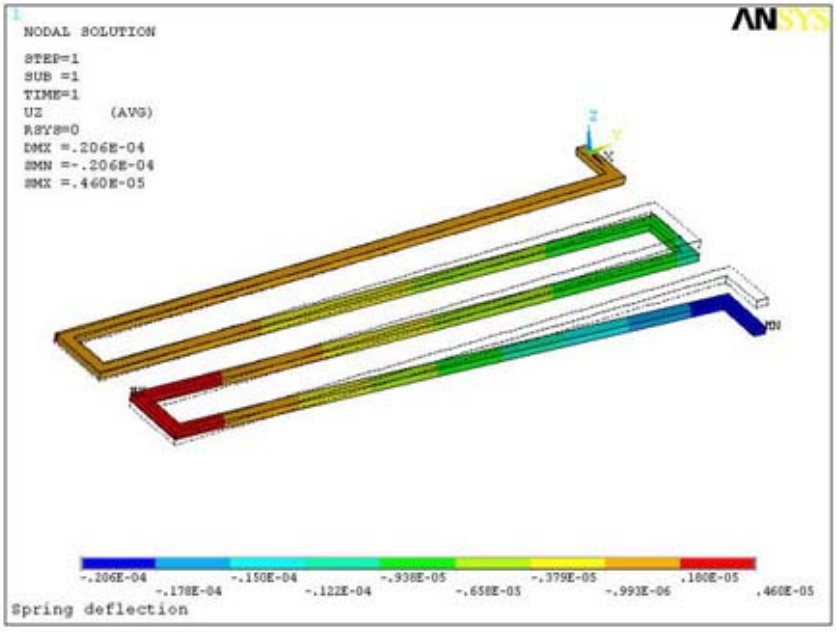

Figure 3-5 Simulated deflection of the spring: the maximum displacement is 20.6 μm when the force of 10^{-4} N is applied to the end of spring in the z-direction

Table 3-3 Design constant of nickel serpentine springs

Parameter	value
Modulus of elasticity (E)	206.843 GPa
Poisson's ratio (ν)	0.31
Modulus of rigidity (G)	$\frac{E}{2(1+\nu)}$
Height of spring (h)	2450 μm
Gap of spring (g)	225 μm
Width of cross section (w)	50 μm
Thickness of spring (t)	30 μm
Moment of inertia (I_y)	$\frac{wh^3}{12}$
Torsion factor J for a beam with Rectangular cross-section[71] (J)	$J=\frac{tw^3}{3}\left(1-\frac{192w}{\pi^5 t}\sum_{i=1,3,5,\ldots}\frac{1}{i^5}\tanh\left(\frac{i\pi t}{2w}\right)\right)$
Number of repeated part (N)	0-4

The Figure 3-6 shows the results of analytical calculation using Equation 3-11 and numerical simulation by ANSYS. The number of repeated part N marked as 'b' in Figure 3-4 does not affect the spring stiffness significantly with more than *N=3*, and makes the very stiff spring with *N=0*. Therefore, *N=1, 2*, or *3* were applied to our devices. On the other hand, the simulation results slightly deviated from the analytical calculations. For high thickness (t=40 μm), however, a considerable error was found for the spring stiffness (K). This is due to the fact that the slender beam approximation for each element of the spring is not valid, so that evaluation of bending is not accurate. The differences between the calculated and simulated value could also be caused by the fact that the joints between the beams are ideal, but this assumption becomes less valid as the thickness of the beam becomes larger.

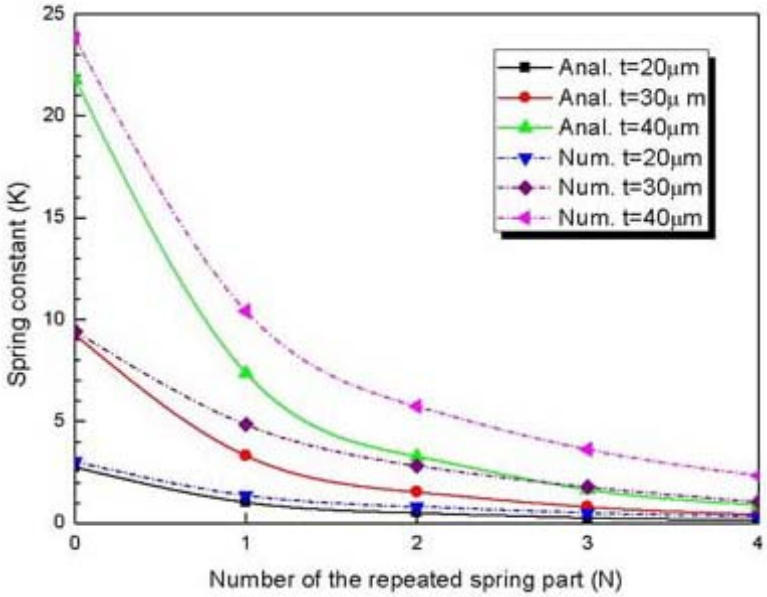

Figure 3-6 The spring constant versus number of the repeated spring part: Anal and Num denotes the results of analytical calculation and numerical simulation depending on thickness marked as t in Figure 3-4

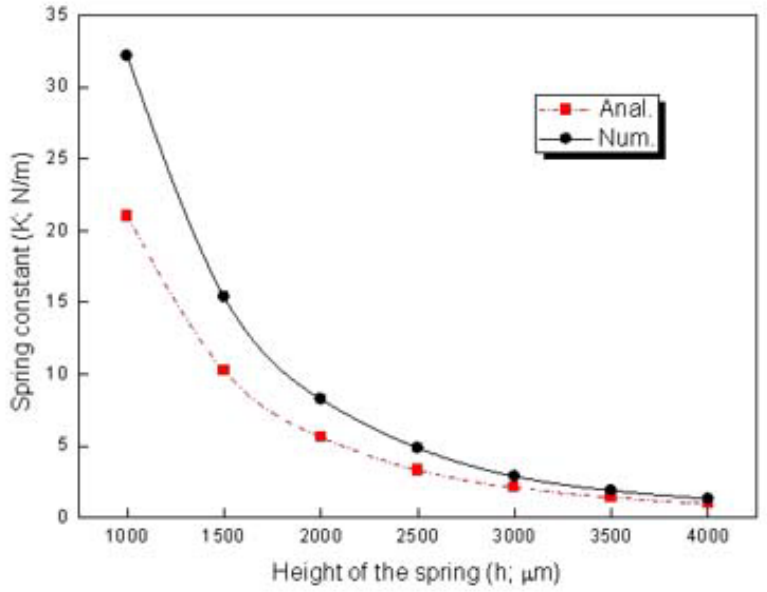

Figure 3-7 The spring constant versus the height of the spring: *N* (the number of repeated part) and t (spring thickness) are fixed at 1 and 30 μm

In Figure 3-7 the spring constant becomes smaller for larger heights of the spring marked as ‘h’ in Figure 3-4. As the difference between the calculated and simulated values becomes larger, the height of spring becomes smaller. This is due to the fact that Equation 3-11 is valid only if the height of spring is much larger than the gap of spring marked as ‘g’.

To reopen the micro-relay against possible sticking force and quickly stabilize the system in the release mode, enough spring stiffness should be considered to restore the deflected plunger. In the transducers designed for this work, two or four springs are used depending on the system properties, and the total spring constant is equivalent to the value of two or four times that of the single spring constant.

3.2.3 Viscous Air Damping

A good positioning device or actuator should be well-damped to obtain faster rising time, shorter settling times, and smaller overshoots. The motion of the thin film of air in a planar microstructure generates a squeeze-film damping that can adversely affect the dynamic response of the system due to the associated noise[72]. Squeeze film damping becomes significant if the gap spacing is small compared to the lateral dimensions of the device. Evacuating the surroundings would eliminate this effect. In addition, the excessive air damping problem can be solved by drilling perforations in one of the plates. In fact, the use of perforated plates has a double role: it reduces the squeeze-film damping effect and enhances the etching of underlying sacrificial layers in the micro-fabrication process. Thus, the perforations are compatible with the thin film processing and add very little to the manufacturing cost.

While the squeeze-film damping is reduced by incorporating holes in the plate, the motion of the air within the plate holes gives a new viscous resistance which adds to the squeeze-film damping. These two viscous effects, namely the squeeze-film damping due to the horizontal motion of air between the plates and the resistance due to the vertical motion of air through the holes are not independent [Figure 3-8]. In order to reduce the squeeze-film damping, more holes are required. However, each new hole adds its resistance to the total damping. Thus, the optimum number of perforations that minimizes the viscous damping should be considered. Recently viscous damping of perforated planar microstructures has been studied by many groups[73,74,75].

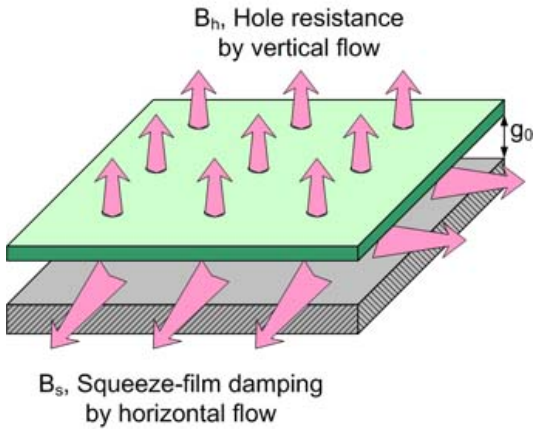

Figure 3-8 Squeeze-film damping and hole resistance in the perforated planar microstructure

- **Squeeze-film damping (B_s)**

The squeeze-film damping by horizontal flow can be derived by Reynolds gas-film equation[72,73,74,75]. In Bergqvist's model[11], the squeeze-film damping is

$$B_s = \frac{12\,\mu\,A_2^2}{n\,\pi\,g_0^3}\left(\frac{A_0}{2} - \frac{A_0^2}{8} - \frac{\ln A_0}{4} - \frac{3}{8}\right) \tag{3-12}$$

where μ is viscosity, A_2 is the plunger area, n is the total number of holes, g_0 is the initial air-gap, A_0 is the surface fraction occupied by the holes.

- **Holes' resistance (B_h)**

The calculation of the hole resistance is obtained by modeling the flow in a hole as a Poiseuille flow in a pipe, described again by a Poisson equation for velocity. In Homentcocshi's model[72], the hole-resistance is

$$B_h = \frac{8 n \pi \mu h}{A_0^2} \tag{3-13}$$

where h is the height of hole.

By adding the two terms modeling the viscous damping, the squeezing mechanical damping and the plate hole-resistance, total viscous damping is obtained as follows.

$$B = B_s + B_h = \frac{12 \mu A_2^2}{n \pi g_0^3}\left(\frac{A_0}{2} - \frac{A_0^2}{8} - \frac{\ln A_0}{4} - \frac{3}{8}\right) + \frac{8 n \pi \mu h}{A_0^2} \tag{3-14}$$

Figure 3-9 shows the relationship between the viscous damping and the hole-fraction of plunger. The physical constants associated with the device were listed in Table 3-4. As the number of holes increases, the damping coefficient becomes smaller in the given range of hole-fraction. In the case of the small air-gap, for instance 15 μm, the damping coefficient becomes larger with strong dependence on the hole-fraction. In the case of the large air-gap, however, the damping coefficient becomes smaller and the influence of the hole-fraction becomes almost negligible. Therefore, viscous damping coefficient may be ignored in the case of the device with the large air-gap and the increased hole-fraction. For this research work, the device with 25 μm air-gap and 0.0126 hole-fractions (15 holes) was chosen to allow moderate increases in damping coefficient and trouble-free

etching of the sacrificial layer. In this case the calculated total viscous damping coefficient is 0.0166 Pa·s/m^3.

Using the formulas for the squeeze-film damping and the hole-resistance[73], the optimum number of circular holes is obtained as follows

$$N_{opt} = \sqrt{\frac{3}{2hg_0^3}} \frac{A_1}{\pi} \left(\frac{A_0}{2} - \frac{A_0^2}{8} - \frac{\ln A_0}{4} - \frac{3}{8} \right)^{\frac{1}{2}} \tag{3-15}$$

In addition, the associated minimum value of the total damping coefficient is obtained as follows.

$$B_{\min} = \frac{8\sqrt{6}\mu A_2}{A_0} \sqrt{\frac{h}{g_0^3}} \left(\frac{A_0}{2} - \frac{A_0^2}{8} - \frac{\ln A_0}{4} - \frac{3}{8} \right)^{\frac{1}{2}} \tag{3-16}$$

Using these equations, the optimum number of circular holes (N_{opt}) is calculated to be 51 and the associated minimum value of the total damping coefficient (B_{min}) is 0.0077 Pa·s/m^3. These values are the results of compromise between the squeeze-film damping and the hole-resistance.

Table 3-4 Design constant associated with the device

Parameters	Value
Air viscosity (μ)	1.583×10^{-5} kg/m·s
Hole area (A_1)	1.06×10^{-7} m^2
Plunger area (A_2)	8.4×10^{-6} m^2
hole fraction (A_0)	0.0126
Total number of holes (n)	15
Initial air gap (g_0)	$15\text{-}45\times10^{-6}$ m
Height of hole (h)	30×10^{-6} m

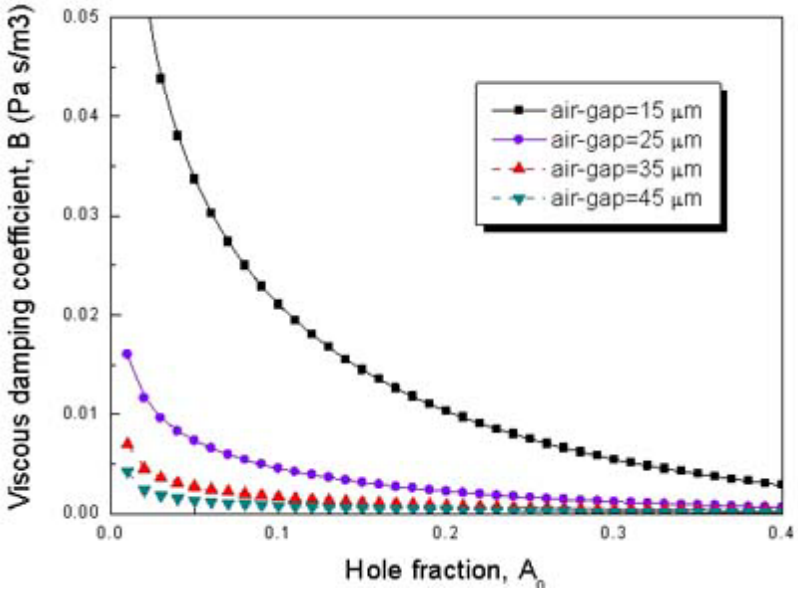

Figure 3-9 The function of viscous air damping and hole fraction

3.3 Micro-power Relay

3.3.1 Static Analysis

Let us now apply these fundamental equations to the simple electrostatic actuator by adding a spring between the movable plate and the fixed support. The instantaneous electrostatic force *F* working on the armature suspended by the flat springs [Figure 2-4] can be expressed as Equation 3-8. In actual applications, the actuator is usually attached to a load against which it performs work. In most cases, the load can be modeled by a mass-spring system. A simple spring-actuator configuration is shown in Figure 3-10. The mass moves in response to a pure mechanical force which is due to the spring force and the damping force, and a force of electric origin which is due to the attractive electrostatic force.

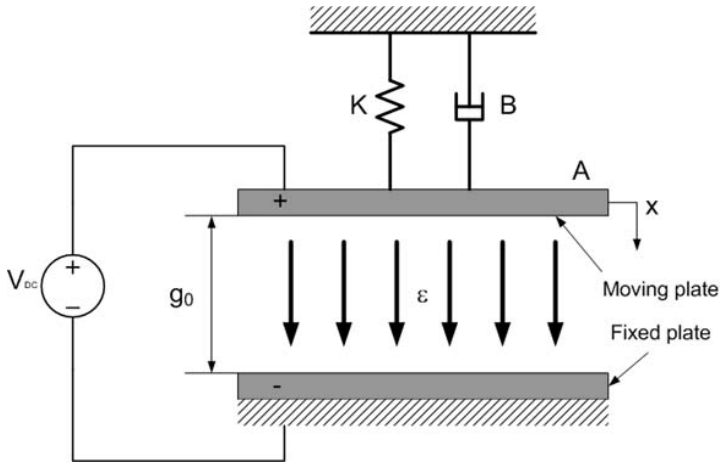

Figure 3-10 A schematic of a simple electrostatic actuator configuration. A movable capacitor plate attached to a spring: spring constant (*K*), damping coefficient (*B*), mass of moving plate (*M*), voltage (*V*), initial air gap (g_0), surface area (*A*), and electric permittivity (ε)

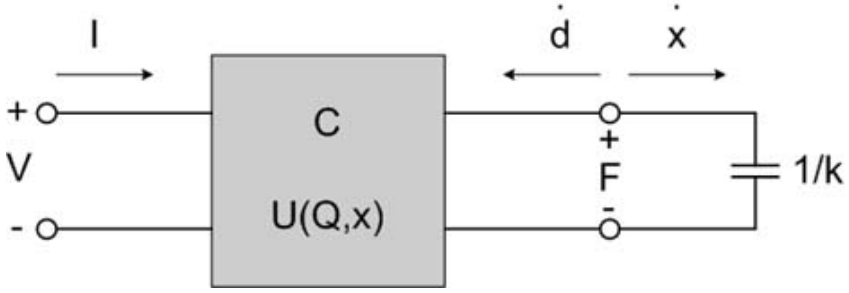

Figure 3-11 The circuit element model of the simple electrostatic actuator with two ports: an electrical port with voltage (*e*) and current (*I*) as the conjugate variables, and a mechanical port with force (*F*) and velocity ($\dot{x}$) as the conjugate variables

Figure 3-11 illustrates the equivalent circuit element model of the simplified electrostatic actuator. For the reason of simplicity, the damping coefficient B of the system is assumed to be zero. In this configuration, the electrostatic actuator performs work only against the spring. Now, this system can be analyzed with equations given in the previous section. Obviously the gap is obtained from

$$g = g_0 + \int \dot{g}\, dt \tag{3-17}$$

where g_0 is the gap in the neutral position (initial air-gap) between the spring force and the electrostatic force. Since the relationship between $\dot{g}$ and $\dot{x}$ is given as

$$\dot{g} = -\dot{x}, \tag{3-18}$$

the integral for $\dot{g}$ must simply yield -*x*. Therefore, Equation 3-17 is obtained as follows.

$$g = g_0 - x \tag{3-19}$$

Substitution of Equation 3-7 into 3-9 and then Equation 3-9 into 3-19 gives the equation in terms of charge Q:

$$g = g_0 - \frac{Q^2}{2\varepsilon AK} \tag{3-20}$$

and the voltage across the capacitor at the electrical port is

$$V = \frac{Qg}{\varepsilon A} = \frac{Q}{\varepsilon A}\left(g_0 - \frac{Q^2}{2\varepsilon AK}\right) \tag{3-21}$$

On the other hand, substitution of Equation 3-8 into 3-9 and Equation 3-9 into 3-19 gives the equation in terms of voltage V:

$$g = g_0 - \frac{\varepsilon AV^2}{2Kg^2} \tag{3-22}$$

and the voltage across the capacitor at the electrical port is

$$V = \frac{Qg}{\varepsilon A} = \frac{Q}{\varepsilon A}\left(g_0 - \frac{\varepsilon AV^2}{2Kg^2}\right) \tag{3-23}$$

Generally, an electrostatic actuator is controlled by voltage [Equation 3-22 and 3-23] rather than charge [Equation 3-20 and 3-21]. As the voltage increases in the voltage controlled system, the gap decreases with the amount of decrease-growing as the gap gets smaller. Thus, there is a positive feedback in this system, and at some critical voltage (pull-in voltage) the system goes unstable, and gap collapses to zero. The net force on the

upper plate at voltage V and gap g, using a sign convention that assigns a positive sign for forces that increase the gap, is

$$F_{net} = -\frac{\varepsilon A V^2}{2g^2} + K(g_0 - g) \tag{3-24}$$

where g_0 is the gap at zero volts and zero spring extension. At a point of equilibrium, F_{net} is zero. For the small perturbation of the gap to $g+\delta g$, δF_{net} is

$$\delta F_{net} = \frac{\partial F_{net}}{\partial g}\delta g = \left(\frac{\varepsilon A V^2}{g^3} - K\right)\delta g \,. \tag{3-25}$$

If δF_{net} is positive for positive δg, then g is an unstable equilibrium point because a small increase δg creates a force tending to increase it further. If δF_{net} is negative, then g is a stable equilibrium point. In order for g to be a stable equilibrium, the expression in parenthesis must be negative, which means that

$$K > \frac{\varepsilon A V^2}{g^3} \,. \tag{3-26}$$

Since the equilibrium gap decrease with increasing voltage, there will be a specific voltage at which the stability of the equilibrium is lost. This is defined as the pull-in voltage (V_{PI}). When pull-in occurs, there is an unbalance between electrostatic force and spring force, which is compensated by a reaction force when the movable part hits in final position. This effect also limits the dynamic range of capacitive accelerometers. This inherent instability is a common phenomenon associated with electrostatic MEMS devices and extensively studied[76,77]. At pull-in, there are two equations that must be satisfied: the original requirement $F_{net} = 0$ and new requirement

$$K = \frac{\varepsilon A V_{PI}^2}{g_{PI}^3} \tag{3-27}$$

It is readily shown[10,78] that the pull-in occurs at

$$g_{PI} = \frac{2}{3} g_0 \tag{3-28}$$

and the equilibrium voltage is at this gap

$$V_{PI} = \sqrt{\frac{8Kg_0^3}{27\varepsilon A}} . \tag{3-29}$$

Figure 3-12 shows the pull-in voltage of the device with different suspension stiffness. The pull-in voltage of the device using a different gap-size is depicted in Figure 3-13. As can be seen, the initial gap-size has a large effect on the pull-in voltage. Thus, the initial gap-size should be carefully considered at the beginning of the design step. The definition of the parameters and the values used for analysis are given in Table 3-5.

Table 3-5 Parameters used in the modeling of the relay

Parameters	Value
Plunger area (A)	4×10^{-6} m^2
Electric permittivity (ε)	8.85×10^{-12} F/m
Initial air-gap (g_0)	25 μm
Spring constant (K)	19.4 N/m

An additional insight can be obtained from the pull-in phenomenon by examining the two components of δF_{net} graphically. It is helpful to use two normalized variables: the normalized voltage to the pull-in voltage and the normalized displacement of the plate from its equilibrium position, using g_0 as the normalization constant.

$$v = \frac{V}{V_{PI}} \tag{3-30}$$

$$\xi = 1 - \frac{x}{g_0} \tag{3-31}$$

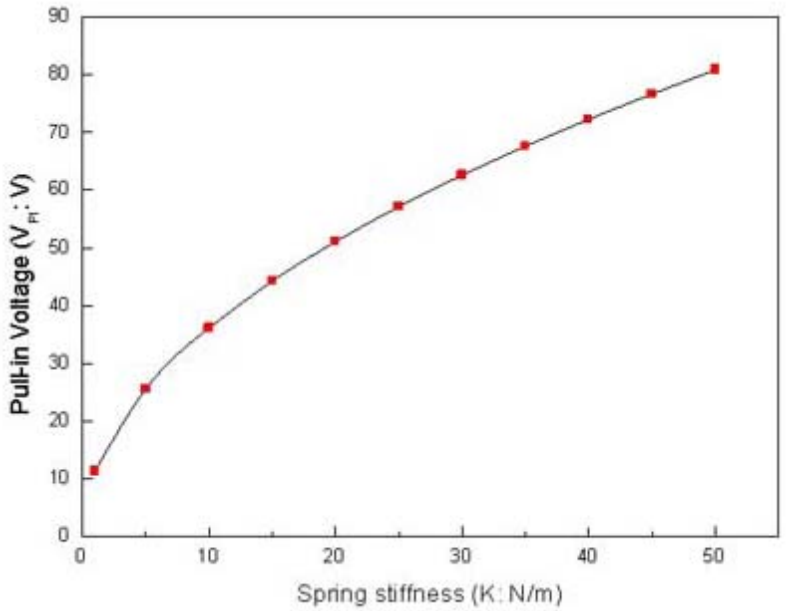

Figure 3-12 Pull-in voltage(V_{PI}) versus spring stiffness(K): The initial air-gap is fixed at the value of 25 μm

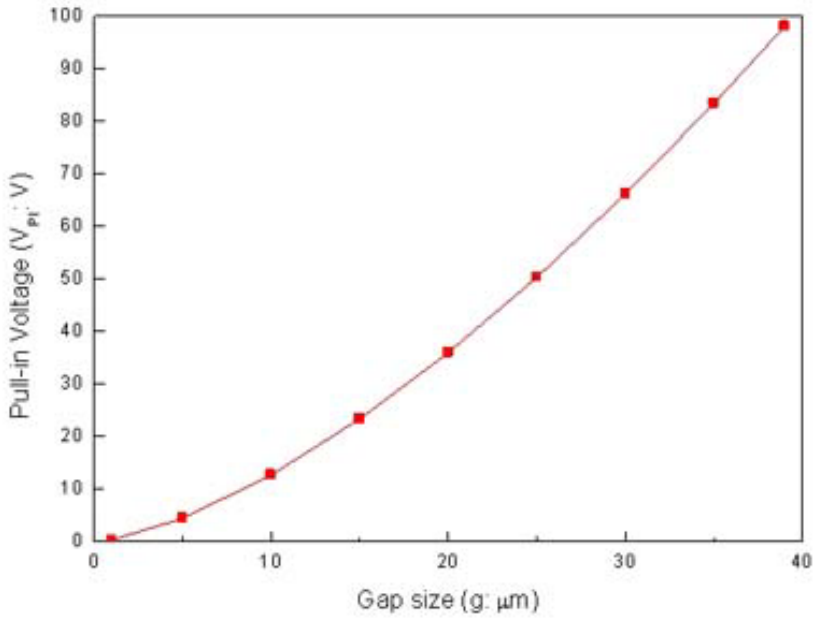

Figure 3-13 Pull-in voltage(V_{PI}) versus gap size(g): The spring stiffness is fixed at the value of 19.4 N/m

Since the condition for equilibrium is $F_{net}=0$, substitution of Equation 3-30 and 3-31 into 3-24 gives

$$\frac{4}{27}\frac{v^2}{\left(1-\xi^2\right)}=\xi\,. \tag{3-32}$$

Figure 3-14 shows the two sides of this equation (normalized electrostatic force and spring force) plotted simultaneously. The series of electrostatic force-ξ curves were generated with the applied voltage of *19.3* to *50* volts, with *7.7* volt increment for the calculated value of $V_{PI}=50$ *volts* by using the given constants in Table 3-5. The spring-suspension force increases linearly with armature displacement until the armature comes into contact with the electrodes on the bottom part, while the electrostatic force increases nonlinearly. The net force actuated on the armature is the difference between the electrostatic attraction force closing the gap and the spring-suspension force that pulls the armature to the initial position. When the relay is driven to the closed position, the armature makes the physical contact on the electrodes on bottom part to switch on. The excess force helps to maintain good electrical contact and a low electrical resistance across the switch[79]. As the voltage is increased in Figure 3-14, the two equilibrium points move toward each other, and finally merges when $\xi=1/3$ and $v=1$. This represents the minimum pull-in voltage required for the electrostatic plates to snap across the air-gap. For example, when an actuation voltage of v=0.846 is applied, this suspension stiffness would result in a mechanical restoring force that equals to the electrostatic force at a displacement of ξ=0.15. Using the same analogy, the suspension stiffness required for different pull-in voltages can be determined. For normalized voltages greater than 1, the curves never intersect, and there is no stable equilibrium.

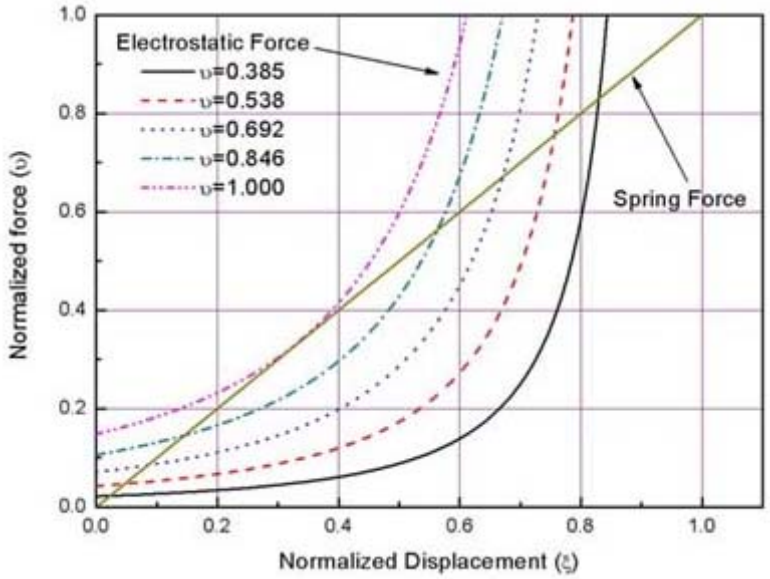

Figure 3-14 Electrostatic force and spring force for the electrostatic actuator plotted at *V=19.3, 26.9, 34.6, 42.3, and 50 volts*

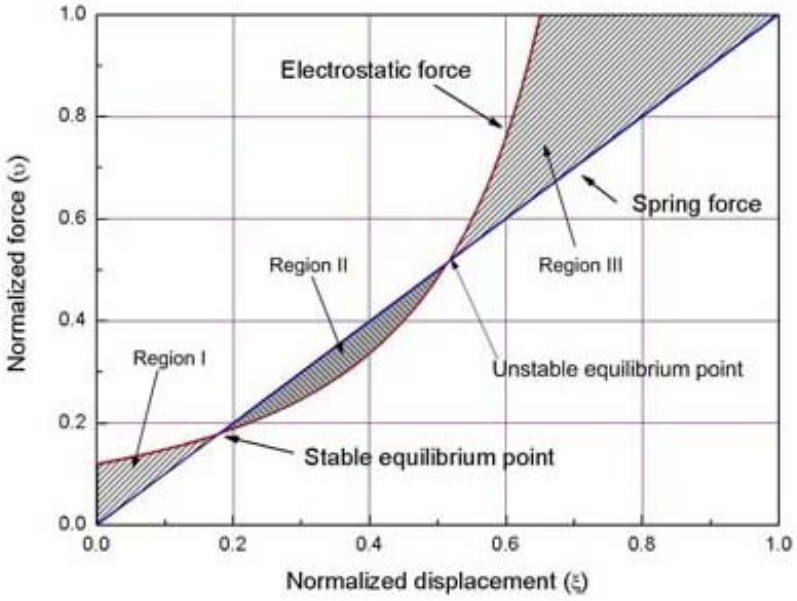

Figure 3-15 The energy comparison of the relay as a function of the plunger displacement

Although there are two intersections between the electrostatic force and the spring force, only one of them is stable. The stable solution can be seen from the energy point of view as shown in Figure 3-15. This analysis is very similar to Williams' work on electromagnetic relays[80]. As the electrostatic and spring forces increase, three unique regions are formed as marked in the Figure 3-15 as region I, II, III. In region I, the electrostatic force is larger than the spring force and the net force on the plunger drives it to move downward. The work energy done is equal to the area in region I. This work energy is converted to kinetic energy of the plunger at the moment when the two plots intersect at the stable equilibrium point. After the plots pass this point and entered region II, the spring force is larger than the electromagnetic force and the top plate of the relay decelerates while a downward motion is still maintained. After the plots reach at the unstable equilibrium point, the nonlinearly increasing electrostatic force becomes much larger than spring restoring force and the top plate is quickly accelerated to close the relay. This is the reason why this point is unstable. In order for the relay to close, the area representing the energy difference in region I must be greater than the area represented in region II. If the area in region II exceeds that of region I, then the velocity of the relay becomes negative, this means that spring force pulls the plunger to move up and the relay does not close. Furthermore, as region II grows larger, the displacement of the plunger becomes smaller and smaller leading to higher frequency harmonic oscillations. This particular operation mode can be used for an accelerometer.

Another way to explore pull-in is to make a graph of the normalized equilibrium gap as a function of normalized voltage. Using these variables, the condition for equilibrium is obtained as,

$$\frac{4}{27}v^2 = (1-\xi)\xi^2 . \tag{3-33}$$

This is shown in Figure 3-16 with stable displacements occurring for normalized gaps greater than 2/3, and unstable collapse to zero-gap occurring once the pull-in voltage is reached.

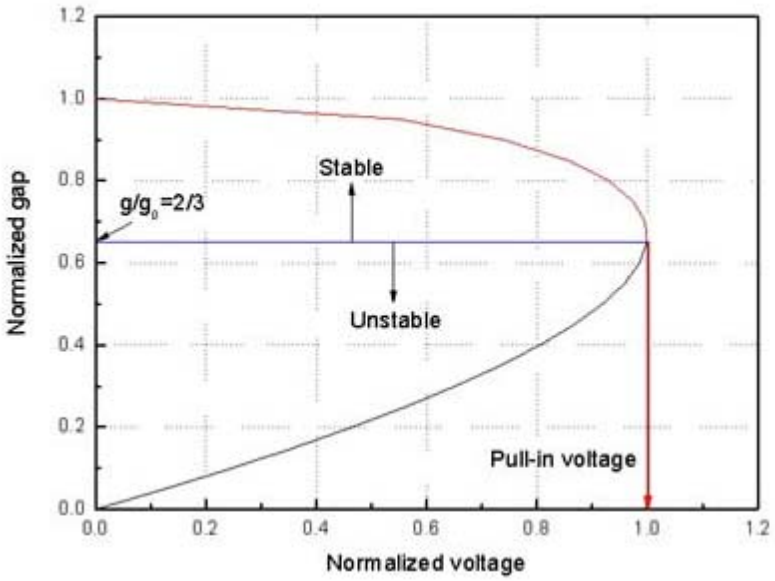

Figure 3-16 Normalized gap as a function of normalized voltage for the electrostatic actuator

3.3.2 Dynamic Analysis

The choice of methods for analyzing the dynamics of a lumped-element system depends critically on whether or not the system is linear. A linear system such as a spring-mass-dashpot system is characterized by state equations that depend only on the first powers of the various state variables. In this case all linear-system methods can be used such as Laplace transform, s-plane analysis with poles and zeros, Fourier transform, convolution, superposition, and eigenfunction analysis.

In our case, the voltage-controlled parallel-plate electrostatic actuator is a nonlinear system. In this approach, the state variables which are the time derivatives of a set of variables describing the state are identified, and a set of coupled first-order differential equations are written for the system. For complete analysis of dynamic behavior, three components dictating the system dynamical behavior were considered. Mass represents the mechanical inertia of the moving plate, and a dashpot captures the mechanical damping forces that arise from the viscosity of the air that must be squeezed out when the plates move together and drawn in when the plates move apart. The other component is a source resistor for the voltage source that drives the actuator. This system was modeled as shown in Figure 3-17. Figure 3-18 also shows the equivalent circuit element model for the relay. It is clear from the equivalent circuit that the system can be demonstrated with two domains: the electrical domain with voltage and current and the mechanical domain with force and velocity.

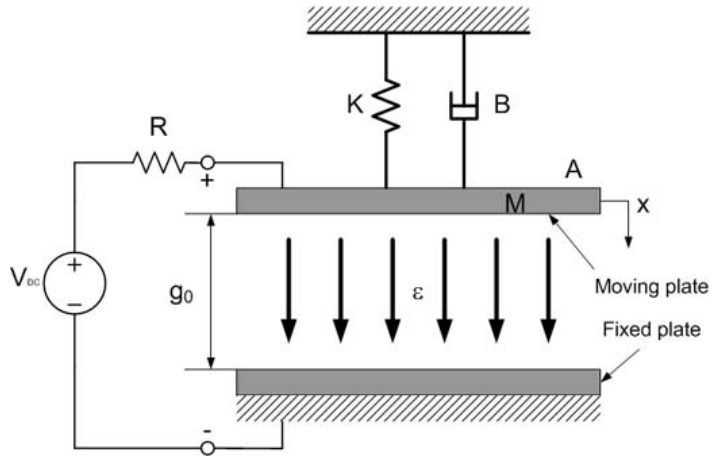

Figure 3-17 Schematic of a complete electrostatic actuator configuration with added elements representing the inertia of the movable element, mechanical damping, and the source resistance of the electrical network

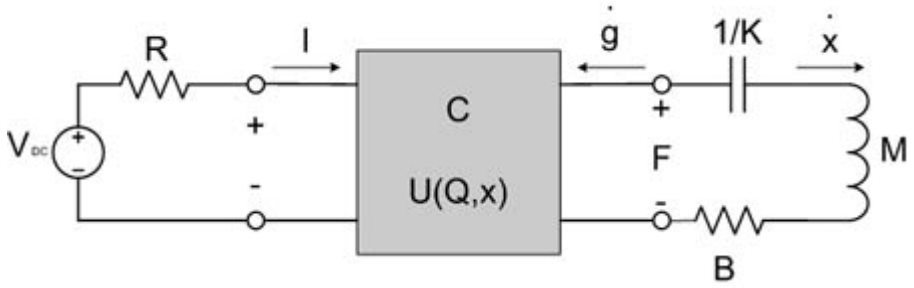

Figure 3-18 The circuit element model of the complete electrostatic actuator with two ports

The governing equations for this actuator are obtained from Kirchhoff's Voltage Law* equations in the two domains, and manipulated into the state equation forms. For the electrical domain:

$$V_{DC} = V_{\mathrm{Re}\,sistor} + V_{Capacitor} \tag{3-34}$$

Substitution of Equation 3-6 into 3-34 gives 3-35 where x is replaced for g.

$$\dot{Q} = I = \frac{1}{R}\left(V_{DC} - \frac{Qx}{\varepsilon A}\right) \tag{3-35}$$

For the mechanical domain, using the force balance, we obtain

$$M\ddot{x} + B\dot{x} + K\left(x - g_0\right) + \frac{Q^2}{2\varepsilon A} = 0\,. \tag{3-36}$$

To get this equation into state form, we must identify three state variables. If we select state variables as follows,

$$x_1 = Q \tag{3-37}$$

$$x_2 = x \tag{3-38}$$

$$x_3 = \dot{x}_2 = \dot{x}\,, \tag{3-39}$$

then the state equations become:

* The oriented sum of all voltage (efforts) around any closed path is zero

$$\dot{x}_1 = \frac{1}{R}\left(V_{DC} - \frac{x_1 x_2}{\varepsilon A}\right) \tag{3-40}$$

$$\dot{x}_2 = x_3 \tag{3-41}$$

$$\dot{x}_3 = -\frac{1}{M}\left(\frac{x_1^2}{2\varepsilon A} + K(x_2 - g_0) + Bx_3\right). \tag{3-42}$$

In this case, the input is the voltage V_{DC} and the output can be considered to be any desired function of the three state variables. These nonlinear state equations can be integrated numerically using the ode command in MATLAB. Alternatively, a system block-diagram can be constructed in SIMULINK, and simulations can be performed in that environment[44]. A SIMULINK model that implements these equations is shown in Figure 3-19. The definition of the parameters and the values used for the simulations are given in Table 3-6. The triangular waveform is applied to the V_{DC} and observed to see how the system evolves.

Table 3-6 Parameters used in the modeling of the relay

Parameters	Value
Plunger area (A)	4×10^{-6} m^2
Electric permittivity (ε)	8.85×10^{-12} F/m
Initial air-gap (g_0)	25 μm
Minimum gap (g_{min})	0.01 μm
Density (ρ)	8.9×10^{3} kg/m^3
Volume (v)	2.52×10^{-10} m^3
Mass (M)	2.24×10^{-6} kg
Damping coefficient (B)	0.0143 Pa·s/m^3
Spring constant (K)	19.4 N/m
Resistance (R)	0.01 Ω

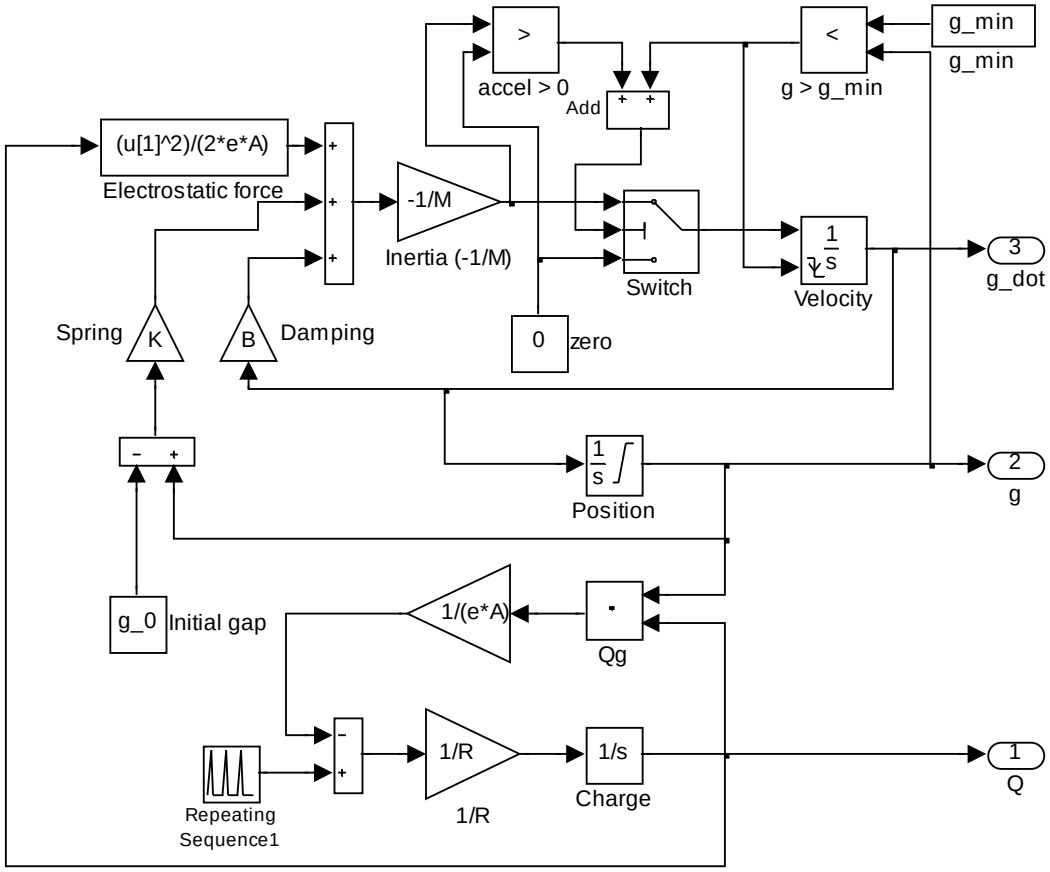

Figure 3-19 SIMULINK implementation of state equations for the parallel-plate electrostatic actuator

The pull-in voltage is in very good agreement with analytical result in static analysis. For the parameters selected, the analytical pull-in voltage is 50 volts. Figure 3-20 shows the driving voltage waveform together with the output for the charge *Q*. Because of the existence of resistance *R*, there is a 2 ms of time delay between the applied voltage and the appearance of the charge on the plate. The displacement as a function of time is shown in Figure 3-21. It can be seen that behaviors of pull-in and release depend on accumulated charge.

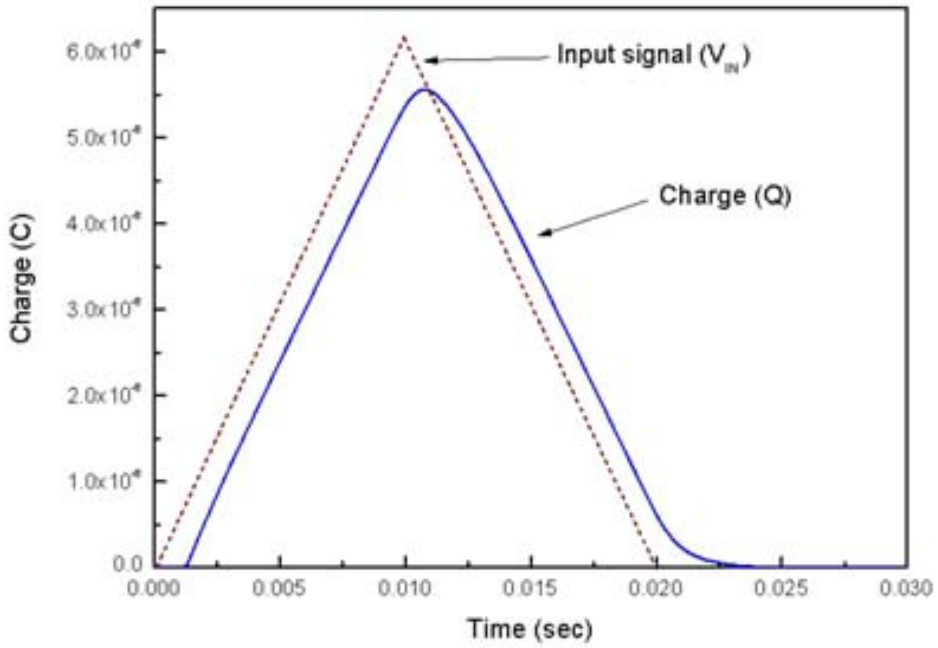

Figure 3-20 The input signal and output charge: the time lag is about 2μsec

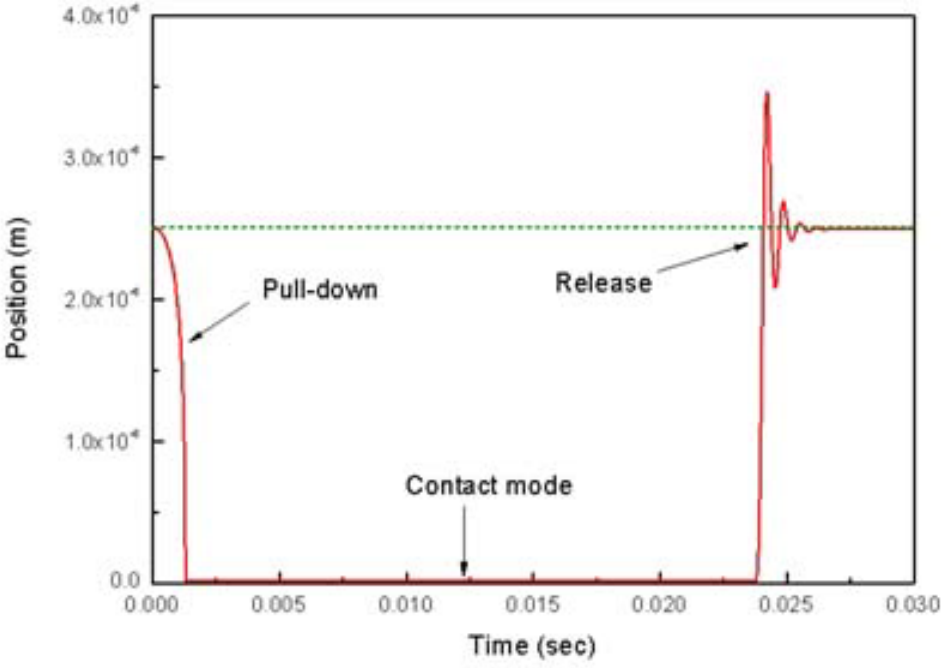

Figure 3-21 Position of the moving plate as a function of time

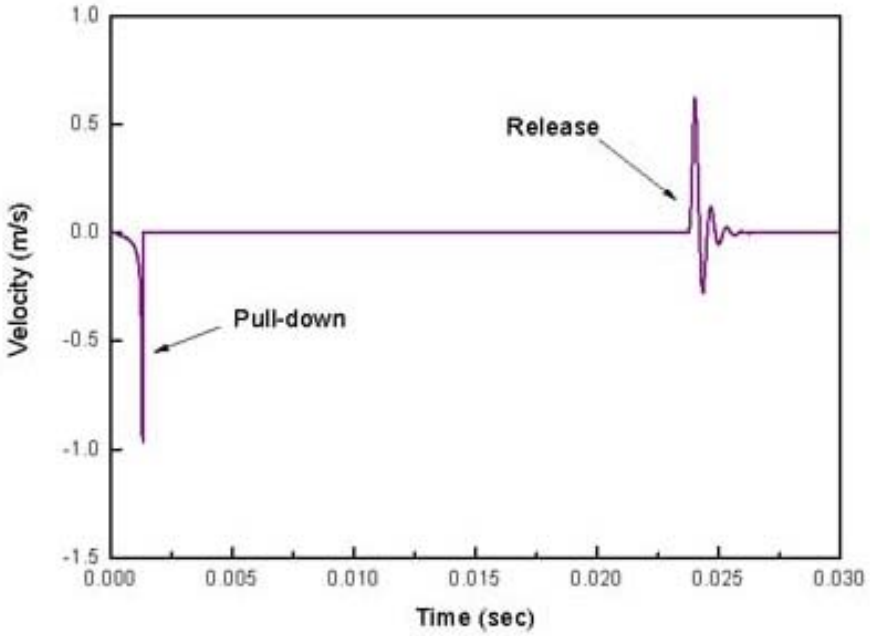

Figure 3-22 Velocity of the moving plate as a function of time

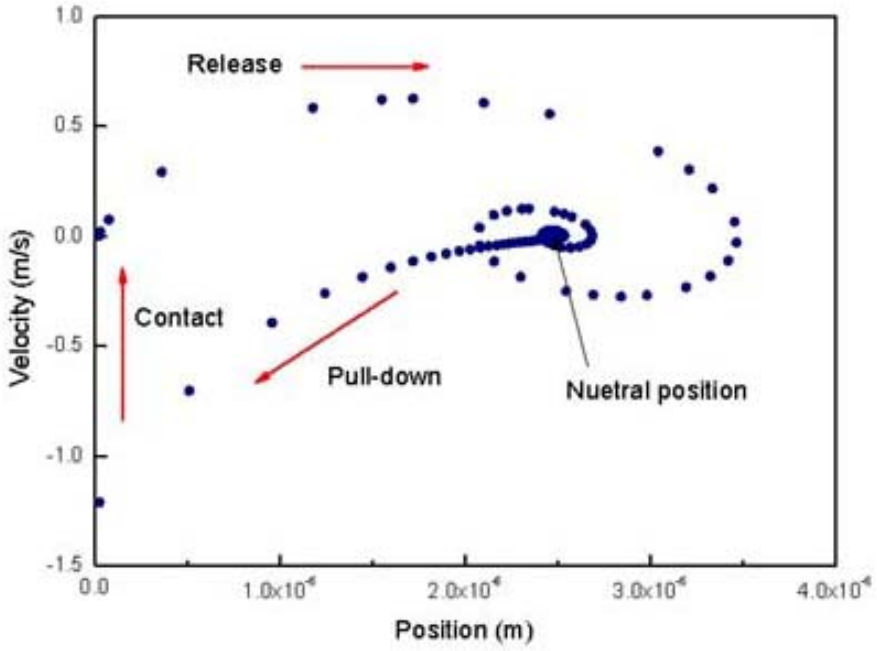

Figure 3-23 Phase-plane plot: velocity of the moving plate as a function of position

During the release phase, there is ringing motion as the plate pops up and oscillates about its equilibrium position. If required, the third capacitive plate above the spring suspension can be used to avoid this oscillatory motion. The additional electrostatic force may attract the top plate to its equilibrium position quickly. The corresponding velocity as a function of time is shown in Figure 3-22. The crash-reset of the velocity to zero at the moment of pull-in is evident. The ringing on release phase is also very clear.

In Figure 3-23, the phase-plane plot of velocity versus position shows the cycle of pull-in, crash, and release. The ringing on release appears as cyclic motion about the final rest position.

In the previous studies, the actuator was considered to be a rigid body. However, if the stiffness of the relay is important, resonance mode shapes should be considered. The first three modes of resonance were analyzed by using the suspension stiffness of 45.5 N/m which corresponds to the value of 77.13 pull-in voltage. The first mode represents Z-axis planar displacement of the moving electrostatic plate [Figure 3-24 (a)]. The second and third mode represents the out-of-plane rotation of the plate about its axes of symmetry [Figure 3-24 (b) and (c)]. The first, second, and third mode resonances occur at 773.2, 1225.0, and 1264.8 Hz respectively. The slight difference of about 3% between the second and third mode frequency is due to the rectangular shape of the moving plate and the orientation of the serpentine spring anchor points.

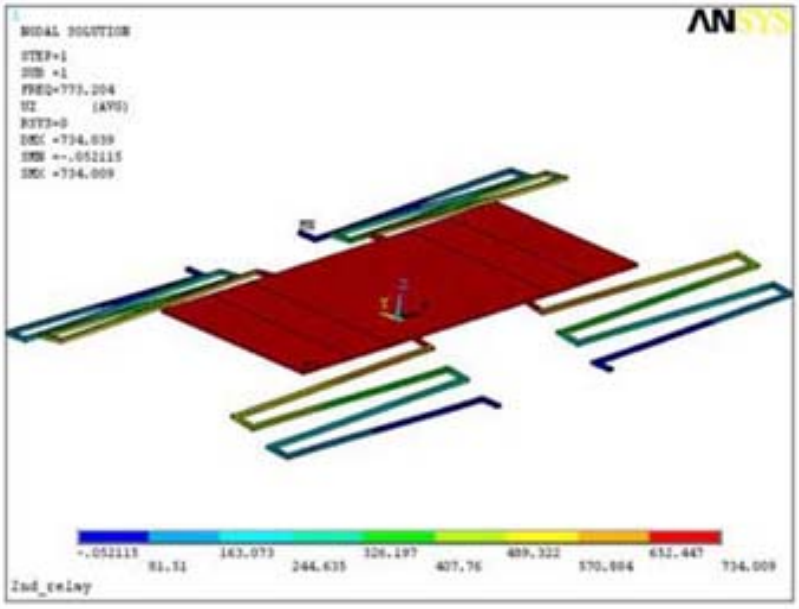

a) First resonance mode shape at ω_n=773.2 *Hz*

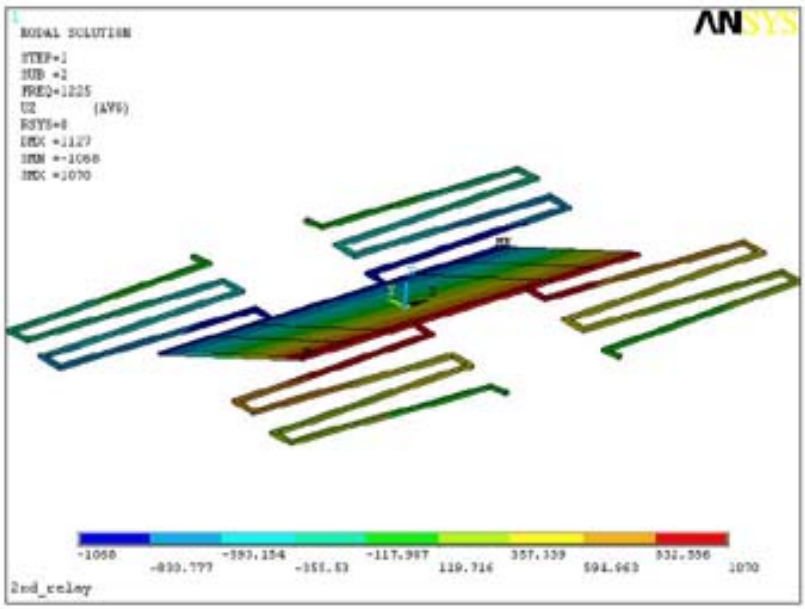

b) Second resonance mode shape at ω_n=1225.0 *Hz*

Figure 3-24 Resonance mode shapes of the device with 45.5N/m spring stiffness

Figure 3-24 continued

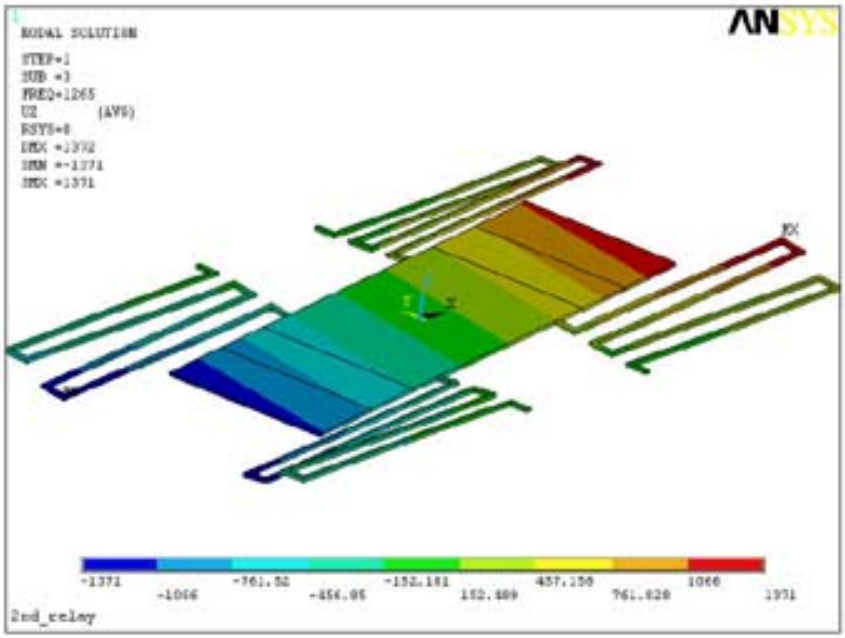

c) Third resonance mode shape at ω_n=1264.8 *Hz*

3.4 Micro-accelerometer

As shown in Figure 3-25, the simplest model of an accelerometer is a mass-spring-damper system that is attached to a protective housing. The measurement of acceleration relies on classical Newton's mechanics. The applied acceleration of the housing causes the proof mass (also referred to seismic mass) to move, and this vertical motion can be used to determine the magnitude of the acceleration. Some form of damping is required; otherwise the system would oscillate at its natural frequency for any input signal. To derive the dynamic equation of the system, D' Alembert's principle is applied, where all real forces acting on the proof mass are equal to the inertia force on the proof mass.

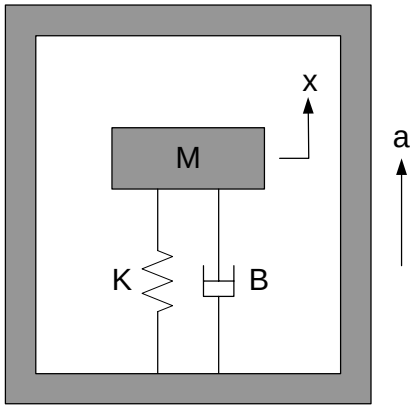

Figure 3-25 Accelerometer sensing principle

For the purpose of simplicity, the electrostatic force that may be induced by the voltage induced during the measurement is neglected. Then the displacement of the mass, x_m, the displacement of the housing, x_h, and the relative displacement of mass with respect to housing can be expressed as

$$x_m = x_h + x_r \tag{3-43}$$

where x_r is relative displacement of the mass. Then the dynamic equation describing the system can then be derived as follows:

$$M\frac{d^2x_m}{dt^2} + B\frac{dx_r}{dt} + Kx_r = 0 \tag{3-44}$$

where M is seismic mass, B is damping coefficient, and K is spring constant. Substituting Equation 3-43 into 3-44 yields

$$M\left(\frac{d^2x_k}{dt^2} + \frac{d^2x_r}{dt^2}\right) + B\frac{dx_r}{dt} + Kx_r = 0\,. \tag{3-45}$$

For the input function of $x_h=A\sin\omega t$, the absolute value of the resulting acceleration of the housing is $\frac{d^2x_h}{dt^2} = A\omega^2 \sin\omega t$, and then the acceleration input is determined by measuring x_r (the net stretch or compression of the spring),

$$M\frac{d^2x_r}{dt^2} + B\frac{dx_r}{dt} + Kx_r = F_0 \sin\omega t \,, \tag{3-46}$$

where F_0 is $MA\omega^2$. This is well known equation for the damped forced vibration. The transient solution and steady state solution can be derived as

$$\left(x_r\right)_{transient} = \begin{cases} A_1 e^{-\zeta\omega_n t}\sin\omega_d t + B_1 e^{-\zeta\omega_n t}\cos\omega_d t; & \zeta < 1 \\ A_2 e^{-\omega_n t} + B_2 t e^{-\omega_n t}; & \zeta = 1 \\ A_3 e^{\left(-\zeta+\sqrt{\zeta^2-1}\right)\omega_n t} + B_3 e^{\left(-\zeta-\sqrt{\zeta^2-1}\right)\omega_n t}; & \zeta > 1 \end{cases}, \tag{3-47}$$

$$\left(x_r\right)_{steady} = \frac{F_0/K\sin\left(\omega t-\phi\right)}{\left\{\left[1-\left(\omega/\omega_n\right)^2\right]^2 + \left[2\zeta\left(\omega/\omega_n\right)^2\right]^2\right\}^{1/2}} \,, \tag{3-48}$$

where the constants are given by

$$A_1 = \frac{v_0 + \zeta\omega_n x_0}{\omega_d} \tag{3-49}$$

$$B_1 = x_0 \tag{3-50}$$

$$A_2 = x_0 \tag{3-51}$$

$$B_2 = v_0 + \omega_n x_0 \tag{3-52}$$

$$A_3 = \frac{v_0 + \left(\zeta + \sqrt{\zeta^2-1}\right)\omega_n x_0}{2\omega_n\sqrt{\zeta^2-1}} \tag{3-53}$$

$$B_3 = \frac{-v_0 - \left(\zeta - \sqrt{\zeta^2 - 1}\right)\omega_n x_0}{2\omega_n \sqrt{\zeta^2 - 1}} \tag{3-54}$$

Then, the complete solution is given by

$$x_r = (x_r)_{transient} + (x_r)_{steady} . \tag{3-55}$$

Dynamic response of the accelerometer model for a given input was obtained using the MATLAB [Figure 3-26 to Figure 3-29], and the programmed MATLAB code was attached in APPENDIX B. The definition of the parameters and the values used for calculations were given in Table 3-7. The calculated system response was summarized in Table 3-8. Figure 3-26 shows displacement of the moving plate as a function of time. To avoid resonance phenomenon, the accelerometer should be operated out of range of the natural frequency of the system with a damper. The corresponding velocity and acceleration as a function of time were shown in Figure 3-27 and Figure 3-28. An accurate plot of the magnification factor M versus the frequency ratio ω/ω_n for the damping ratio ζ=0.49 was shown in Figure 3-29. If a motion amplitude is excessive, two possible remedies would be: to increase the damping to obtain a larger value of ζ, or to alter the driving frequency so that ω is farther from the resonance frequency ω_n. However, the addition of damping is most effective near resonance frequency. If the damping coefficient B of the system is assumed to be zero, and then the natural frequency of the system is the undamped natural frequency ω_n which can be used to estimate the response speed of the system. This represents the maximum frequency the system can be driven. Then the equivalent capacitance of the accelerometer can be expressed as

$$C = \frac{\varepsilon A}{\left(g_0 - x_r(t)\right)} \tag{3-56}$$

where A is the cross-sectional area of the capacitor and ε is the dielectric constant of air.

Table 3-7 Parameters used in the modeling of the accelerometer

Parameters	Value
Plunger area (A)	4×10^{-6} m^2
Initial air-gap (g_0)	25 μm
Mass (M)	7.14×10^{-7} kg
Damping coefficient (B)	0.0016 Pa·s/m^3
Spring constant (K)	3.7 N/m
Force amplitude (F_0)	5×10^{-6}
Driving frequency (ω)	1.0 kHz
Initial velocity (v_0)	1.0 μm/s
Initial position (x_0)	25 μm

Table 3-8 Summary of the system response

System parameters	Equation	Value
Natural frequency	$\omega_n = \sqrt{\frac{K}{M}}$	2.27 kHz
Damping ratio	$\zeta = \frac{B}{2\sqrt{KM}}$	0.49
Phase angle	$\phi = \tan^{-1}\frac{2\zeta(\omega/\omega_n)}{1-(\omega/\omega_n)^2}$	0.4923 rad
Damped natural frequency	$\omega_{nd} = \sqrt{\frac{K}{M} - \left(\frac{B}{2M}\right)^2}$	1.98 kHz
Damped period	$\tau_d = \frac{2\pi}{\omega_{nd}} = \frac{2\pi}{\omega_{nd}\sqrt{1-\zeta^2}}$	3.175 ms

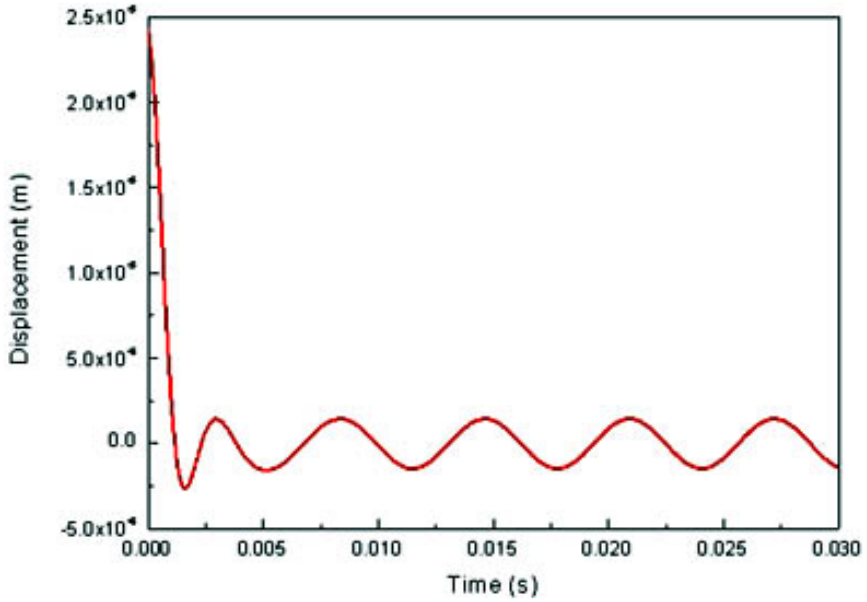

Figure 3-26 Displacement of the moving plate as a function of time

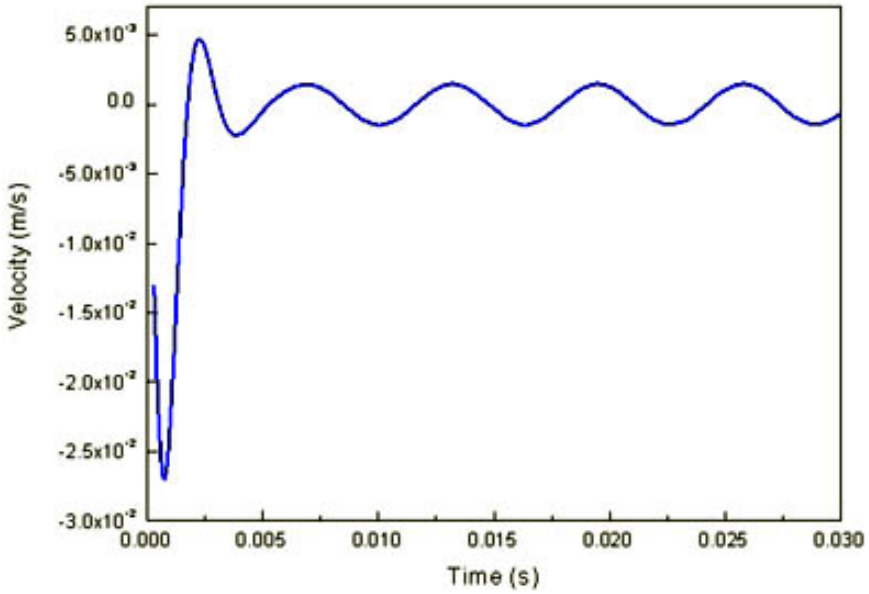

Figure 3-27 Velocity of the moving plate as a function of time

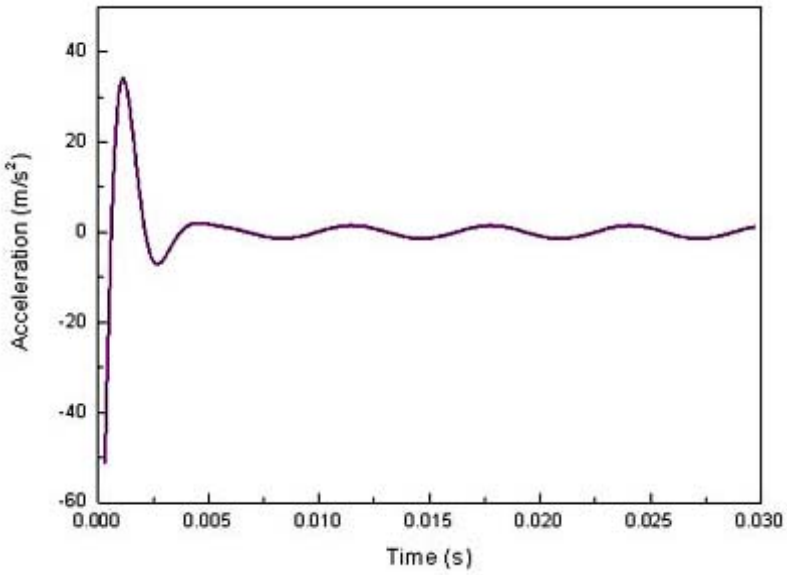

Figure 3-28 Acceleration of the moving plate as a function of time

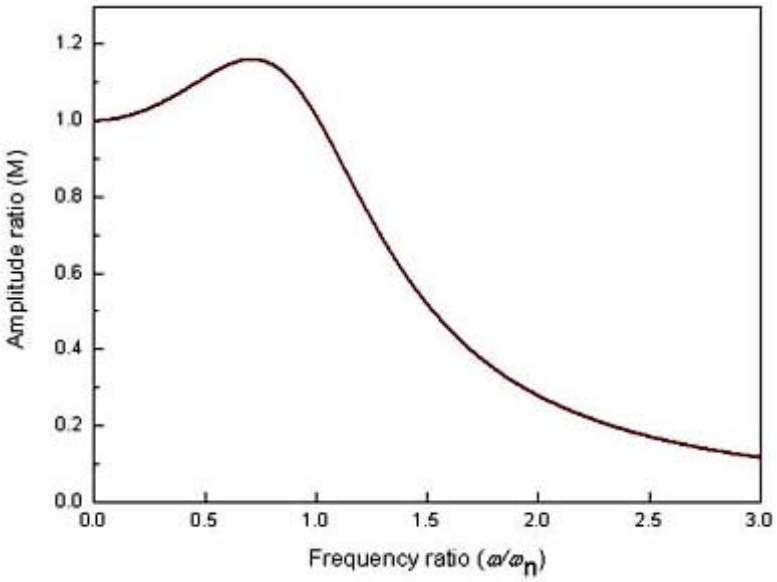

Figure 3-29 The magnification factor versus the frequency ratio at ζ=0.49

In addition, two important performance parameters can be introduced: a) minimum detectable acceleration or sensitivity and b) bandwidth estimation.

- **Sensitivity**

With a constant acceleration *a*, Equation 3-46 can be rewritten as

$$\ddot{x}_r + 2\zeta\omega_n\dot{x}_r + \omega_n^2 x_r = a \tag{3-57}$$

Then, the steady state response is $x=a/\omega_n^2$. In other words, the steady state net stretch or compression of the spring is directly proportional to the applied acceleration. If we set the minimum measurable spring deflection is x_{min}, the minimum detectable acceleration of the accelerometer is given by

$$a_{\min} = x_{\min}\omega_n^2 \tag{3-58}$$

and the sensitivity is defined by

$$S = \frac{\Delta x}{a} = \frac{M}{K} \tag{3-59}$$

The sensitivity of the designed accelerometer was calculated as 1.94×10^{-7}, and inversely proportional to the resonance frequency in the sensing direction.

- **Bandwidth**

Let the applied acceleration be a sinusoid with circular frequency ω, i.e., $a=F_0 sin\omega t$. The steady-state deflection of the spring is of the form $x = X\sin(wt-\phi)$ as shown Equation 3-48. The deflection magnitude X is related to the magnitude of the applied acceleration F_0 by

$$X = \frac{F_0 / K}{\left\{\left[1-(\omega/\omega_n)^2\right]^2 + \left[2\zeta(\omega/\omega_n)^2\right]^2\right\}^{1/2}} \tag{3-60}$$

As indicated by Equation 3-60, X depends on the driving frequency ω. In particular, X becomes diminishingly small when ζ is sufficiently large, and the accelerometer will cease to be useful at such a frequency. In practice, the bandwidth within which the accelerometer is useful is given by the cutoff frequency ω_c. This frequency is defined by the equation:

$$\frac{X(\omega_c)}{X(0)} = \frac{1}{\sqrt{2}} \tag{3-61}$$

and is given by

$$\omega_c = \gamma \omega_n \tag{3-62}$$

where

$$\gamma = \sqrt{1 - 2\zeta^2 + \sqrt{\left(1 - 2\zeta^2\right)^2 + 1}} \tag{3-63}$$

The bandwidth of the designed accelerometer was calculated as 2.9 kHz. Stiffer springs help to provide very high response speed to the system. The design of the spring is limited mainly by required accelerometer speed and the fabrication technology, and also affected by the possible deflection caused by the weight of the armature. Because the thickness of the micro-fabricated springs and the seismic-mass can be controlled easily by a spin-coating process, the bandwidth and the response speed can be easily manipulated as desired. In other words, they can be easily controlled to meet requirements for most industrial applications.

CHAPTER 4: MECHANICS OF MATERIALS

4.1 Stress Analysis

Stress analysis of the device shows that the maximum Von-Mises stress occurs near the turning point of each spring segment. These stresses with the corresponding restoring force of the spring suspension system are depicted in Figure 4-1. For the 77.13 volts of pull-in voltage design, the maximum of Von-Mises stress was about 12.8 MPa which was about 9.14% of the yield strength of bulk nickel. These stress values could be further reduced by removing the stress concentration effect due to the sharp corners of the spring design through filleting.

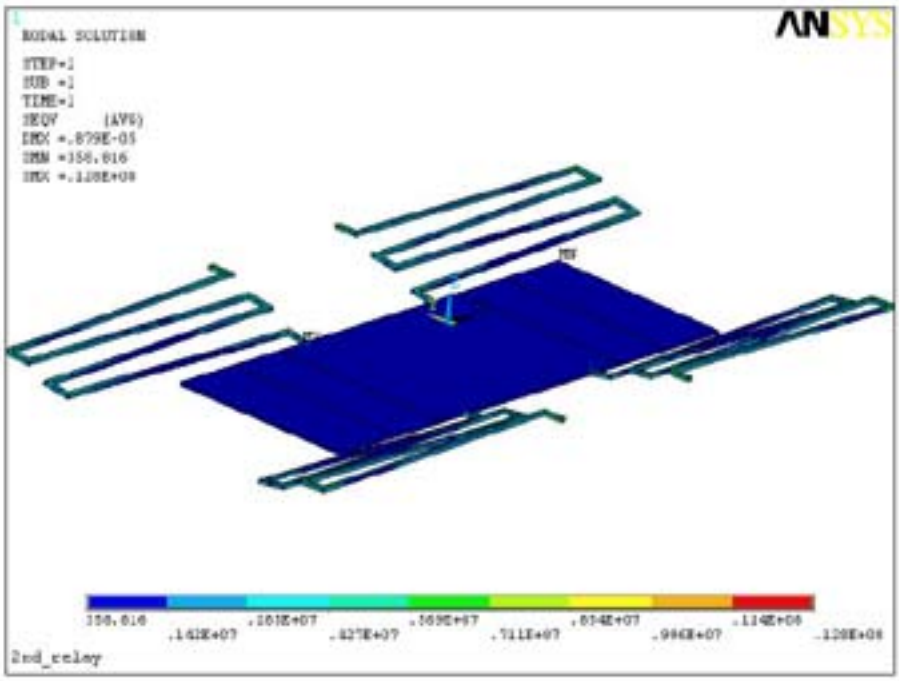

Figure 4-1 Von Mises stresses for the device: The force of 40 μN is applied. Other constant associated with the device are listed in Table 3-5

4.2 Contact Resistance

In general, the contact resistance decreases over the first few thousand switch cycles, and degrades progressively when the switches are cycled beyond approximately 10^6 cycles[81]. Most difficulties in the behavioral understanding of contact resistance come from the surface roughness. Mechanical contact is done by asperities of contact and the formed area is much smaller than the apparent one. Moreover all the asperities are not involved in the electrical contact. So we have Equation 4-1:

$$A_{electrical} < A_{mechanical} << A_{apparent} \tag{4-1}$$

The resistance of contact is due to the constriction of the current lines while passing through asperities. Several relations describe those phenomena[82,83]. If the radius a is much larger than the mean free path l_e, the resistance is dominated by a diffuse scattering mechanism, and the Maxwell spreading resistance formula for a single spot is used:

$$R_h = \frac{\rho}{2a} \tag{4-2}$$

where ρ is the resistivity, and a is the radius of a circular contact area. However, if the radius is small compared to the electron mean free path l_e, the resistance is dominated by the Sharvin mechanism, in which electrons are projected ballistically through the contact spot without being scattered. In this case, the Swartjes resistance for a single spot is used:

$$R_s = \frac{4\rho l_e}{3\pi a^2} \tag{4-3}$$

Wexler has given a solution of the Boltzmann equation, using the variational principle for resistance of a circular contact spot separating semi-infinite bodies. This results in a

simple interpolation formula which can account for the transition between the Maxwell and Sharvin regimes.

$$R_w = \frac{4\rho l_e}{3\pi a^2} + \nu \frac{l_e}{a} \frac{\rho}{2a} \tag{4-4}$$

where ν is a slowly varying function of the ratio *le/r* with ν(0)=1 and ν(∞)=0.694. The Table 4-1 reports mean free path values of basic contact materials.

Table 4-1 Conductivity and electron mean free path of main contact materials

Materials	ρ (10^{-8} Ωm)	l_e (nm)
Au	2.35	36
Cu	1.67	39
Ag	1.57	53

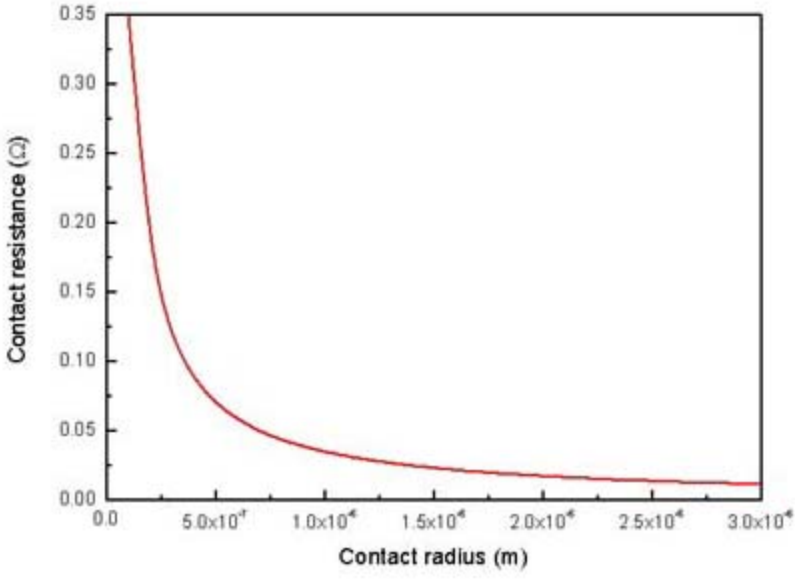

Figure 4-2 Calculated contact resistance versus contact radius: ρ_{Ni}=7.0×10^{-8} Ωm

In order to determine contact resistance, we need to know the accurate radius *a* of the circular area. However, it is not an easy job to get accurate surface profile at this moment. However, it is still instructive to study the characteristics of contact resistance on the basis of a simple surface profile model. Accordingly, we assumed that the radius *a* of circular area was on a range of μm contact. In this case, Maxwell spreading resistance formula can be used [Equation 4-2]. Figure 4-2 shows the contact resistance characteristics on a range of μm contact radius. The contact resistance becomes smaller on a range of large contact size. Therefore, the extra contact force is required to decrease the contact resistance. This is reason why the micro-relay needs to be operated in more than pull-in voltage.

4.3 Contact Force

In order to switch on the relay, the mechanical contact of switching electrode should be made by electrostatic force. The mechanical contact is determined by the contact deformation mode. From the material deformation theory, the following relation was reported[66].

$$F = n\pi \xi H a^2 \tag{4-5}$$

where n: number of asperities

H: material hardness

ξ: coefficient of material deformation mode

a: is the radius of a circular contact area

and with $\xi<0.3$: elastic deformation

$0.3<\xi<0.75$: elastoplastic deformation

ξ=1: plastic deformation

In electrical contact, ξ=0.6 is generally chosen. The Equation 4-5 permits to determine the minimum force that has to be applied to obtain the elastoplastic deformation mode. In this deformation mode, asperities are deformed to fragment and break the insulating layer. Figure 4-3 shows the minimum contact force for the elastoplastic deformation mode as function of the contact size with n=100, 200, and 300. All the contact forces for the elastoplastic deformation are identical at small contact size. In range of large contact size, however, the contact force has strong dependency on the number of asperities.

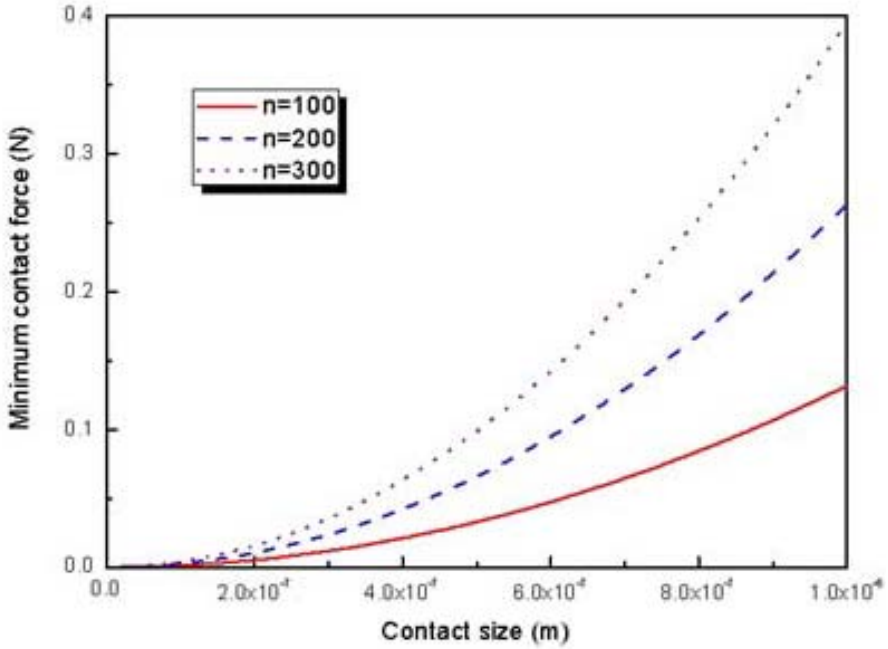

Figure 4-3 Minimum contact force for the elastoplastic mode as function of contact size

4.4 Stiction

For electrostatic force, restoring force is set by the design and it determines the power necessary to actuate the relay. Reducing the restoring force helps to lower the required pull-in power. However, free-standing microstructures are susceptible to

attachment to each other due to surface tension forces. Various analytical models for stiction and adhesion are available in literature[84,85,86]. However, no numerical solution or model exists that can explain or accurately predict stiction during fabrication or operation. Release of microstructures using supercritical CO_2 methods[87] or freeze-drying methods[88] relieves the surface tension forces during drying. In addition, the device operated in a vacuum has lower moisture content and is less susceptible to stiction. Thus, it is a trade-off between pull-in power and stiction risks.

In our system, there was no significant stiction problem because the air gap was quite large compared to other MEMS relays. However, if required, the third capacitive plate above the spring suspension can be used to avoid stiction. In addition, this extra electrostatic force attracts the top plate to its equilibrium position quickly and reduces the oscillatory motion.

4.5 Arcing

Arcing is an important wear factor in macro-relays because it happens several times per cycle due to contact rebounds. In micro-relays, Paschen curves show that contacts are so close that electrons present in air gap do not have enough room to accelerate and ionize air between contacts[89]. Therefore, closing arcs do not exist in micro-relays. However, opening arcs are still present. While separating contacts under load, electrons and ions tend to keep contact closed and metallic ions are emitted from anode to cathode. This phenomenon, called Townsend arc, is an important wear factor in micro-relays. To limit this phenomenon, polarization has to be inversed regularly or contact separated without electrical load.

4.6 Mechanical Wears

Fretting, creep, and corrosion are expected to have a limited role in relay failure mode because masses are so small that MEMS devices have low sensitivity to inertial phenomena, and moreover, they are hermetically sealed[83].

CHAPTER 5: MEMS TECHNOLOGY AND UV-LIGA

5.1 Introduction to MEMS Technology

Miniaturization of mechanical systems promises opportunities for progress of science and technology in new directions. Micro Electro Mechanical Systems (MEMS) have recently become an important area of technology. Micro-mechanical devices and systems are inherently smaller, lighter, faster, and possibly more precise than their macroscopic counterparts. Micro-fabrication provides a powerful tool for batch processing and miniaturization of mechanical systems into a dimensional domain not accessible by conventional techniques. Furthermore, micro-fabrication provides an opportunity for integration of mechanical systems with electronics.

MEMS were first developed at the end of 1980's and began to commercialize in the 1990's. MEMS technologies have been developing very fast, and have opened up many new opportunities to industrial, telecommunication, biomedical, and military applications. A typical MEMS device is a unit including both electronic and mechanical microstructures. The typical size of a micro-system is on the order of hundreds of microns. The MEMS fabrication technologies were developed on the foundation of the technologies developed by the microelectronics industry in the past decades. They may be used to create tiny electromechanical devices or systems.

Recent progress of the micro-fabrication technology is transforming the conventional field of mechanical transducers into MEMS transducers. Rapid advances in device design, fabrication, materials, testing, packaging, and applications, as well as the rapid expansion of the field has brought the outstanding results in the MEMS.

Because MEMS is an offshoot of the technology developed to fabricate integrated circuits on silicon, it includes techniques such as ion implantation, isotropic and anisotropic etching, anodic bonding, non-contact lithography, material deposition, electroplating, and X-ray radiation. Integrated circuits are designed to exploit the electrical properties of silicon, but MEMS utilizes both the mechanical and electrical properties of materials such as silicon, metal/alloys, or polymers. MEMS devices have advantages of miniaturization, reliability, long lifespan, and low drive power. The miniaturization of electromechanical systems has already had significant impacts on various areas, and the commercialization of MEMS has already spread to all corners of life. In recent years, many MEMS companies have started up, and developed many MEMS devices for telecommunication, biomedicine, military, and various other applications. In the following sections, the MEMS technologies related to this research work were briefly reviewed.

5.2 Fabrication Route of MEMS Devices

The MEMS fabrication technologies can be divided into three categories: surface micromachining, bulk micromachining, and molding.

5.2.1 Surface Micromachining

Surface micromachining process is additive: various films are deposited on top of the substrate, and then parts of deposited films are selectively removed to create MEMS devices, similar to fabrication of multi-layer integrated circuits. The typical surface micromachining process is graphically shown in Figure 5-1.

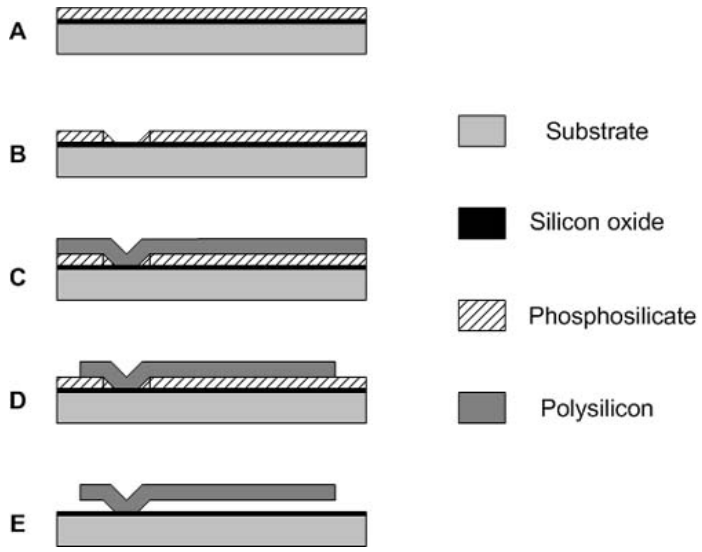

Figure 5-1 Typical surface micromachining process sequence: (A) Sacrificial layer deposition. (B) Base patterning with mask 1. (C) Microstructure layer deposition. (D) Pattern microstructure with mask 2. (E) Selective etching of sacrificial layer

Silicon surface micromachining is a powerful technique to fabricate micro-accelerometer chips for controlling automobile air-bag deployment and mirror arrays for portable projectors[90]. The major draw of surface micromachining is the limited vertical dimension of the microstructures[5] and the yield problems related to stiction of the substrate[83-87]. This restricts the ability to create devices, which can deliver significant mechanical forces or power levels, and to define channels or cavities for fluidic, chemical or biological applications.

5.2.2 Bulk Micromachining

Bulk micromachining[91] involves etching features directly into silicon wafers or other substrates. If the integrated electrical function is required, the micro-electronic elements are created using microelectronics processes on the top side of the silicon wafer, and then bulk micromachining commences from the other side of the wafer to yield mechanical

elements such as thin diaphragms or beams on the top side of the wafer. This strategy has been used for many years to create small pressure sensors[92]. The cavity is evacuated and sealed to create relative and absolute pressure sensors. Figure 5-2 shows a schematic diagram of a bulk micro-machined cavity and membrane structure for a pressure sensor. The low cost, high etching selectivity, and reliability are the advantages of the bulk micromachining. However, the major drawbacks are the poor lateral dimensional controls due to the anisotropic nature of etch, and dependence of crystal planes in orientation-dependent etching which results in the limit of device configurations.

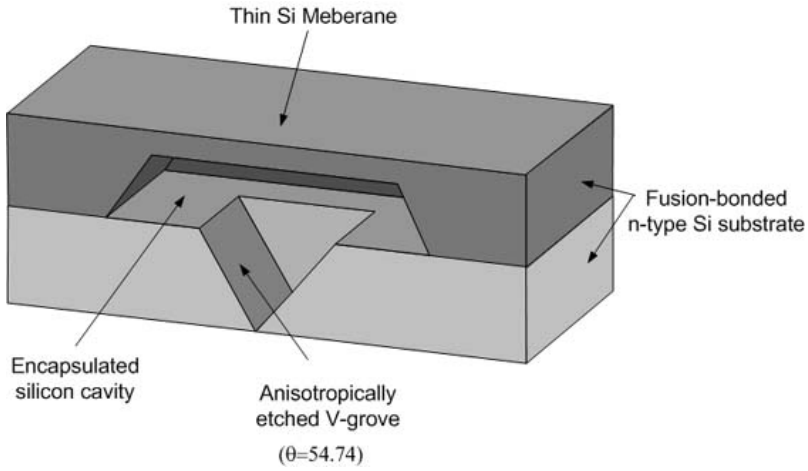

Figure 5-2 Schematic illustration of a typical bulk micro-machined structure

5.2.3 Molding

The third prevalent manufacturing process used for MEMS is the creation of the mechanical elements of the device by deposition of material into a micro-fabricated mold. The most widespread molding process is LIGA[93]. The basic process consists of creating a polymer mold by lithography and then electroplating metal into the mold cavities. A typical process flow is shown in Figure 5-3.

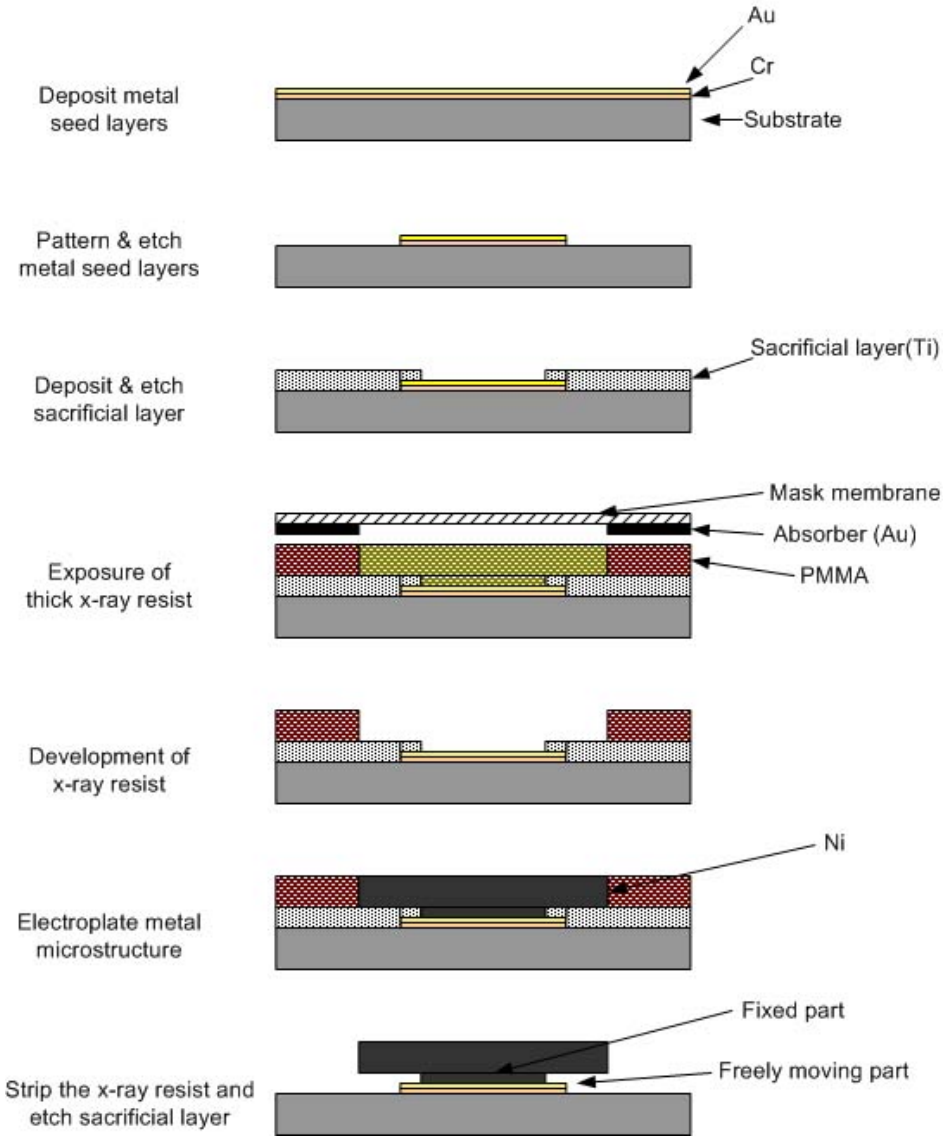

Figure 5-3 Typical process flow for a LIGA device

The idea of using a molding operation is not confined to electro-deposition. Other materials, such as polycrystalline silicon and silicon carbide, can be deposited using chemical vapor deposition, and refractory ceramics structures have been created by slurry processing methods[94]. The advantage of such molding processes is a broad selection of materials. They also have the same advantage of bulk micro-machined parts in terms of

the size of features. However, non-electronics compatible processes and materials restrict the capability of high degrees of integration.

In this study, molding technologies based on UV-LIGA process was used to fabricate the devices. The detail processes and characteristics of UV-LIGA are explained in the following section.

5.3 UV-LIGA Technology

5.3.1 Advantages of UV-LIGA Process

Compared to the more conventional MEMS processes based on silicon technology, the UV-LIGA processes have some unique advantages. First, it allows the fabrication of microstructures of any lateral shape with structural heights up to several hundreds of micrometers in any cross-sectional shape[46]. Second, a wide variety of materials such as plastics, metals, alloys, and ceramics or a combination of these materials can be used as the structural materials[94]. These advantages make it very suitable for fabricating micro power relays. For example, beryllium-copper can be used for making a micro-spring, high aspect ratio microstructures can be used to achieve stronger force with limited driving voltage, and good electrically conducting materials such as copper and gold can be electroplated as electrodes for better contacting condition. Finally, the fabrication cost of UV-LIGA is much lower than that of x-ray LIGA. The x-ray LIGA may be too costly for most industrial applications because its process requires expensive x-ray masks and x-ray beam lines. In UV-LIGA process, thick SU-8 resist and ultraviolet light source are used, instead of the x-ray. This approach helps to reduce the cost of fabrication

significantly, and at the same time boast the productivity. In addition, an x-ray exposure may last several hours and an exposure with UV-light source can be done within seconds.

The research presented in this dissertation focused on both the design of micro transducers (micro relay and accelerometer) based on the electrostatic actuation and a multi-layer, multi-step UV-LIGA process used to successfully fabricate a prototype of the micro transducers.

5.3.2 SU-8 Negative Photoresist for UV-LIGA

SU-8 is a negative, epoxy-type, near UV photoresist based on EPON SU-8 epoxy resin. This photo resist can be spin-coated to thicker than 2 mm, and aspect ratio more than 20 with a standard contact lithography equipment. Moreover, in X-ray lithography, the thickness of the resist can be up to 3-5 mm, and the achievable aspect ratio can be more than 60. These results are due to the low optical absorption in the UV range. For example, 100% absorption occurs for 2 mm thickness in the 365nm-wavelength. Of course, x-ray LIGA still yields better results at a higher processing cost. In addition SU-8 is well suited for acting as a mold for electroplating because of its relatively high thermal stability (T_g > 200 °C for the cross-linked resist). Therefore, UV-LIGA process by SU-8 is very suitable for low-cost application.

5.3.3 Basic SU-8 Processing Steps

SU-8 processes applied to this research work were performed in CAMD[*]. The procedures for SU-8 process were well understood and standardized by CAMD for several years. Therefore, most processes applied to this research were based on CAMD

[*] Center for Advanced Microstructures and Devices, Louisiana State University, Baton Rouge, LA 70806

work. However, some processing conditions were modified to improve the quality of devices, and summarized in the following sections.

5.3.3.1 Substrate Preparation

The process starts with a 4-inch diameter substrate such as silicon, silicon oxide, glass, or aluminum oxide substrates. To improve the adhesion of the SU-8 on the substrate, dehydration bake was performed at 200℃ for 1hr. For better adhesion with the substrate, adhesion promoter for SU-8, OmniCoat, was sometimes spun on the substrate, followed by SU-8 coating. The detail process information for OmniCoat is available from the MicroChem Inc.

5.3.3.2 Spin Coating

Spin coating was performed using the Headway Research PWM101 Light Duty Photoresist Spinner. The spin curves shown in APPENDIX C1 represent the thickness versus spin speed characteristics of four different MicroChem SU-8 formulations for 30 second spin time. For thick layers, an edge bead appears at the border of the wafer. In order to reduce it, all samples were put on a flat plane for 1 to 2 hours at room temperature after removing excessive resist from the edges of the substrate.

5.3.3.3 Pre-exposure Bake (Soft Bake)

This step was done on the temperature-controlled flat and horizontal hot plate. The substrate coated with SU-8 was placed on the hot plate for 10 min to reduce the internal stress, and then the hot plate was ramped from room temperature to 95°C, and held for specific period of time depending on the thickness of SU-8. All solvent in the SU-8 layer is removed in this step. For the best result, flatness of coated SU-8 is very important

because non-uniformity of the resist coats yields exposure non-uniformity in later processing. Table A-1 established by MicroChem illustrates soft bake times for different thickness layers.

5.3.3.4 Exposure

Exposure to UV light promotes cross-linking of the SU-8 photoresist. The exposure was performed using a Quintel UL7000-OBS Aligner with a 1000 W Hg lamp. The required dose depends on the thickness of SU-8. Table 3-1 attached in APPENDIX C3 shows the exposure-doses depending on the thickness of SU-8. Because light components with shorter wavelengths have much higher absorption rates than the longer wavelength ones, overexposure tends to happen at the surface of the resist due to the excessive absorption of shorter wavelength components. In addition to filtering of shorter wavelength components, the stepwise illumination was also performed for high exposure doses to avoid over-heating related errors. For example, the SU-8 was illuminated for 20 seconds, cooled down for 60 seconds, and illuminated again.

5.3.3.5 Post-exposure Bake (PEB)

During this step the illuminated SU-8 is polymerized through a cationic photo-amplification mechanism. The recommended PEB process by MicroChem is shown in APPENDIX C4. All samples were ramped from room temperature to 95°C. In order to minimize internal film stresses, an intermediate bake was performed at 60°C depending on the film thickness before allowing the wafers to cool to room temperature.

5.3.3.6 Development

The standard way using SU-8 Developer was performed at room temperature. The development time depends on the layer thickness. After the development, the substrate was rinsed with isopropyl alcohol. If white traces remain on the surfaces, it indicates that the development is not finished, and then the substrate has to be put in the developer again.

5.3.4 Nickel Electroplating

The next step of UV-LIGA is electrodeposition of metal. In this research, nickel and copper were electroplated on the patterned substrate, and the related technology was summarized in this section.

5.3.4.1 Mechanism of Electrodeposition

Electroplating bath was composed of anode, cathode, aqueous-metal solution, and a DC power supply [Figure 5-4]. Nickel pellets were used for the sacrificial anodes, and a thin layer of Au/Cr (plating seed layer) deposited by evaporation was used for the cathode. The aqueous-metal solution was made of nickel (Ni^{2+}), hydrogen (H^{+}), sulfate ions (SO_4^{2-}), and additives such as sodium lauryl sulfate($CH_3(CH_2)_{11}OSO_3Na$).

With an external electric field applied, positive ions are attracted to the negatively biased cathode. The nickel ions that reach the cathode receive free electrons and are converted to metallic nickel at the cathode surface forming the electrodeposits. Simultaneously, nickel anodes produce ions into the plating solution by the electrochemical etching process. Hydrogen ions that also gain electrons from the cathode form bubbles of hydrogen gas. The formation of hydrogen gas is undesirable since it

lowers the plating efficiency and the bubbles can obstruct the deposition of the intended electrodeposit[95].

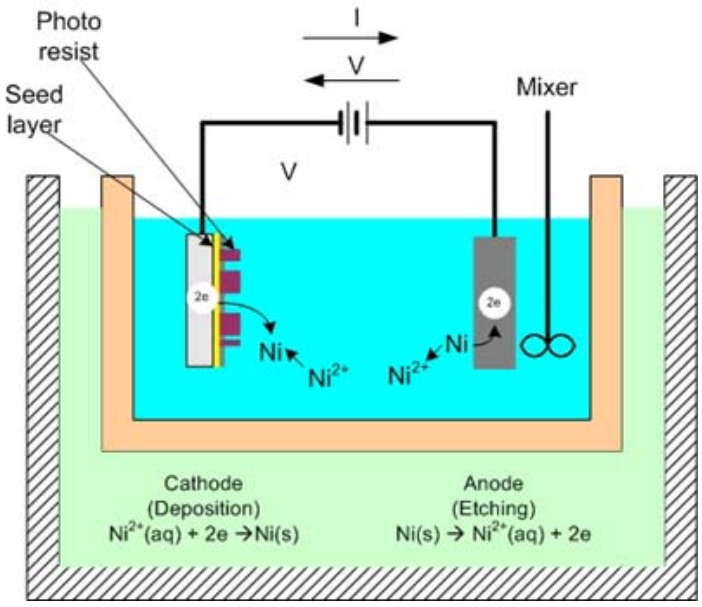

Figure 5-4 Electroplating setup

5.3.4.2 Electrodeposition Rate and Thickness

Theoretical calculation of electrodeposition rate and thickness could be performed using Faraday's law as follows.

$$\frac{1F}{96487C} = \frac{mol \times n_{el}}{I \cdot t} \tag{5-1}$$

$$w = \frac{MW}{F \cdot n_{el}} I \cdot t = 1.095 \cdot I[A] \cdot t[hr] = \frac{I[mA] \cdot t[\min]}{54800.36} \tag{5-2}$$

where w is the amount of nickel deposited at the cathode or dissolved at the anode in grams, MW(58.69g/mol) is the molecular weight of Ni, n_{el} is the number of electrons involved in the reaction, I is the current that flows through the plating tank, and t is the

time that the current flows. This calculation assumes that all of the current is effectively used in the deposition or dissolution of nickel. In practice, secondary electrochemical reactions may occur such as the reduction of hydrogen, which consume a small percentage of the current. Therefore, the modified equation is

$$w[g] = \frac{I[mA] \cdot t[\min] \cdot \eta}{54800.36} \tag{5-3}$$

where η is plating efficiency.

The deposit thickness can be evaluated by considering the volume of the deposit in Equation 5-2. Since the volume of the deposit (V) is the product of the plated surface area (A) and the thickness (h), the weight of the deposit (w) can be expressed as follows.

$$w = \rho_{Ni} \cdot A \cdot h \tag{5-4}$$

where δ_{Ni}=8.9g/cm^3 is the density of nickel, A is the area being electroplated, and h is the deposit thickness. By Equation 5-2, 5-3, and 5-4, the deposit thickness can be determined as follows.

$$h[\mu m] = 12.294 \cdot J[A/dm^2] \cdot t[hr] \cdot \eta = \frac{J[mA/cm^2] \cdot t[\min] \cdot \eta}{48.772} \tag{5-5}$$

where J is the current density. Figure 5-5 and Table 5-1 show the characteristics of nickel deposit based on 95.5% cathode efficiency.

5.3.4.3 Distribution of Deposition Thickness

In general, the deposit thickness will not be perfectly uniform across the plated area. It is therefore important to understand the factors that influence the deposit thickness

distribution. These factors are the current distribution and the throwing power of the plating solution. The current density at any point affects the local thickness at that point.

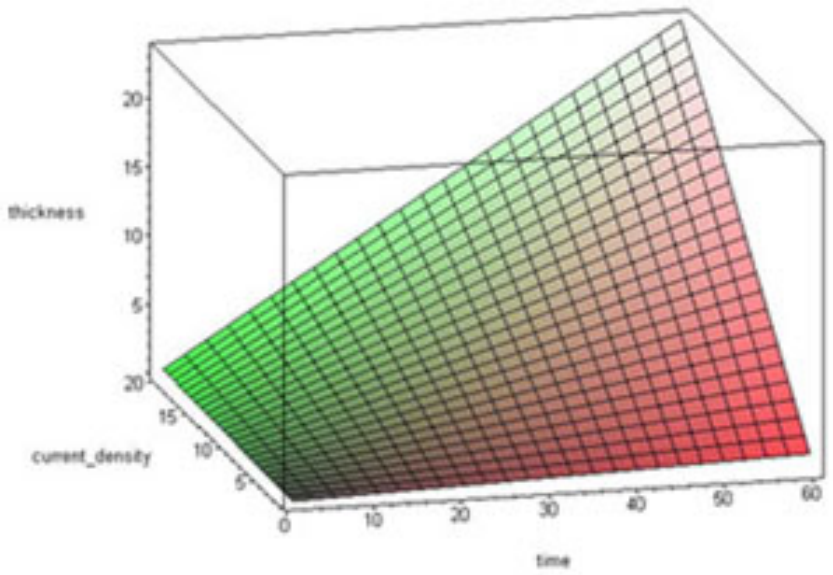

Figure 5-5 The relationship of nickel deposition thickness [μm], current density [mA/cm^2], and time [min]*

Table 5-1 Time to electroplate nickel at various current densities*

Current Density (mA/cm2)	Time (min) to deposit the indicated thickness of nickel at various current densities							
	5 μm	10 μm	15 μm	20 μm	25 μm	30 μm	40 μm	50 μm
10	25.5	51.1	76.6	102.1	127.7	153.2	204.3	255.4
15	17.0	34.0	51.1	68.1	85.1	102.1	136.2	170.2
20	12.8	25.5	38.3	51.1	63.8	76.6	102.1	127.7
25	10.2	20.4	30.6	40.9	51.1	61.3	81.7	102.1
30	8.5	17.0	25.5	34.0	42.6	51.1	68.1	85.1
40	6.4	12.8	19.2	25.5	31.9	38.3	51.1	63.8
50	5.1	10.2	15.3	20.4	25.5	30.6	40.9	51.1

* Based on 95.5% cathode efficiency

The current distribution is largely determined by geometric factors such as the shape of the part, the location of the part relative to the anodes, and the placement of parts on the plating racks. The current density is higher on prominences and areas closest to the anodes due to the lower resistance to current flow with the shorter anode-to-cathode distance. This variation in current density necessarily means that prominences receive a thicker coating than recessed areas. Since the localized electrodeposition rate is proportional to the localized current density, a uniform current density over the entire seed layer is needed to obtain uniform thickness. To achieve selective deposition, however, portions of the seed layer are covered with masking material that makes the current density in its proximity non-uniform. An example of the effect the plating mask has on the uniformity of current density is illustrated in Figure 5-6. In order improve the uniformity of current density, shields was sometimes used.

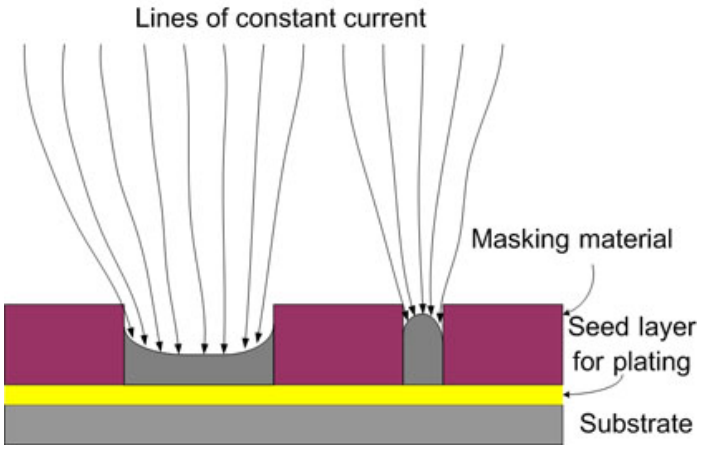

Figure 5-6 Non-uniform current density by masking material

The other factor is the throwing power of the plating solution. Metal distribution is influenced by cathode polarization, the cathode efficiency-current density relationship, and the electrical conductivity of the solution[96]. Throwing power can be determined

experimentally. A solution with high-throwing power is capable of depositing almost equal thicknesses on both recessed and prominent areas. Research on the throwing power was not the focusing point of this research and not performed in this dissertation. In general, however, the current distribution was primarily determined by geometric factors. In addition the throwing power was somewhat improved by lowering the current density, increasing the electrical conductivity of the solution, increasing the anode-to-cathode distance, and raising the pH and temperature.

5.3.4.4 Internal Stress

During electrodeposition, stresses can develop within the deposit due to the effect of the electrocrystallization process or the codeposition of impurities such as hydrogen, sulfur, and other elements[97]. Stress becomes an important consideration when thick coatings are produced. Generally, Watts nickel solutions without additives exhibit tensile stress in the range 125 to 185 MPa, under typical operation conditions. Lower stress levels can be achieved with sulfamate nickel solution[98].

5.3.4.5 Nickel Plating Solutions

Generally, nickel sulfate solution (Watts solution) and nickel sulfamate solution are used for nickel plating [Table 5-2]. Sulfate solution is chiefly used for decorative plating, and nickel sulfamate solution is used for electroplating in engineering applications because of its low residual stress, high deposition rates, and good ductility despite its high cost compared to nickel sulfate solution. It is important to carefully maintain the solutions and continuously treat for impurities. In this study, sulfamate solution was used to

fabricate micro-structures and its detail formulation was shown in APPENDIX D. The properties of this solution were summarized in the following section[98].

Table 5-2 Typical composition and operating conditions for nickel plating solutions

	Nickel Sulfate Solution	Nickel Sulfamate Solution
$NiSO_4 \cdot 6H_2O$ (Nickel Sulfate)	240-300 g/L	
$Ni(SO_3NH_2)_2$ (Nickel Sulfamate)		300-450 g/L
$NiCl_2 \cdot 6H_2O$ (Nickel Chloride)	30-90 g/L	0-30 g/L
$B(OH)_3$ (Boric Acid)	30-45 g/L	30-45 g/L
$CH_3(CH_2)_{11}OSO_3Na$ (Sodium Lauryl Sulfate)	1 g/L	1 g/L
Temperature	40-60 ℃	40-60 ℃
Agitation rate	200 rpm	200 rpm
pH	3.5-4.5	3.5-4.5
Current density	20-70 mA/cm^2	20-150 mA/cm^2
Deposition rate	25-85 μm/hr	25-85 μm/hr

The nickel sulfamate is the primary source of nickel ions (Ni^{2+}). A potential problem of this solution is hydrolysis of nickel sulfamate which produces sulfate and ammonium ions. These greatly increase the tensile stress of the deposit. To avoid hydrolysis of the nickel sulfamate it is important to maintain the temperature below 65℃ and the pH above 3.0. One of the advantages of sulfamate solutions is the higher solubility of nickel sulfamate compared with nickel sulfate. It is therefore possible to use higher nickel concentrations, permitting higher plating rates.

Nickel chloride has a pronounced effect on stress and also influences anode behavior. For example, chlorides promote anode corrosion, but also increase conductivity thereby reducing voltage requirements, throwing power, and uniformity of coating thickness

distribution. However, chlorides increase the internal stress of the deposits, and they tend to refine grain size and minimize formation of nodules and trees. Therefore, the chloride content should be kept low to achieve minimum stress. It is possible to operate with zero chloride if sulfur activated nickel anodes are used with sufficient anode area. However, a low concentration of nickel chloride is generally recommended to provide some insurance of satisfactory anode performance.

Boric acid is a buffer and has the major function of controlling the pH of the solution. Because the cathode efficiency (90-97%) is generally lower than the anode efficiency (almost 100%), the nickel ion concentration and the pH of the solution will slowly rise during operation. Regular additions of sulfuric acid (H_2SO_4) are therefore required to adjust the pH. The mechanism by the boric acid operation is complex, but it is generally understood that it exists in solution as a mixture of borate ions and non-ionized boric acid. When hydrogen is discharged, some boric acid will ionize to replace the lost hydrogen ions and so the pH change is limited. At the same time, borate ions form. When acid is added to adjust the pH, these borate ions combine with hydrogen ions to reform boric acid. Boric acid is therefore only lost through drag-out or other solution losses. Deposits may be cracked and burnt at low boric acid concentrations. Its concentration should vary with operating temperature from 30g/L at 20℃ to over 45g/L at 52℃[99]. Low boric acid can cause orange peel type of pitting. High boric acid will tend to salt-out of solution at lower temperatures. Once salted out or crystallized, it is difficult to redissolve[100] .

Surfactant (sodium lauryl sulfate) was added to lower the surface tension of the plating solution so that air and hydrogen bubbles did not cling to the parts being plated. It also has an indirect effect on corrosion performance[101].

5.3.4.6 Process Quality Control

Process quality control involves maintaining the concentrations of the main constituents within specified limits, and controlling current density, temperature, pH, agitation and the purity of plating solutions. The general operation conditions are listed in Table 5-2. The specific operation conditions applied for this research work were shown in APPENDIX D. For the best result, the following operation conditions were carefully controlled.

- **Maintaining the Optimum Solution Concentration**

Analysis of nickel, chloride, and boric acid were carried out using titration methods. Any change in the concentration of these major constituents was generally very slow and therefore they needed only to be checked infrequently. The detail titration methods of nickel and boric acid applied to this research work were shown in APPENDIX E[102].

- **Current Density**

Current density management is important for two main reasons. Firstly, the current density controls the rate of deposition. Secondly, the current density must be controlled within the correct operation range in order to obtain sound deposits having uniform appearance and free from burning. All samples for Ni deposition were electroplated with 20-50 mA/cm^2. The uniformity of thickness became worse when the current density more than 100 mA/cm^2 was applied. Uniformity of thickness could be improved with low current. With current density less than 10, however, the color of deposited nickel became dark. In addition it took too long to deposit the required thickness.

Within normal operating limits (20-150 mA/cm^2), it has been reported that current density and temperature has little effect on the hardness and the structure of the deposits[98].

On the other hand, current density has varying effects on stress. It may fluctuate from compressive to tensile, and the properties and characteristics of the deposit are also affected by current density. Increasing current density causes a minor increase in tensile stress in chloride free bath. Ductility decreases rapidly with increasing temperature.

- **Temperature**

Temperature can influence the brightness range, throwing power, ductility, hardness, internal stress, and burning characteristics. Stress has a pronounced minimum at 50℃ with value of about 13.8 MPa in tensile, increasing uniformly above and below 50℃[99]. For the best result, therefore, temperature was kept in the water bath at 56℃.

- **pH**

The pH of the nickel plating solutions has an important influence on bath performance[103]. The pH can affect the bright plating range, cathode efficiency, effects of impurities, throwing power, stress as well as the physical properties of the deposit. A sulfamate solution with 76.5 g/L of nickel yields its lowest stress at pH 3.8 to 4.8, and with 107 g/L does at pH 2.9 to 3.8. The stress increases rapidly at pH values above 5.0 because of the codeposition of basic nickel salts. Hardness in the sulfamate solution is affected by pH. As pH rises, it is fairly constant up to a critical value of about 5.0, above which it rises sharply, but does not change the deposit hardness. Above pH 5.0, hardness increases and ductility decreases through codeposition of small amounts of basic nickel salts. Therefore, the constant pH range from 3.9 to 4.1 was kept for this work. Under normal operating conditions the pH tended to rise and this was counteracted by the addition of dilute sulfuric acid.

- **Agitation**

The plating solution was stirred at 200 rpm. Agitation is important to dislodge hydrogen or air bubbles from the cathode surface, which might otherwise cause pitting. Agitation also assists in maintaining a uniform temperature throughout the solution.

- **Filtration**

Continuous filtration was performed to maintain the plating solutions free of insoluble particles. These might be introduced through solid particle adhering to the work, drag-in, additions of impure chemicals, corrosion of dropped components, airborne particles, faulty anode bags, etc. Clearly, it is important to eliminate as many of the sources of insoluble particles as possible.

- **Anodes for nickel plating**

Activated grade of nickel pellets was used for anode, which contained a small amount of sulfur (e.g., 0.02%) to lower the anodic potential. However, it was reported that the resultant insoluble black residue of nickel sulfide might pose a problem as a possible source of roughness[98]. Therefore, we used the titanium anode basket and the polypropylene bags. Titanium baskets are widely used for anode baskets as it conducts the electrical current to the nickel metal without acting as an anode itself. This is due to a protective oxide film formed on the titanium surface during electrolysis.

Nickel anodes and baskets must be fitted with bags to prevent nickel fines or nickel sulfide residues entering the plating solution. Polypropylene is widely used for anode bags because of its durability. However, other fabrics including cotton and other synthetics are used successfully.

CHAPTER 6: MICRO-FABRICATION OF TRANSDUCERS

6.1 Micro-power Relay

The top (armature) and bottom part of a relay were fabricated separately and then assembled together. As shown in the schematic diagram in Figure 2-2, it can be seen that the bottom part of the relay is designed with three different heights. The bottom capacitor plate of the actuator and other connection pads are the lowest structures, the supporting posts for the suspension springs are the highest, with the two pair of electrodes of the relay higher than the bottom electrode of the capacitive actuator and lower than the supporting posts of the suspension springs. This structural design of multiple heights requires a multi-step and multi-layer fabrication process. In this structure, electrical energy is stored in the top and bottom capacitor. The initial air gap, typically 10-30 μm, is controlled by adjusting the height of each layer in the bottom part.

The fabrication process starts with a 4 inch diameter substrate such as silicon or alumina wafer which is deposited with a thin layer of metal for the electroplating seed layer. To obtain good adhesion, a thin layer of chromium (100Å) was evaporated first, followed by another thin layer of gold or copper (500Å). The lithography process was performed using SU-8 (negative type) or SPR photoresist depending on processes. The different types of SU-8 and SPR were used according to the desired thickness. In the SU-8 process, for example, SU-8 50 from MicroChem Corporation was used to spin-coat the first layer with 150 μm thickness at 1000 rpm for 30 seconds. SU-8 5 gives 10 μm thickness at 1500rpm for 30 seconds for the second layer. And SU-8 10 gives 25μm thickness at 1250 rpm for 30 seconds for the third layer. In the SPR process, SPR 220-7

from Shipley Company was used to spin-coat the first layer with 36 μm thickness at 1500 rpm for 30 seconds followed by another 1000 rpm spin-coat for 30 seconds. The single coat of SPR 220-7 at 2000 rpm for 30 seconds gives the 9.5 μm thickness of the second layer. The detail SU8 processes are described in the previous chapter 5.3.3, while the SPR processes in APPENDIX F. The 30 mA/cm^2 of electric current density was applied in the nickel sulfamate solution to deposit nickel microstructures together with 200 rpm stirring, and the temperature was maintained with 56℃ in the water bath. The detail plating process was described in the chapter 5.3.4. The fabrication steps for both the top and bottom parts of the relay are presented separately in the following sections with schematic diagrams.

6.1.1 Fabrication of the Bottom Part Relay

Three different fabrication processes were used to find the best suitable fabrication technology. The first type is based on a hybrid UV-LIGA process using both the negative resist SU-8 and the positive resist SPR. SU-8 was used when thick structures are desired while SPR was used when thin metal structures are required.

6.1.1.1 Hybrid UV-LIGA Process

The fabrication flowchart of the hybrid UV-LIGA process is schematically shown in Figure 6-1.

Step #1: Pattern the electroplating seed layer for the supporting pads, the switching electrodes, and the bottom plate for the parallel plate capacitor before 1st layer structure was electroplated;

Step #2: Fabricate the supporting pads, the switching electrodes, and the bottom plate for the parallel plate capacitor on the patterned seed layer. This was achieved by the lithographically patterned SU-8, electroplating Ni to the desired thickness, and polishing the sample to obtain a flat surface. The SU-8 mold for the 1st layer did not need to be removed and was kept for insulation purpose;

Step #3: Fabricate the two pair of the metal electrodes and the two armature supporting posts that also supply signal to the top capacitive plate of the actuator. The sample was etched slightly in the 20% HNO_3 solution for a couple of minutes before electroplating the second layer structures to improve the strength of adhesion between the 1st and 2nd layers. The structures were again slightly over-plated and then polished to obtain the required height [5 μm in Figure 6-1 (c)] and the flat surface. The 2nd layer of SU-8 serves not only as the plating mold but also the insulation layer between the top and bottom part of capacitive plate to protect the assembled relay from being burned-out;

Step #4: Raise the height of supporting posts for the "armature" of the relay by a desired height (10 μm in the prototype relay presented here). A thin layer of SPR photoresist was lithographically patterned to make the plating mold for the supporting posts, followed by nickel electroplating and polishing processes to make the smooth surface [10 μm in Figure 6-1 (d)]. This polishing step was also used to control the air gap between the top and bottom plate of the capacitor. This height difference can be adjusted based on the spring stiffness and driving voltage;

Step #5: Carry out the flood-exposure process to remove the remaining SPR. The exposed SPR is removed using the MF84 MX developer from Shipley Company.

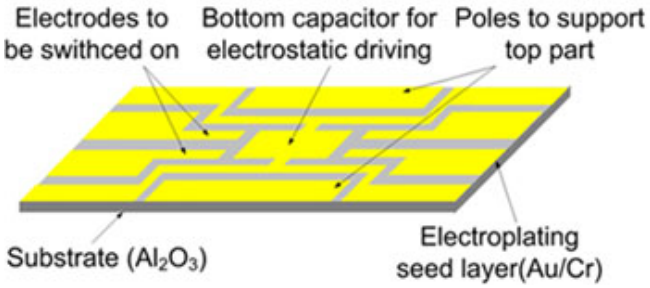

a) Step #1

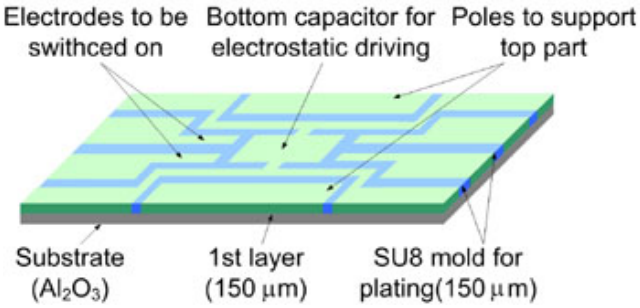

b) Step #2

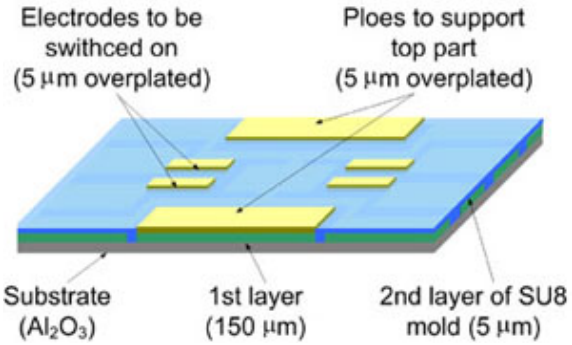

c) Step #3

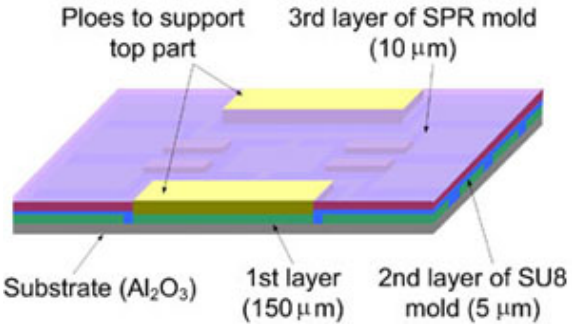

d) Step #4

Figure 6-1 Schematic diagrams of the hybrid UV-LIGA process for fabrication of the bottom part of the relay

Figure 6-1 continued

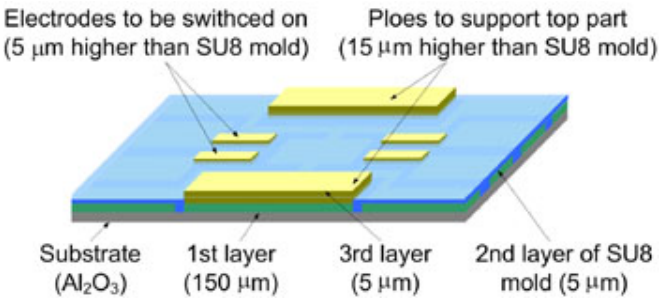

e) Step #5

6.1.1.2 SU-8 Process

This method was based on the SU-8 process only. The first three steps are exactly same as those of the hybrid UV-LIGA process. In the following steps, SU-8 was used to spin-coat the 3rd layer with 10 μm thickness at 1500 rpm for 30 seconds. The SU-8 mold for each electroplating was removed at the final step by using Dynasolver 185 from Microposit Company. However, it was very difficult to completely remove the SU-8 mold with Dynasolver in spite of heating it up to 85℃. Alternatively the SU-8 mold was removed by using the Technics Micro-RIE85 and the Tepla 300 microwave plasma asher*. Because a direct use of the Tepla plasma asher might causes cracks from high temperature in the chamber, half thickness of the SU-8 mold (80 μm) was removed by using Technics Micro-RIE85 which was equipped with a water-cooling system, and then followed by Tepla plasma asher. The 20-25% of CF_4 was supplied to etch the SU-8 mold with the 300-350 Watts of power in the 760 mTorr vacuum chamber.

* Dry etch process was performed at UTD with the help of Dr. Daniel Park who worked with Dr. Michael C. Muphy as a post doctor at LSU.

The dry etching process by plasma resulted in complete removal of the SU-8 mold and much better geometric shape.

6.1.1.3 SPR Process

The fabrication flowchart of the SPR process is schematically shown in Figure 6-2. This method was also three-mask process completely based on UV lithography of SPR. SPR 220-7 was spin-coated for a thickness of 36μm in the 1st layer structures [Figure 6-2 (a)]. This was achieved using the two-steps of spin-coating process with the first one at 1500 rpm for 30 seconds followed by another 1000 rpm spin-coat for 30 seconds. The single layer coat of SPR 220-7 at 2000 rpm for 30 seconds gave the 10 μm thickness for the 2nd and 3rd layer [Figure 6-2 (b) and (c)]. After the SPR mold was completely removed with acetone solution, the insulation layer was spin-coated with SC1827 photoresist from Shipley Company. The single layer coat of SC1827 at 3000 rpm for 30 seconds gave the 2.5 μm thickness [Figure 6-2 (d)]. The detail process procedures of SPR and SC1827 were shown in APPENDIX F and G.

Figure 6-3 shows two photographs of the bottom part of the prototype relay fabricated using the hybrid UV-LIGA process schematically shown in Figure 6-1. The SU-8 plating mold was kept, and all of the metal structures were imbedded in the cured SU-8 polymer (mold). Figure 6-4 shows photographs of the bottom part of the relay fabricated using the SU-8 based process. Because the cured SU-8 is stripped after an electroplating process, the height of the metal structures looks much higher than those in Figure 6-3. Figure 6-5 shows the photographs of the bottom part relay made using the SPR based process. The maximum thickness of the structures was much smaller in comparison with the other two processes.

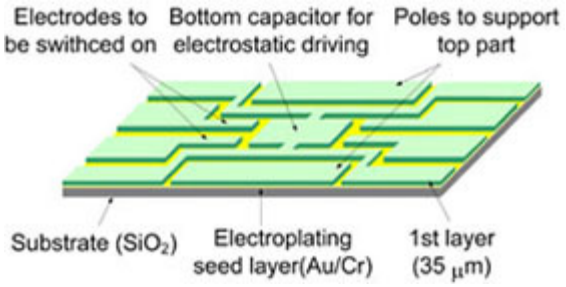

a) Step #1

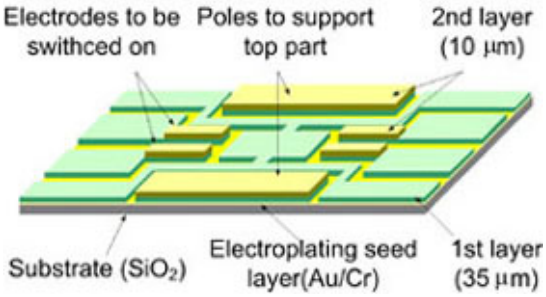

b) Step #2

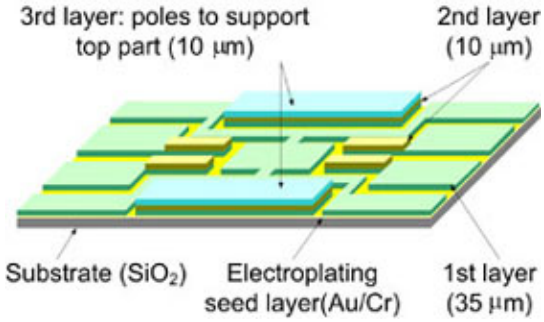

c) Step #3

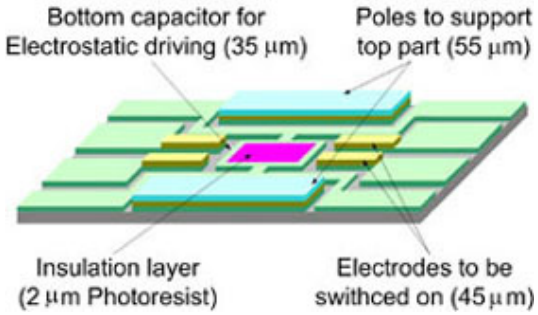

d) Step #4

Figure 6-2 Schematic diagrams of the SPR process for fabrication of the bottom part of the relay

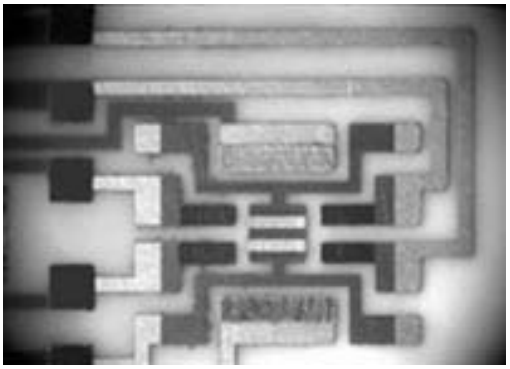

a) Top view

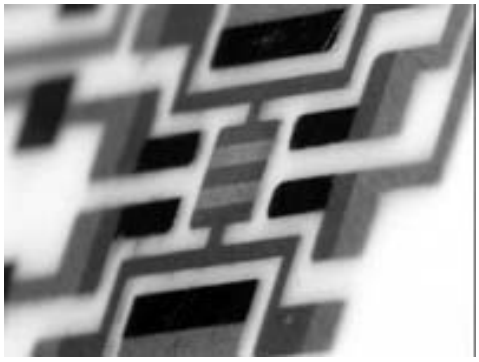

b) Side view

Figure 6-3 Photographs of the bottom part of relay by the hybrid UV-LIGA process. The thicknesses of 1st, 2nd, and 3rd are 150, 10, and 10 μm. The surface area of capacitor is 2000×2000 μm. The first layer of nickel micro-structures is embedded in the SU8 mold

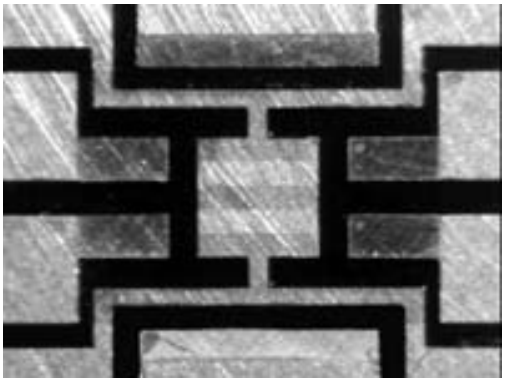

a) Top view

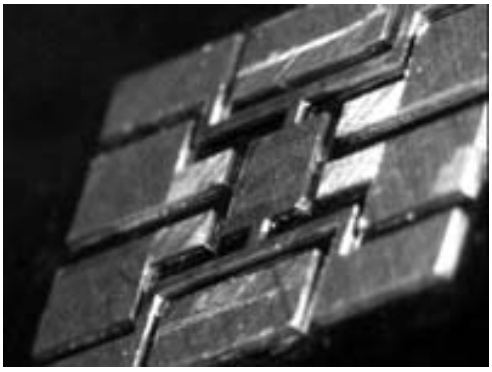

b) Side view

Figure 6-4 Photographs of the bottom part of relay by the SU-8 process only. The thicknesses of 1st, 2nd, and 3rd are 100, 15, and 20 μm. The surface area of capacitor is 2000×2000 μm

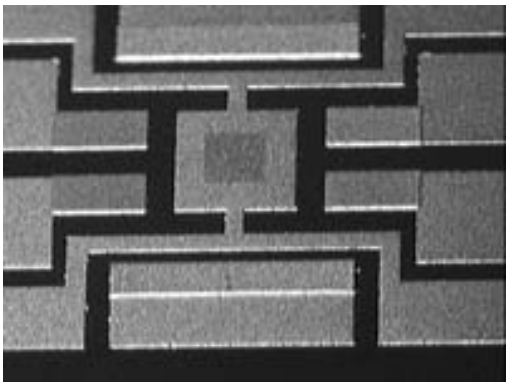

a) Top view

b) Side view

Figure 6-5 Photographs of the bottom part of relay by the SPR process only. The thicknesses of 1st, 2nd, and 3rd are 35, 10, and 15 μm. The surface area of capacitor is 2000×2000 μm. The SPR mold for plating is completely removed by acetone solution

As can be seen from the figures, the supporting posts for the suspension springs are slightly higher than the electrodes of the relay which are to be switched on. The bottom plate of the capacitive actuator has the lowest height. The electrodes, the supporting posts, and the bottom plate of the capacitor are electrically isolated. The strips in Figure 6-3 and Figure 6-4 and the light-dark square in Figure 6-5 on the bottom capacitor are a thin layer of SPR or SU8 (2~5 μm) kept for electrical insulation purpose. When the armature is pulled down to switch on the relay during operation, possible deflection of the relay armature may happen, therefore resulting in physical contact between the top and bottom plates of the capacitive actuator. This insulation layer is necessary for preventing being burned-out between the top and bottom capacitive plate.

The advantage of the SU-8 based process in comparison with the SPR based one is the better processibility of making a thick metal structures (up to a couple of thousand micrometers), a key advantage for obtaining larger current capacity for the relay. Other advantages of the SU-8 based process are better step coverage and better sidewall quality compared with the ones obtained using the SPR based process. Figure 6-6 shows photographs of process characteristics. Structures fabricated by the SU-8 process show a stiff side wall, while structures by SPR process show poor step coverage.

The main disadvantage, however, is difficulty to strip the cured SU-8. This is a common problem for the SU-8 based LIGA process because it is well known that SU-8 is very difficult to strip. This is also the main reason that the hybrid UV-LIGA fabrication process is the preferred one because it successfully avoids the removal step of the cured SU-8 and keeps it for electrical insulation by using SPR in the last step. The hybrid UV-LIGA process takes advantages of both SU-8 and SPR. First of all, better thickness

control is achieved because the SU-8 is used for the thick microstructures while the SPR is used for the thin microstructures. The good controllability of thickness and flatness in the multilayer process is the most valuable property because the gap between the top and bottom capacitor affects the overall system response and functions. Another advantage is that the SU-8 plating mold does not need to be removed. Instead of removing the SU-8 mold, it was used as the body of the micro relay. In addition, with the help of a sacrificial layer, the hybrid UV-LIGA process could be applied to the integrated process by using an additional sacrificial layer, which was the topic of chapter 6.1.2. The whole microstructures of the relay were fabricated on the one substrate without assembling requirement. Table 6-1 shows the summarized characteristics of these fabrication processes.

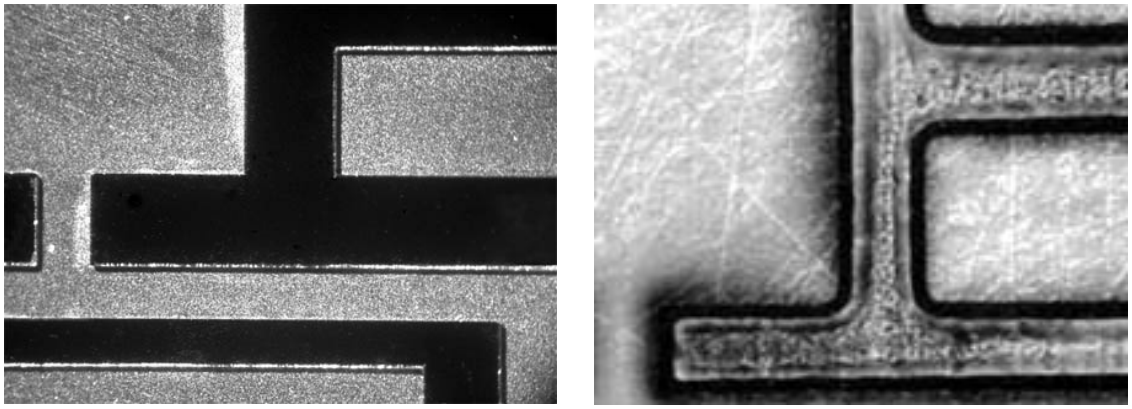

a) Stiff side wall by SU-8 process b) Poor step coverage by SPR process

Figure 6-6 Photographs of process characteristics

Table 6-1 Summarized characteristics of fabrication processes

Fabrication method	Side-wall stiffness	Step coverage	Thickness controllability	Multiple structurability	Process time	Process stability
Hybrid UV-LIGA	Good	N/A	Good	Good	Medium	Good
SU8	Good	Moderate	Moderate	Moderate	Long	Poor
SPR	Poor	Poor	Moderate	Poor	Short	Moderate

6.1.2 Fabrication of the Top Part Relay

The top part of relay includes suspension springs, the imbedded polymer connectors, the switching connector, and the top capacitor plate. The fabrication of the top part of the relay is much more technically involved than that of the bottom part of the relay. The fabrication flowchart is schematically demonstrated in Figure 6-7.

Step #1: Fabrication of the metal structures that include suspension springs, the frames, and the top electrode of the capacitor. Two consecutive electroplating processes were performed. First, a copper sacrificial layer was electroplated. A lithography patterning and electroplating of nickel were then followed to make the armature frame, the top electrode of the capacitive actuator, and the switching connectors;

Step #2: Fabrication of the two strips of polymer connectors (SU-8). Different thickness of SU-8 was spin-coated depending on the desired mass that affected system properties;

Step #3: Release the completed "armature" from the substrate by selectively etching the copper sacrificial layer. A commercial copper etch solution, APS Copper Etchant 100 from Transene Company, was used to selectively etches a copper at 14.4-28.8 μm/hr rate in 30-40℃.

Figure 6-8 shows a photograph of the armature after the resist was stripped and the polymer connectors were not patterned yet.

Figure 6-9 shows two pictures of the armature of the relay after the polymer connectors have been patterned. In Figure 6-9 (b), it was clearly shown that the switching connector and the capacitive plate were physically disconnected with the gap of 100 μm.

It was also sufficient gap to isolate them electrically. At this stage, the top part of the relay has been completed but not released from the substrate yet.

Figure 6-10 shows oblique views of the armature of the relay. In both pictures, thickness of polymer connectors (150 μm) is same while the amount of mass is different by 0.353 μg because they are covered with the different amount of SU-8.

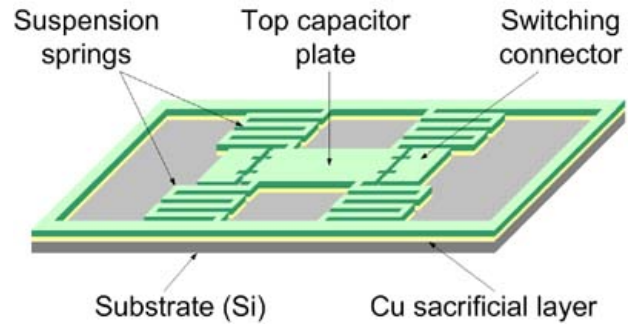

a) Step #1

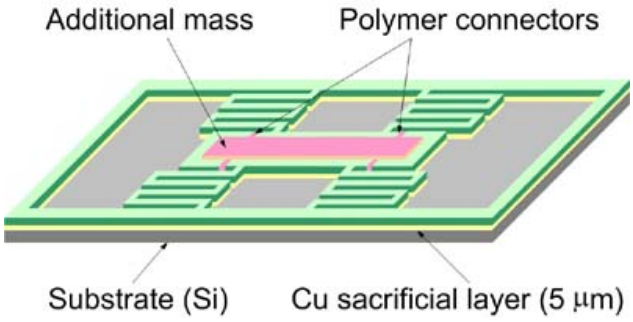

b) Step #2

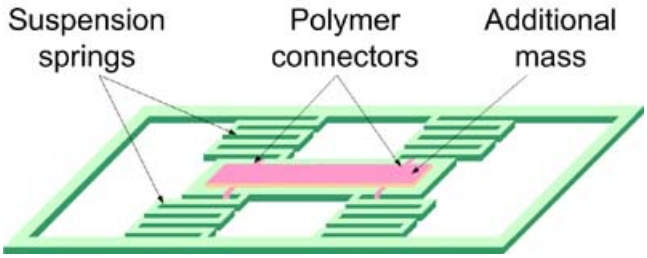

c) Step #3

Figure 6-7 Schematic diagrams of lift-off process using a Cu sacrificial layer

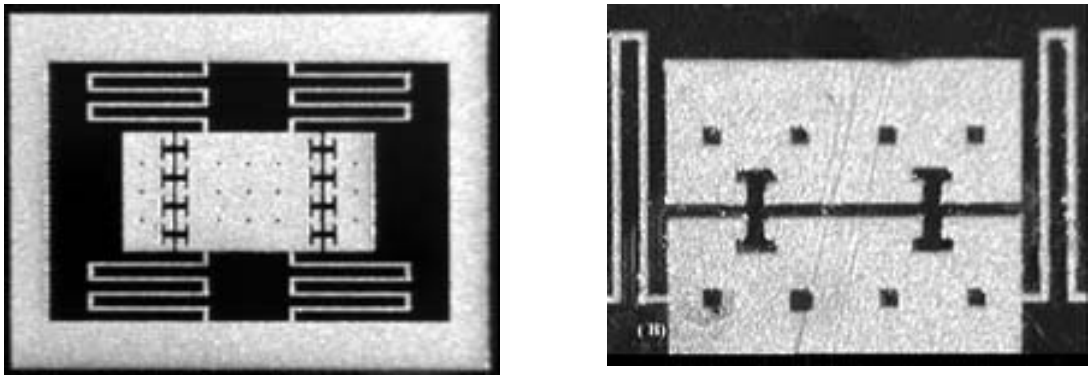

a) Top view b) Closed-up view

Figure 6-8 Photographs of the armature in the relay after the SU-8 plating pattern was stripped

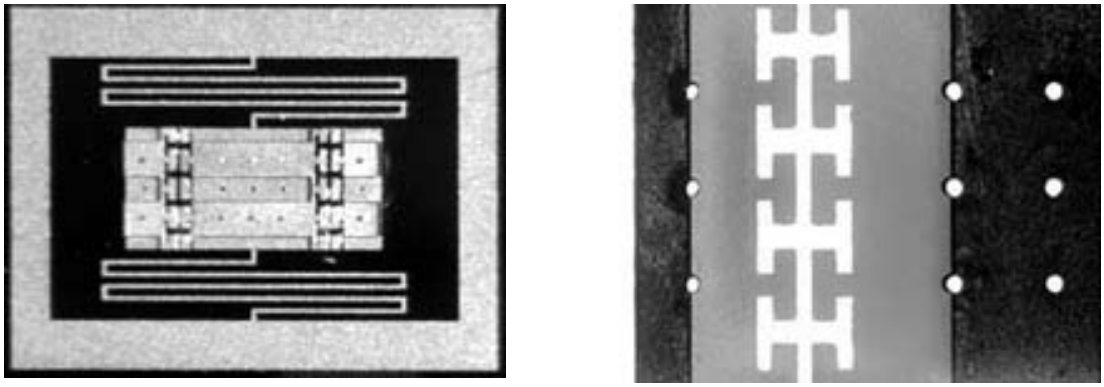

a) Top view b) Closed-up view

Figure 6-9 Photographs of the armature of the relay after the polymer connectors have been patterned: switching connectors and capacitive plate were separated with the gap of 100 μm for electrical isolation

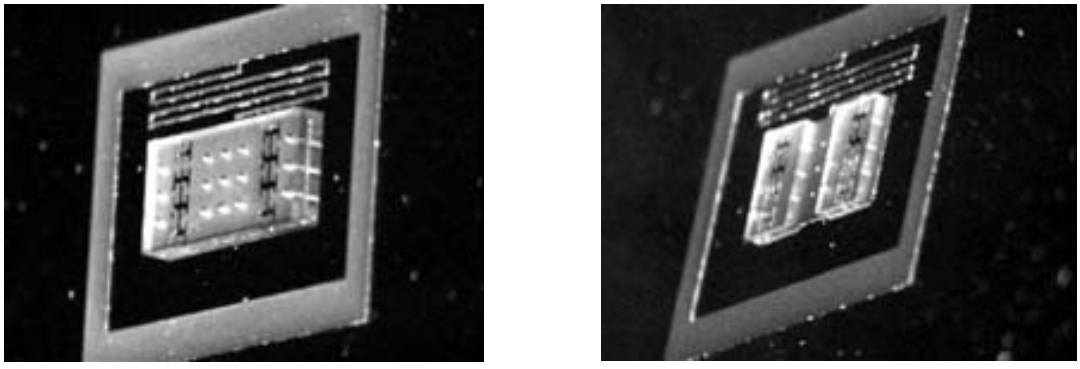

a) Photograph of fully covered SU-8 connector and plate b) Photograph of partially covered SU-8 connector and plate

Figure 6-10 Oblique views of the armature of the relay: The thickness of the polymer is 150 μm

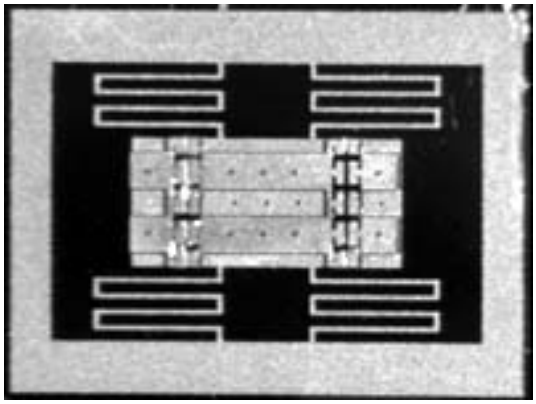

a) Photograph of four symmetrical springs with two stripes of a cured SU-8 for physical reinforcement and imbedded polymer connectors

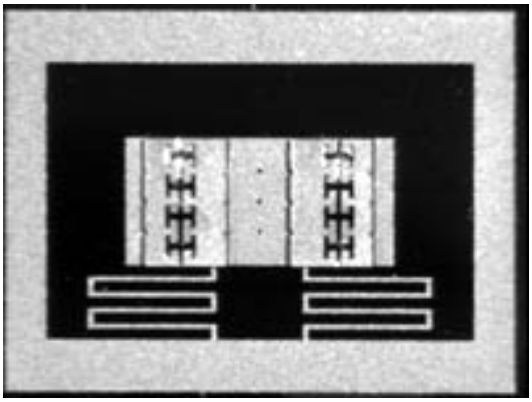

b) Photograph of two cantilever type of springs with a cured SU-8 polymer connectors

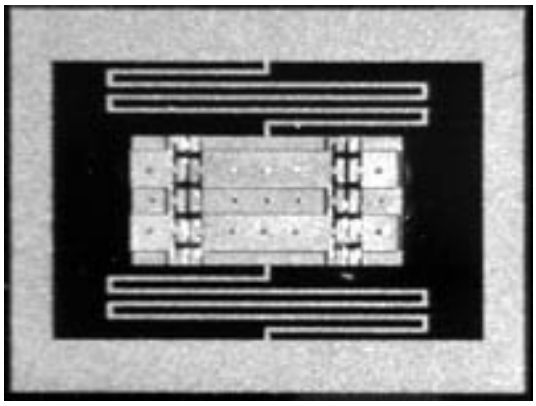

c) Photograph of two symmetrical springs with two stripes of a cured SU-8

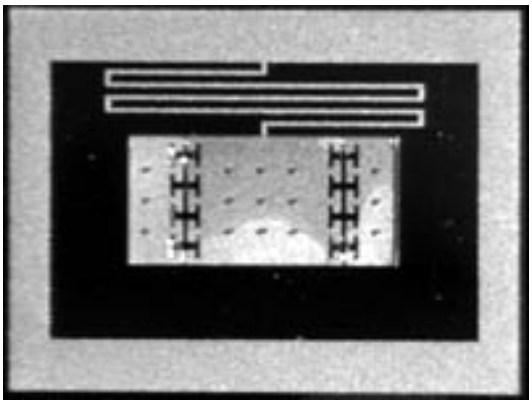

d) Photograph of cantilever type of spring with a fully covered cured SU-8 polymer connectors

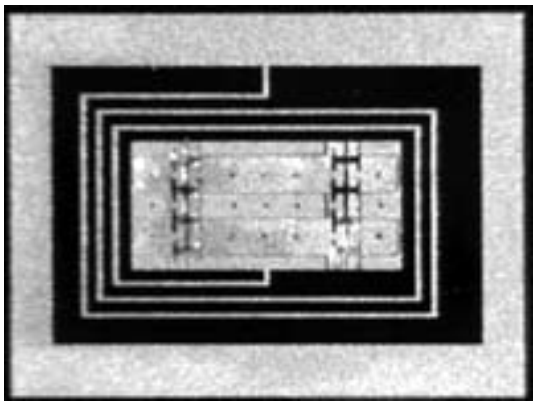

e) Photograph of spiral type of spring with two stripes of a cured SU-8

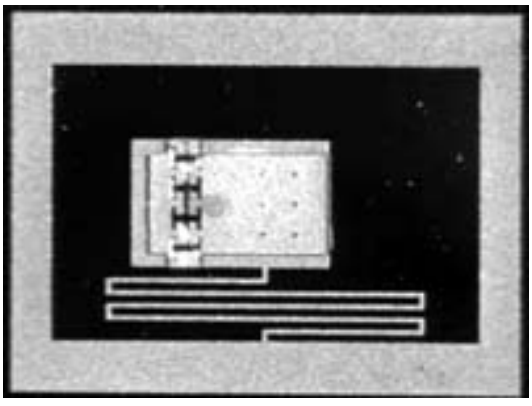

f) Photograph of cantilever type of spring with one switching connector

Figure 6-11 The several different types of design in the top part of relay. Each spring has different flexibility (spring constant) and additional polymer (mass)

Figure 6-11 shows pictures of the released top part of the prototype relay. The several different types of armature were designed depending on the required system properties where each spring had different flexibility (spring constant) and additional mass (SU-8).

6.1.3 Assemble the Top and the Bottom Parts

After the top and bottom parts of the relays were fabricated separately, they were bonded together using the "44" Rosin Core Solder from Kester Connecting Innovation and the Silver Paste Plus^{TM} from SPI Supplies Inc. There was an inherent alignment error to assemble the top and bottom parts without the help of alignment equipments. However, the minor alignment errors in the assembling did not affect the overall characteristics of the assembled relay. Figure 6-12 shows a photograph of assembled micro-relay. From the assembled relay, it can be seen that other than the two strips of cured SU-8 polymer resist, the assembled relay has a predominantly metal structure. Theses vertical structures of actuators can be also used as z-axis acceleration sensors by detecting the capacitance change when an external acceleration is applied to the movable top capacitor.

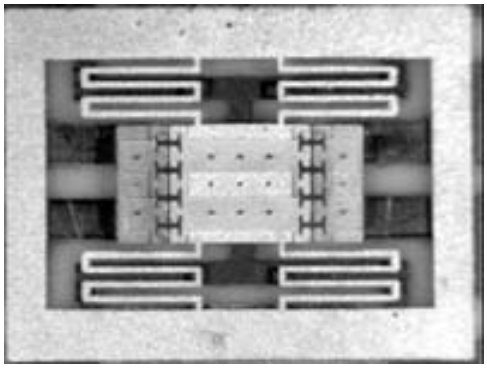

a) Wiring with solder and silver glue

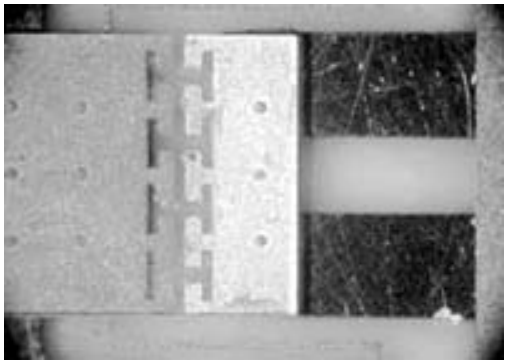

b) Closed-in picture of the switching connector and electrodes

Figure 6-12 Picture of an assembled relay

6.2 Micro-accelerometer

It was our approach to fabricate the proposed micro-relay by two different schemes; 1) the separated SU-8 process and 2) the integrated SU-8 process. In the first approach, the separated process, the top and bottom parts of the accelerometer were made separately and then assembled together. In the second approach, the integrated process, vertical structures were fabricated using a single substrate. The advantage of the integrated process was not to require the bonding of two structures. Therefore, the air gap between top and bottom part could be more precisely controlled. In addition, the integrated process was robust to alignment errors originated from no bonding step. In both processes, the structural design of multiple heights required a multi-step and multi-layer fabrication process. Instead of applying SU-8 only as a photo resist, the cured SU-8 was used as the primary structural material. Glass, ceramic, or silicon substrate may be used. The advantage of using glass as a substrate includes good adhesion and better spin-coat properties. The major advantage in using a silicon substrate is that signal-processing circuit may be fabricated on the same chip to provide an integrated system. The detail fabrication steps are presented in the following sections with schematic diagrams.

6.2.1 Separated SU-8 process

The first method is to fabricate the top and bottom parts of the accelerometer, and then assemble them together. The fabrication flowchart of the accelerometer is shown in Figure 6-13. The steps from 1 to 3 show the fabrication procedures of the bottom part. The top part is fabricated on the other substrate, and then assembled together (steps 4 to 8).

Step #1: Pattern a thin layer metal (Au/Cr) for the bottom part of the parallel capacitive plate;

Step #2: Fabricate the supporting posts and insulation layer. This is achieved by lithographically patterning SU-8 to the desired thickness. The air gap of fabricated accelerometer is controlled at this step;

Step #3: Spin-coat a thin layer of polymer (SC1827 or SU-8 2);

Step #4: Spin-coat SU-8 on another substrate and exposure it with the desired doses. Instead of developing the exposured structures, they had been kept until the next step;

Step #5: Spin-coat another layer of SU-8 and exposure it with the desired doses;

Step #6: Remove the unexposured SU-8 structures;

Step #7: Deposit a thin layer of metal (Au/Cr) by an evaporator for the top capacitive plate;

Step #8: Bonding the top and bottom structures together to form the accelerometer.

Figure 6-14 shows a photograph of the bottom and top part of the accelerometer. As can be seen from Figure 6-14 (a), the supporting posts for the suspension springs were slightly higher than the bottom capacitive plate which was covered with a thin layer of SU-8 (~2 μm) for electrical insulation purpose.

The alternative process is also tried to release the top structures from the substrate using back-side etch with chemicals such as HNA or Alkali-OH. Isotropic echants commonly used in microelectronics technology was applied to selectively remove the

silicon substrate: HNA system-mixtures of nitric acid (HNO_3), hydrofluoric acid (HF), and acetic acid (CH_3COOH).

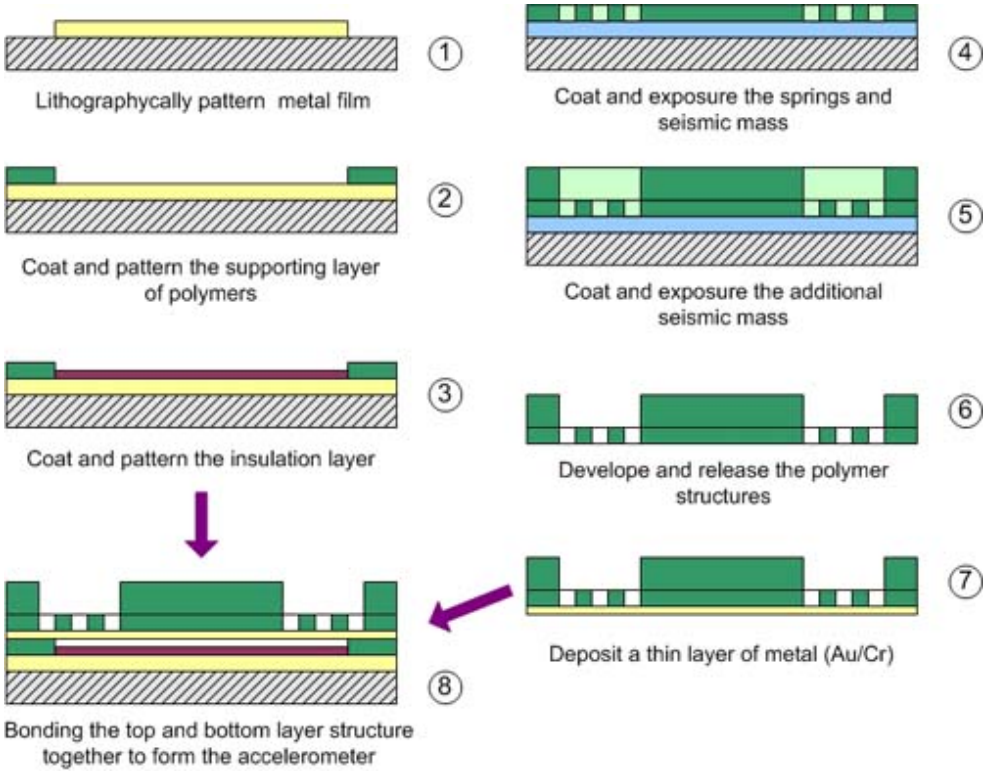

Figure 6-13 The fabrication flow chart for the polymer based micro-accelerometer by the separated process

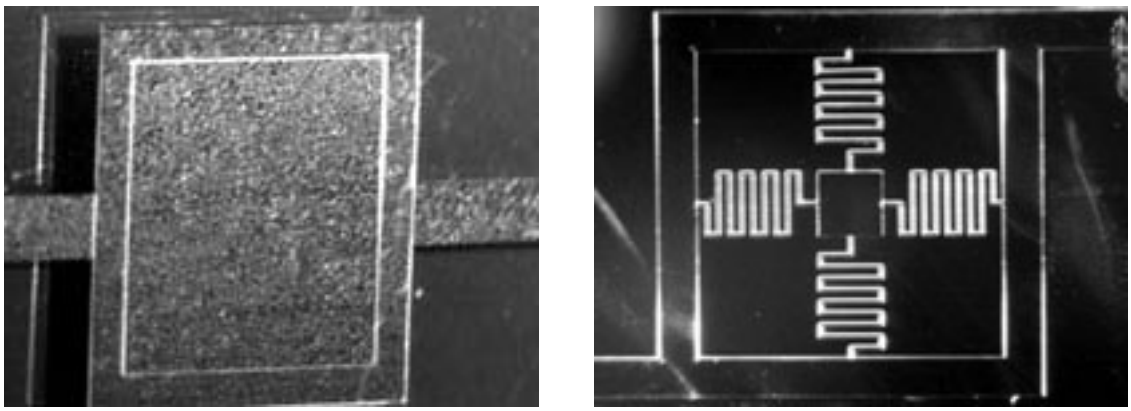

a) Bottom part b) Top part

Figure 6-14 Photographs of the prototype accelerometer

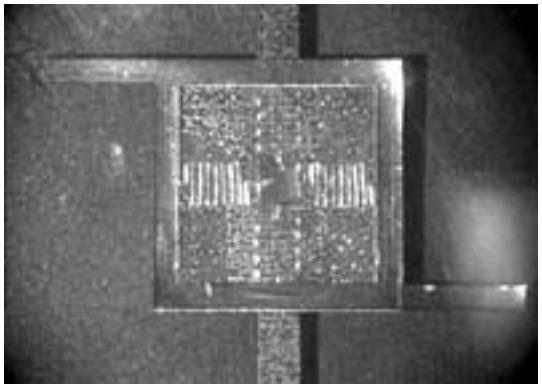

Figure 6-15 Photograph of the assembled accelerometer. The thickness of springs and seismic mass is 50 and 200 μm respectively. The air-gap is 20 μm

The reaction is initiated by HNO_3 that forms a layer of silicon dioxide on the silicon, and the HF dissolves the oxide away. The overall reaction is:

$$Si + HNO_3 + 6HF \rightarrow H_2SiF_6 + HNO_2 + H_2 + H_2O\,. \qquad (6\text{-}1)$$

Acetic acid is used to dilute the etchant. The compositions of mixtures can be varied to yield different etch rates. Figure 6-16 shows the isoetch-curves of various constituents by weight[104]. At high HF and low HNO_3 concentrations (region 1), the etch rate is controlled by the HNO_3 concentration because there is an excess of HF to dissolve the SiO_2 created during the reaction. On the other hand at low HF and high HNO_3 concentration, the etch rate is limited by the ability of the HF to remove the SiO_2 as it is created. In the region 3, initially the etch rate is not very sensitive to the amount of CH_3COOH, and then sharply falls for 1:1 ratio of HF: HNO_3. In our application, HNA mixture in region3 was used to accelerate etch rate.

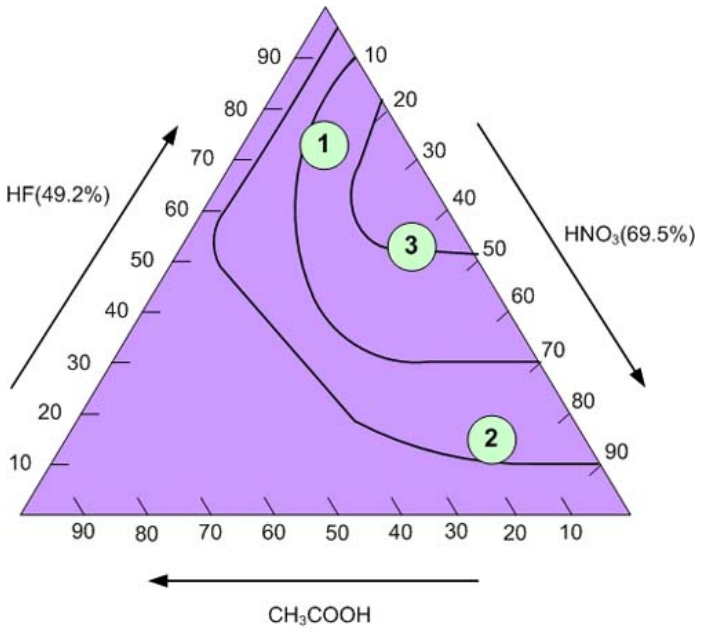

Figure 6-16 Isoetch curves for silicon in HNA system

6.2.2 Integrated SU-8 Process

The second method is an integrated process. The general idea is to deposit the springs-mass-frame layer by layer first using a light-shield metal film, and then develop and etch to obtain the desired pattern. This approach does not require an assembling step with the top and bottom capacitor. This means that the air gap between the capacitive plates is much more controllable. The fabrication flow chart is shown in Figure 6-17.

Step#1: Pattern a thin layer of metal (Au/Cr) for the bottom part of capacitive plate.

Step#2: Coat a thin layer of SU-8 (2 μm) for electrical insulation purpose.

Step#3: Coat and exposure the supporting posts. The exposured SU-8 structures are not developed at this stage. Instead they have been kept until the final step.

Step#4: Deposit another thin layer of Cr for the electrodes of the capacitor sensors and signal leads. This metal layer also serves as the protection material for the further

exposure of UV. Since Cr has almost 100 % absorption rate against UV, this metal layer prevents the fabricated SU-8 in the previous steps from the further exposure of UV.

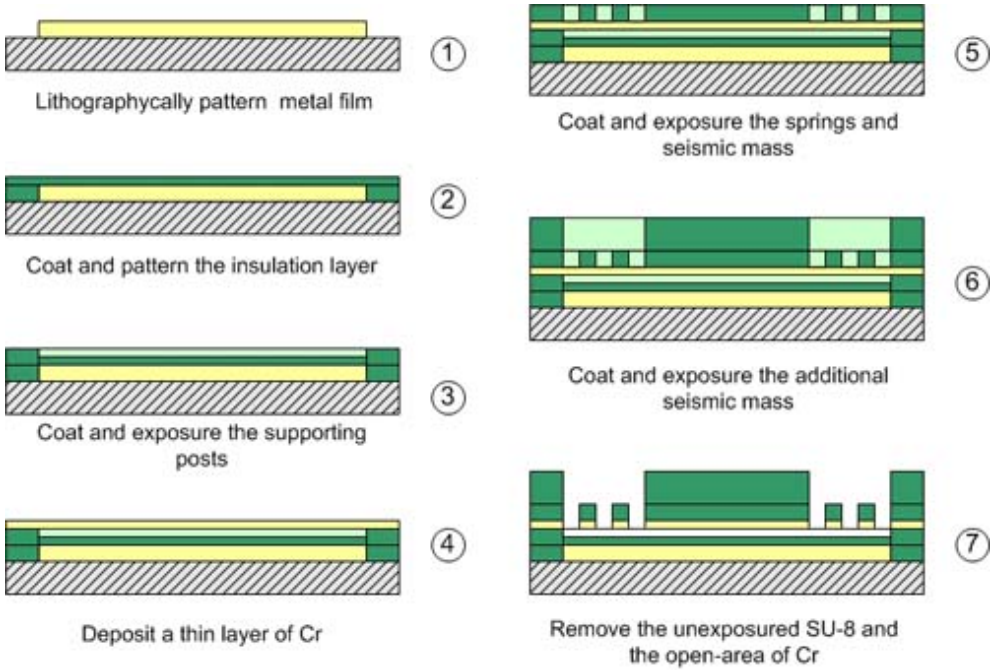

Figure 6-17 The fabrication flow chart for the polymer based micro-accelerometer by the integrated process

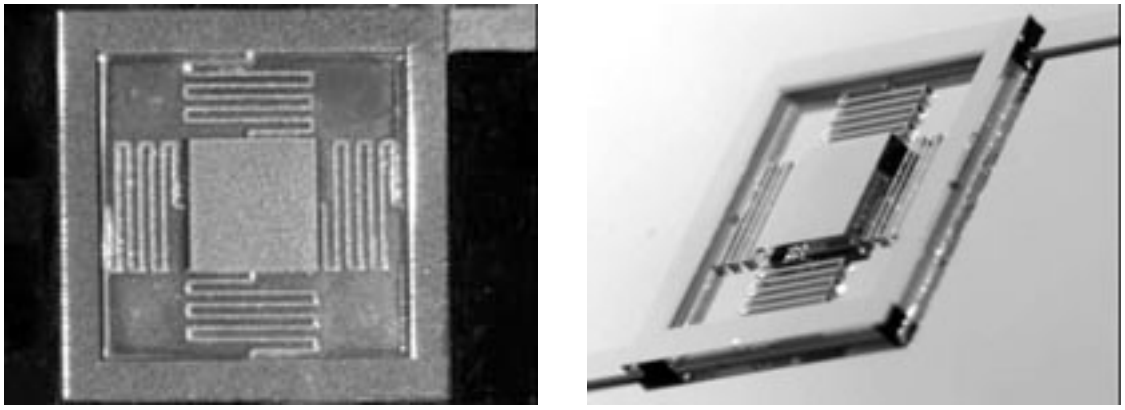

a) Top view b) side view

Figure 6-18 Photographs of the prototype accelerometer fabricated by the integrated process. The thickness of springs and seismic mass is 50 and 200 μm respectively. The air-gap is 25 μm

Step#5: Coat and exposure the springs and seismic mass.

Step#6: Coat and exposure the additional seismic mass to get the desired value of inertia.

Step#7: Finally develop the unexposed SU-8 and etch the open-area of metal (Cr).

Figure 6-18 shows photographs of the fabricated accelerometer.

CHAPTER 7: EXPERIMENTS AND RESULTS

7.1 Test Setup

Testing of the micro-devices was carried out using a probe station equipped with a microscope, power supply, signal generator, oscilloscopes, multimeter, and computer with data acquisition board [Figure 7-1].

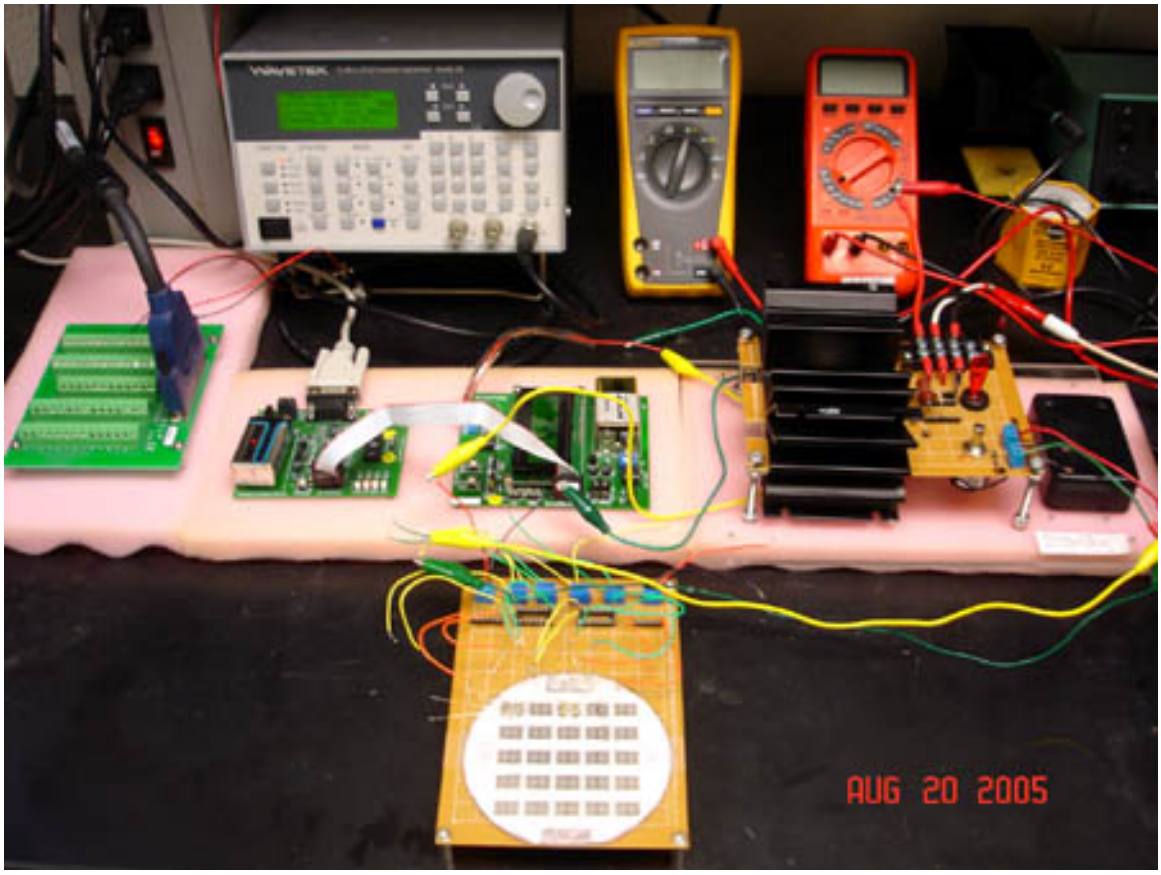

Figure 7-1 Probe station to test the device

The voltage-controlled voltage source (VCVS) using APEX PA84 high operational amplifier was designed to supply DC control voltage to the prototype relay. The PA84 is a high voltage operational amplifier designed for output voltage swings up to ± 145 V

with a dual supply or 290 V with a single supply. Figure 7-2 shows the schematic diagram of inverting Op Amp with non-inverting positive reference to produce VCVS from 0 to 290V. The ideal transfer equation is given as Equation 7-1.

$$V_{out} = -V_{in}\frac{R_f}{R_g} + V_{ref}\left(\frac{R_f + R_g}{R_g}\right) \tag{7-1}$$

Feedback resistance (R_f) was fixed at 4 KΩ while rheostat was used for gain resistance (R_g) to adjust the desired output voltage (V_{out}).

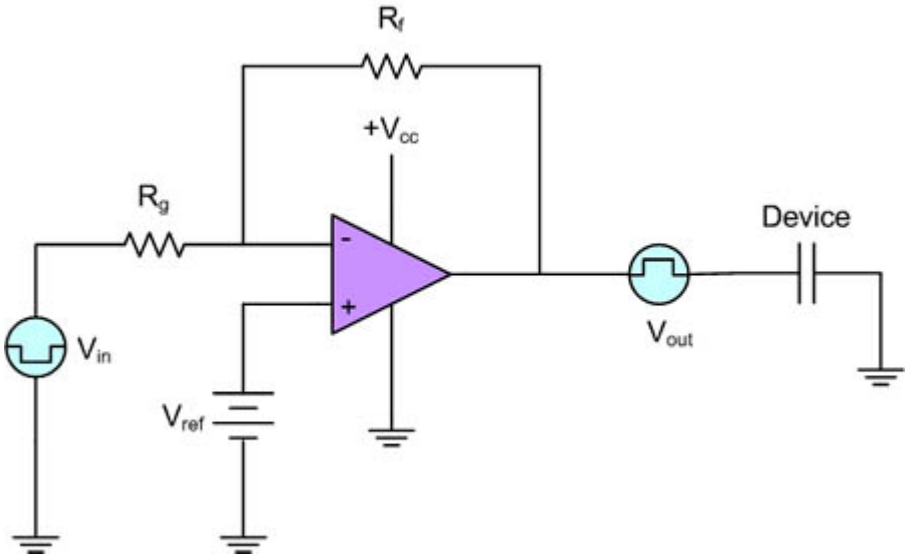

Figure 7-2 VCVS using inverting Op Amp with non-inverting positive reference

For the input signal, the function generator from WaveTek Company was used, and the data acquisition board from Quantum Research Group was used to measure the capacitance change during operation. A square wave of input signal ranging from 0.5 to 500 kHz was applied to the device to measure the dynamic response of the device.

7.2 Micro-power Relay

In order to test the assembled relay, electrical leads were glued to the outer contacts of the relay base using a silver paste and a solder. The specifications of the relay are listed in Table 7-1. The relay operated consistently for more than 10^6 cycles with actuation voltages of approximately 18 V as shown in Figure 7-3. The capacitance abruptly increased at the operation voltage due to the movement of armature. Compared to other MEMS relays (normally more than 50 V) with approximately the same size, this actuation voltage was considerably low due to the large area of capacitive plates and the relatively small spring stiffness. It also shows that the device exhibits hysteresis during its voltage operation. This is well known property of MEMS electrostatic device. The contact resistance of a closed micro-relay ranged from 0.3 to 11.5 Ω and the current capacity was more than 5.0 A without any degradation.

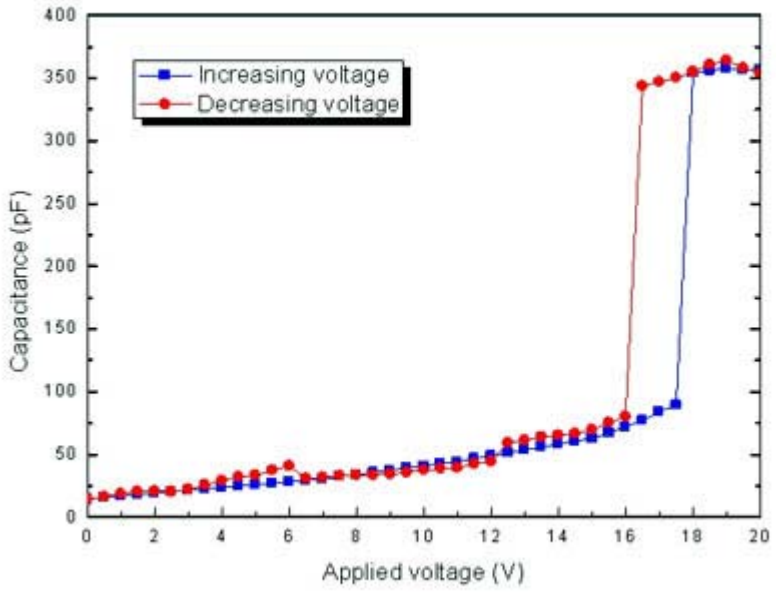

Figure 7-3 Measured capacitance change of the relay during operation

Table 7-1 Characteristics of a fabricated micro-relay

characteristics		Value
Device size	Assembled relay	10×5.6×0.4 mm
	Capacitive plate	2×2×0.15 mm
	Switching connector	2×0.6×0.03 mm
	Initial air-gap	25 μm
Drive voltage		18 V
Contact resistance		0.3 -11.5 Ω
Current capacity		over 5 A
Mechanical life time		over 10^6 cycles
Response time	operation	3.2-3.5 ms
	release	7.9-14.3 ms

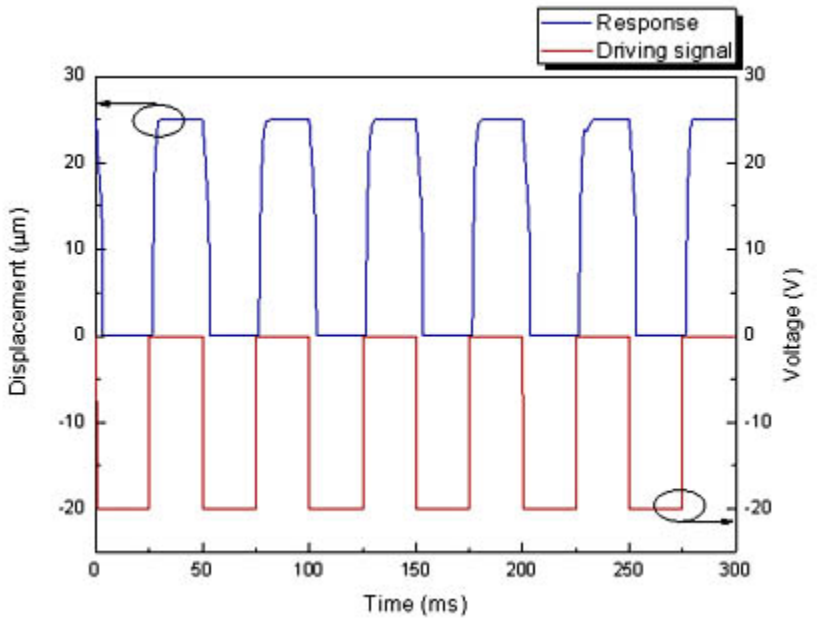

Figure 7-4 Dynamic response of the micro-relay: driven at 20 Hz input frequency

Figure 7-4 shows the dynamic response of a relay for step input at 20 Hz. Since the inverting Op Amp was used to produce VCVS, the negative DC input with 20 V of

amplitude was applied to the device. The response time of a relay was 3.2-3.5 ms during operation while 7.9-14.3 ms during release.

7.3 Micro-accelerometer

Capacitive signal pick-off could be used for accelerometers. The sensing element comprises a seismic mass which can move freely between two electrodes, each forming a capacitor with the seismic mass used as the common center electrode. The differential change in capacitance between the capacitors is proportional to the deflection of the seismic mass from the center position. For the measurement of the differential change in capacitance, the capacitive half-bridge is usually excited with a high frequency signal which is applied to the top electrode and in anti-phase to the bottom electrode; this signal may be a sine or a square wave. Then the magnitude of the signal is proportional to the imbalance of capacitance. However, this is not required to test the prototype accelerometer because the purpose of the device test in this work is to prove the feasibility of the prototype accelerometer and fabrication technology. Instead of that, the capacitance change after a single input signal (amplitude 20 V) was measured to show the dynamic response of an accelerometer [Figure 7-4]. The accelerometer was fabricated using the cured SU-8 as structural material. In order to pick off the output signal (capacitance change), a thin layer of metal film was deposited on the capacitive plates using the Temescal Model BJD-1800 E-Beam Evaporator in CAMD. Immediately after the square wave of input signal, oscillatory motion of seismic mass was shown from which the acceleration could be determined using the capacitive signal pick-off method.

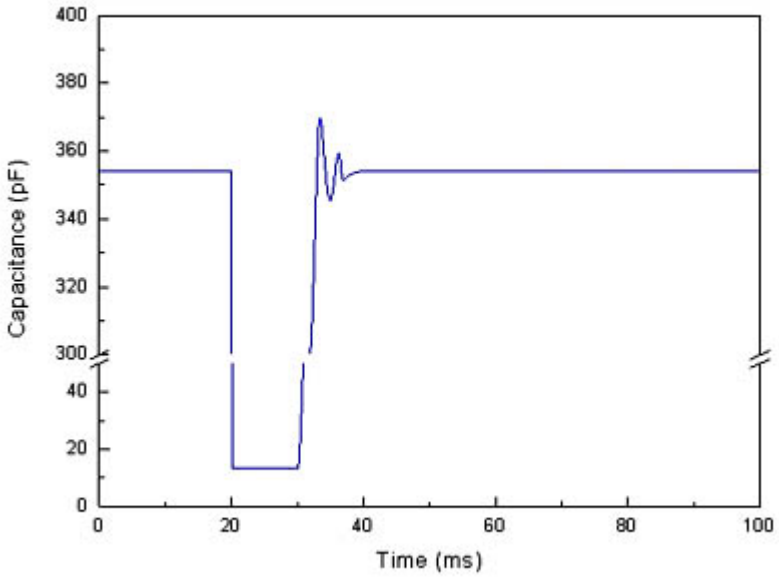

Figure 7-5 Capacitance change of the accelerometer after a square wave of single input signal

CHAPTER 8: CONCLUSIONS AND FUTURE WORKS

8.1 Conclusions

The research work presented in this thesis focused on the development of inertia type electrostatic transducers: the micro-relay and the micro-accelerometer. The work is clearly divided into four sections: design of transducers, static & dynamic analysis of designed transducers, UV-LIGA micro-fabrication technology of transducers, and test technique of transducers. Several different designs of transducers were studied, and unique properties of designed transducers were discussed.

The relay was built with a complete metal structure except two narrow strips of polymer connectors that serve as both mechanical linkages and electrical insulators between the control signal and the circuit to be controlled. A multi-layer, multi-step, hybrid UV-LIGA process has been successfully developed and used to fabricate a prototype relay. It has been demonstrated that the hybrid UV-LIGA process which avoids stripping of the cured SU-8 polymer is the preferred process that offers better fabrication quality and lower fabrication cost. The fabricated relay was operated at 18 V of control voltage with more than 5 A current capacities. The response time of a relay was 3.2-3.5 ms during operation while 7.9-14.3 ms during release.

A prototype accelerometer with very simple structure was also fabricated. Two different approaches were used to fabricate the bottom part of the accelerometer: the separated SU-8 process and the integrated SU-8 process. The integrated SU-8 process can minimize the miss-alignment of top and bottom parts, and potentially provide the precise control of an initial air gap. Because the thickness of the SU-8 resist can be varied in a

large range easily, this provides a very flexible technology to obtain a wide variety of accelerometers for various types of applications, especially for the very low frequency measurement.

8.2 Future Works

Further work would be required to improve the mechanical and electrical properties of transducers. Stiffer springs help to provide very high response speed to the transducer while it may require larger driving force, therefore leading to the increased size of transducers.

More research can be performed to develop the integrated hybrid UV-LIGA process from which an inherent alignment error resulting from the assembling step can be avoided. The gap between the top and bottom capacitive plates may be controlled more precisely by using Cu sacrificial layer. In addition, further development of the UV-LIGA fabrication technology should be performed to improve yields and low reliability concerns. Up to now, yields of the device were less than 10% and a couple of reliability issues were still unsolved.

Finally, the packaging problem should be studied. MEMS are shrinking sensors and actuators into micro and nanometer scales while micro-packaging emerges as the bottleneck for successful device commercialization. MEMS packaging has stringent requirements due to the fragile microstructures, and is generally considered to be the most expensive step in MEMS manufacturing[105]. This is due to one-at-a-time packaging operation using highly specialized production equipment and end-of-line testing and calibration operations. A wide range of efforts for MEMS post-packaging processes has been reported[106, 107, 108]. It is well known that “intimate contact” and “temperature” are

tow major factors for the bonding process, and bonding is the key in device packaging. Intimate contact puts two separated surfaces together, and temperature provides the bonding energy. An innovative bonding approach by localized heating and bonding has also studied. This new approach aims to provide high temperature in a confined region for achieving excellent bonding strength and to keep the temperature low at the wafer-level for preserving MEMS microstructures and microelectronics.

REFERENCES

1 Janusz Bryzek, "Impact of MEMS technology on society," *Sensors and Actuators, A: Physical*, **56**: 1-9 (1996).

2 M. J. Vellekoop, P. M. Sarro, "Technologies for integrated sensors and actuators," *Proceedings of SPIE - The International Society for Optical Engineering*, **3321**, 536-547 (1996)

3 H. Balters, O. Paul, J. G. Korvink, M. Schneider, J. Buhler, N. Schneeberger, D. Jaeggi, P. Malcovati, M. Hornung, A. Haberli, M. von Arx, F. Mayer, J. Funk, "IC MEMS microtransducers," *Technical Digest - International Electron Devices Meeting*, 521-524 (1996).

4 Shuvo Roy, Mehran Mehregany, "Design, fabrication, and characterization of electrostatic microrelays," *Proceedings of SPIE - The International Society for Optical Engineering*, **2642**: 64-73 (1995).

5 Kyu-Yeon Park, Chong-Won Lee, Hyun-Suk Jang, Yongsoo Oh, Byeoungju Ha, "Capacitive type surface-micromachined silicon accelerometer with stiffness tuning capability," *Sensors and Actuators, A: Physical*, **73**: 109-116 (1999).

6 J. M. Hruby, S. K. Griffiths, L. A. Domeier, A. M. Morales, D. R. Boehme, M. A. Bankert, W. D. Bonievert, J. T. Hachman, D. M. Skala, A. Ting, "LIGA: metals, plastics, and ceramics," *Proceedings of SPIE - The International Society for Optical Engineering*, **3874**: 32-43 (1999).

7 K.E. Petersen, "Micromechanical membrane switches on silicon," *Journal of Research and Development*, **23**: 376-385 (1979).

8 M. Mehregany, S. F. Bart, L. S. Tavrow, J. H. Lang, S. D. Senturia, M. F. Schlecht, "A study of three microfabricated variable-capacitance motors," *Sensors and Actuators, A: Physical*, **21**: 173-179 (1990).

9 M.A. Gretillat, P. Thiebaud, C. Linder, N. F. de Rooij, "Integrated circuit compatible electrostatic polysilicon microrelays," *Journal of Micromechanics and Microengineering*, **5**: 156-160 (1995).

10 Kenichiro Suzuki, "Micro electro mechanical systems (MEMS) micro-switches for use in DC, RF, and optical applications," *Japanese Journal of Applied Physics*, **41**: 4335-4339 (2002).

11 J. Bergqvist, F. Rudolf, "A silicon condenser microphone with a highly perforated backplate," *Sensors and Actuators, A: Physical*, **45**: 115-124 (1994).

12 Harrie A. C. Tilmans, Rob Leqtenberg, "Electrostatically driven vacuum-encapsulated polysilicon resonators part II. theory and performance," *Sensors and Actuators, A: Physical*, **45**: 67-84 (1994).

13 Bush Gerry, Don Osborne, "Design and development of a linear thermal actuator," *NASA Conference Publication*, 87-102 (1985).

14 M. J. Zdeblick, J. B. Angell, "Microminiature fluidic amplifier," *Sensors and Actuators*, **15**: 427-433 (1988).

15 Kenji Uchino, "Recent developments in ceramic actuators," *Proceedings of SPIE - The International Society for Optical Engineering*, **3321**: 46-57 (1996)

16 R. M. Moroney, R. M. White, R. T. Howe, "Ultrasonic micromotors: Physics and applications," Proceedings. IEEE Micro Electro Mechanical Systems-An Investigation of Micro Structures, Sensors, Actuators, Machines, 182-187 (1990).

17 Yong-Kweon Kim, Makoto Katsurai, Hiroyuki Fujita, "Fabrication and testing of a micro superconducting actuator using the Meissner effect," *Proceedings. IEEE Micro Electro Mechanical Systems-An Investigation of Micro Structures, Sensors and Actuators, Machines*, 61-66 (1990).

18 Yao, J. Jason, Chang, M. Frank, "Surface micromachined miniature switch for telecommunications applications with signal frequencies from DC up to 4 GHZ," *International Conference on Solid-State, Sensors and Actuators, Proceedings*, **2**: 384-387 (1995).

19 Etsu Hashimoto, Hidenao Tanaka, Yashio Suzuki, Yuji Uenishi, Akinori Watabe, "Thermally controlled magnetization actuator for microrelays," *IEICE Transactions on Electronics*, **E80-C**: 239-245 (1995).

20 Jonathan Simon, Scott Saffer, Chang-Jin Kim, "A micromechanical relay with a thermally-driven mercury micro-drop," *IEEE the Ninth Annual International Workshop on Micro Electro Mechanical System*, 515-520 (1996).

21 B. Rogge, J. Schulz, J. Mohr, A. Thommes, W. Menz, "Fully batch fabricated magnetic microactuators using a two layer LIGA process," *International Conference on Solid-State Sensors and Actuators, Proceedings*, **1**: 320-323 (1995).

22 Hiroshi Hosaka, Hiroki Kuwano, Keiichi Yanagisawa, "Electromagnetic microrelays: concepts and fundamental characteristics," *Sensors and Actuator, A: Physical*, **40**: 41-47 (1994).

23 J. D. Williams, W. Wang, "Microfabrication of an electromagnetic power relay using SU-8 based UV-LIGA technology," *Microsystem Technologies*, **10**: 699-705 (2004).

24 Y. Shacham-Diamand and Y. Sverdlov, "Electrochemically deposited thin film alloys for ULSI and MEMS applications," *Microelectronic engineering*, **50**: 525-531 (2000).

25 V. K. Varadan, V. V. Varadan, "Microsensors, microelectromechanical systems (MEMS), and electronics for smart structures and systems," *Smart Materials and Structures*, **9**: 953-972 (2000).

26 Douglas R. Sparks, Shih-Chia Chang, and David S. Eddy, "Application of MEMS technology in automotive, sensors and actuators," *Proceedings of the International Symposium on Micromechatronics and Human Science*, 9-15 (1998).

27 Greg Freiherr, "Micromachines making headway in medical applications," *Medical Device and Diagnostic Industry*, **19**: 50-52, 54, 56-57 (1997).

28 Mladen Barbic, "Magnetic wires in MEMS and bio-medical applications," *Journal of Magnetism and Magnetic Materials*, **249**: 357-367 (2002).

29 Ryszard J. Pryputniewicz, Cosme Furlong, Emily J. Pryputniewicz, "Design by analysis of a MEMS pressure sensor," *Proceedings of SPIE - The International Society for Optical Engineering*, **4931**: 81-86 (2002).

30 Gerard L. Cote, Ryszard M. Lec, Michael V. Pishko, "Emerging biomedical sensing technologies and their applications," *IEEE Sensors Journal*, **3**: 251-266 (2003).

31 James F. Tressler, Sedat Alkoy, Robert E. Newnham, "Piezoelectric sensors and sensor materials," *Journal of Electroceramics*, **2**: 257-272 (1998).

32 Howard K. Rockstad, T. K. Tang, J. K. Reynolds, T. W. Kenny, W. J. Kaiser, Thomas B. Gabrielson, "A miniature, high-sensitivity, electron tunneling accelerometer," *Sensors and Actuators, A: Physical*, **53**: 227-231 (1996).

33 Norman C. Tien, "Micro-optical inertial sensors using silicon MEMS," *IEEE Aerospace Applications Conference Proceedings*, **1**: 437-443 (1998).

34 Janusz Bryzek, Kurt Petersen, Lee Christel, Farzad Pourahmadi, "New technologies for silicon accelerometers enable automotive applications," *SAE Technical Paper Series*, **920474**: 25-32 (1992).

35 Marc Madou, "Fundamentals of Microfabrication," *CRC Press LLC*, (1996).

36 C. Burbaum, J. Mohr, P. Bley, W. Ehrfeld, "Fabrication of capacitive acceleration sensors by the LIGA technique," *Sensors and Actuators, A: Physical*, **27**: 559-563 (1991).

37 E. J. J. Kruglick, B. A. Warneke, K. S. J. Pister, "CMOS 3-axis accelerometers with integrated amplifier," *Proceedings of the IEEE Micro Electro Mechanical Systems (MEMS)*, 631-636 (1998).

38 J. C. Lotters, J. G. Bomer, A. J. Verloop, E. A. Droog, W. Olthuis, P. H. Veltink, P. Berqveld, "Design, fabrication and characterization of a highly symmetrical capacitive triaxial accelerometer," *Sensors and Actuators, A: Physical*, **66**: 205-212 (1998).

39 Wenming Qu, Christian Wenzel, Gerald Gerlach, "Fabrication of a 3D-differential-capacitive acceleration sensor by UV-LIGA," *Sensors and Actuators, A: Physical*, **77**: 14-20 (1999).

40 Risaku Toda, Nobuo Takeda, Takao Murakoshi, Shigeru Nakamura, Masayoshi Esashi, "Electrostatically levitated spherical 3-axis accelerometer," *Proceedings of the IEEE Mirco Electro Mechanical Systems (MEMS)*, 710-712 (2002).

41 Farrokh Ayazi, Khalil Najafi, "High aspect-ratio dry release poly-silicon MEMS technology for inertial-grade microgyroscopes", *IEEE plans, position location and navigation symposium*, 304-308 (2002).

42 H. Lorenz, M. Despont, N. Fahrni, N. LaBianca, P. Renaud, P. Vettiger, "SU-8: a low-cost negative resist for MEMS," *Journal of Micromechanics and Microengineering*, **7**: 121-124 (1997).

43 M. Shaw, D. Nawrocki, R. Hurditch, D. Johnson, "Improving the process capability of SU-8," *Microsystem Technologies*, **10**: 1-6 (2003).

44 Ru Feng, Richard J. Farris, "Influence of processing conditions on the thermal and mechanical properties of SU8 negative photoresist coatings," *Journal of Micromechanics and Microengineering*, **13**: 80-88 (2003)

45 L. J. Guerin, M. Bossel, M. Demierre, S. Calmes, Ph. Renaud, "Simple and low cost fabrication of embedded micro-channels by using a new thick-film photoplastic," *International Conference on Solid-State Sensors and Actuators, Proceedings*, **2**: 1419-1422 (1997).

46 H. Lorenz, M. Despont, N.Fahrni, J. Brugger, P. Vettiger, P. Renaud, "High-aspect-ratio, ultrathick, negative-tone near-UV photoresist and its applications for MEMS," *Sensors and Actuators, A: Physical*, **64**: 33-39 (1998).

47 Kurt E. Petersen, "Silicon as a mechanical material," *Proceedings of the IEEE*, **70**: 420-457 (1982).

48 Joachim Fruehauf, Eva Gaertner, Erhard Jaensch, "Silicon as a plastic material," *Journal of Micromechanics and Microengineering*, **9**: 305-312 (1999).

49 Donghun Kwak, Jongpal Kim, Sangjun Park, Hyoungho Ko, Dong-il Cho, "Why is (111) silicon a better mechanical material for MEMS: Torsion case," *American Society of Mechanical Engineers, Micro-Electromechanical Systems Division Publication (MEMS)*, **5**: 259-264 (2003).

50 Ewan H. Conradie, David F. Moore, "SU-8 thick photoresist processing as a functional material for MEMS applications," *Journal of Micromechanics and Microengineering*, **12**: 368-374 (2002).

51 A. J. Jacobs-Cook, "MEMS versus MOMS from a systems point of view," *Journal of Micromechanics and Microengineering*, **6**: 148-156 (1996).

52 H. Guckel, T. Earles, J. Klein, J. D. Zook, T. Ohnstein, "Electromagnetic linear actuators with inductive position sensing," *Sensors and Actuators, A: Physical*, **53**: 386-391 (1996).

53 Craig D. Near, "Piezoelectric actuator technology," *Proceedings of SPIE - The International Society for Optical Engineering*, **2717**: 246-258 (1996).

54 W. S. N. Trimmer, "Microrobots and micromechanical systems," *Sensors and Actuators*, **19**: 267-287 (1989).

55 W. S. N. Trimmer, K. J. Gabriel, "Design considerations for practical electrostatic micro-motor," *Sensors and Actuators*, **11**: 189-206 (1987).

56 Dong Yan, Amir Khajepour, Raafat Mansour, "Design and modeling of a MEMS bidirectional vertical thermal actuator," *Journal of Micromechanics and Microengineering*, **14**: 841-850 (2004).

57 Ignaz Schiele, Bernd Hillerich, "Comparison of lateral and vertical switches for application as microrelays," *Journal of Micromechanics and Microengineering*, **9**: 146-150 (1999).

58 Huikai Xie, Gary K. Fedder, "Vertical comb-finger capacitive actuation and sensing for CMOS-MEMS," *Sensors and Actuators, A: Physical*, **95**: 212-221 (2002).

59 Arjun Selvakumar, Khalil Najafi, "Vertical comb array microactuators," *Journal of Microelectromechanical Systems*, **12**: 440-449 (2003).

60 Jongpal Kim, Sanjun Park, Dong-Il Cho, "A novel electrostatic vertical actuator fabricated in one homogeneous silicon wafer using extended SBM technology," *Sensors and Actuators, A*, **97-98**: 653-658 (2002).

61 Gary Keith Fedder, "Simulation of microelectromechanical systems," *PhD Thesis University of Califormia at Berkeley*, 85-86 (1994).

62 A. K. Poddar, K. N. Pandey, "Microwave switch using MEMS-technology," Workshop on High Performance Electron Devices for Microwave and Optoelectronic Applications, EDMO, 134-139 (2000).

63 Catherine Oropeza, Kun Lian, Wanjun Wang, "Fracture toughness study on LIGA fabricated microstructures," *Proceedings of SPIE - The International Society for Optical Engineering*, **4980**: 183-191 (2003).

64 Dong Eun Lee, Hang-Ping Chen, Steve Soper, Wanjun Wang, "An electrochemical micropump and its application in a DNA mixing and analysis system," *Proceedings of SPIE - The International Society for Optical Engineering*, **4982**: 264-271 (2003).

65 Ren Yang, S. J. Jeong, W. Wang, "UV-LIGA microfabrication of a power relay based on electrostatic actuation." *Proceedings of SPIE - The International Society for Optical Engineering*, **4981**: 122-130 (2003).

66 Stephen D. Senturia, "Microsystem design," *Kluwer Academic Publishers*, **3**: (2001).

67 Johnson R. A. "Mechanical filters in electronics," *New York: Wiley*, (1983).

68 Robert C. Juvinall, Kurt M. Marshek, "Fundamentals of machine component design," *John Wiley & sons, Inc.*, **3**: Chap 5 (2000).

69 Sitaraman V. Iyer, Tamal Mukherjee, "Numerical spring models for behavioral simulation of MEMS inertial sensors," *Proceedings of SPIE - The International Society for Optical Engineering*, **4019**: 55-62 (2000).

70 Giuseppe Barillaro, Antonio Molfese, Andrea Nannini, Francesco Pieri, "Analysis, simulation and relative performances of two kinds of serpentine springs," *Journal of Micromechanics and Microengineering*, **15**: 736-746 (2005).

71 Gere J M, Timoshenko S P, "Mechanics of materials," *Chapman and Hall*, **3**: (1991).

72 D. J. Keating and L. Ho, "Effects of squeezed film damping on dynamic finite element analyses of MEMS," *Proceedings of SPIE - The International Society for Optical Engineering*, **4408**: 226-236 (2001).

73 Dorel Homentcovschi, Ronald N. Miles, "Modeling of viscous damping of perforated planar microstructures. Applications in acoustics," *Journal of the Acoustical Society of America*, **116**: 2939-2947 (2004).

74 D. Homentcovschi, R.N. Miles, "Viscous damping of perforated planar microstructures," *Sensors and Actuators, A: Physical*, **119**: 544-552 (2005).

75 Minhang Bao, Heng Yang, Yuancheng Sun, Paddy J French, "Modified Reynolds' equation and analytical analysis of squeeze-film air damping of perforated structures," *Journal of Micromechanics and Microengineering*, **13**: 795-800 (2003).

76 L.A. Rocha, E. Cretu, R.F. Wolffenbuttel, "Full charaterisation of pull-in single-sided clamped beams," *Sensors and Actuators, A*, **110**: 301-309 (2004).

77 L.A. Rocha, E. Cretu, R.F. Wolffenbuttel, "Analysis and analytical modeling of static pull-in with application to MEMS-based voltage reference and process monitoring," *Journal of Microelectromechanical Systems*, **13**: 342-354 (2004).

78 Dominicus J. Ijntema, Harrie A. C. Tilmans, "Static and dynamic aspects of an air-gap capacitor," *Sensors and Actuators, A: Physical*, **35**: 121-128 (1992).

79 R.A. Coutu Jr., P.E. Kladitis, L.A. Starman, J.R. Reid, "A comparison of micro-switch analytic, finite element, and experimental result," *Sensors and Actuators, A: Physical*, **115**: 252-258 (2004).

80 John D. Wiiliams, Ren Yang, Wanjun Wang, "Numerical simulation and test of a UV-LIGA-fabricated electromagnetic micro-relay for power applications," *Sensors and Actuators, A: Physical*, **120**: 154-162 (2005).

81 S. Majumder, N. E. McGruer, G. G. Adams, P. M. Zavracky, R. H. Morrison, J. Krim, "Study of contacts in an electrostatically actuated microswitch," *Sensors and Actuators, A: Physical*, **93**: 19-26 (2001)

82 R. Holm, "Electric contacts, theory and applications," *Springer-Verlag, Berlin*, **4**: (1967).

83 Xavier Lafontan, Francis Pressecq, Guy Perez, Christian Drfaza, Jean-Michel Karam, "Physical and reliability issues in MEMS micro-relays with gold contacts," *Proceedings of SPIE - The International Society for Optical Engineering*, **4558**: 11-21 (2001).

84 Youngjoo Yee, Myoungkyu Park, Kukjin Chun, "A sticking model of suspended polysilicon microstructure including residual stress gradient and postrelease temperature," *Journal of Microelectromechanical Systems*, **7**: 339-344 (1998).

85 C. H. Mastrangelo, C. H. Hsu, "A simple experimental technique for the measurement of the work of adhesion of microstructures," *Technical Digest- IEEE Solid-State Sensor and Actuator Workshop*, 208-212 (1992).

86 Rob Legtenberg, A. C. Tilmans, Job Elders, Miko Elwenspoek, "Stiction of surface micromachined structures after rinsing and drying: model and investigation of adhesion mechanisms," *Sensors and Actuators, A: Physical*, v **43**: 230-238 (1994).

87 Ijaz Jafri, Heinz Busta, Steven Walsh, "Critical point drying and cleaning for MEMS technology," *Proceedings of SPIE - The International Society for Optical Engineering*, **3880**: 51-58 (1999).

88 Rob Leqtenberg, A. C. Tilmans, "Electrostatically driven vacuum-encapsulated polysilicon resonators part I. Design and fabrication," *Sensors and Actuators, A: Physical*, **45**: 57-66 (1994).

89 Ezekiel J. J. Kruglick, "Microrelay design, performance, and systems," *Thesis dissertation, University of California, Berkeley*, (1999).

90 Peter F. van Kessel, Larry J. Hornbeck, Robert E. Meier, Michael R. Douglass, " MEMS-based projection display," *Proceedings of the IEEE*, **86**: 1687-1704 (1998).

91 Gregory T. T. Kovacs, Nadim I. Maluf, Kurt E. Petersen, "Bulk micromachining of silicon," *Proceedings of the IEEE*, **86**: 1536-1551 (1998).

92 Masayoshi Esashi, Susumu Sugiyama, Kyoichi Ikeda, Yuelin Wang, Haruzo Miyashita, "Vacuum-sealed silicon micromachined pressure sensors," *Proceedings of the IEEE*, **86**: 1627-1639 (1998).

93 Thomas Hanemann, Mathias Heckele, Volker Piotter, "Current status of micromolding technology," *Polymer News*, **25**: 224-229 (2000).

94 Chris G. Keller, Roger T. Howe, "Nickel-filled hexsil thermally actuated tweezers," *International Conference on Solid-State Sensors and Actuators, Proceedings*, **2**: 376-379 (1995).

95 John Dukovic, Charles W. Tobias, "Influence of attached bubbles on potential drop and current distribution at gas-evolving electrodes," *Journal of the Electrochemical Society*, **134**: 331-343 (1987).

96 Y. Okinaka, C. Wolowodiuk, "Cyanoaurate(III) formation and its effect on current efficiency in gold plating," *Journal of the Electrochemical Society*, **128**: 288-294 (1981).

97 Y. Okinaka, F. B. Koch, C. Wolowodiuk, D. R. Blessington, "Left double quote polymer right double quote inclusions in cobalt-hardened electroplated gold," *Journal of the Electrochemical Society*, **125**: 1745-1750 (1978).

98 Mordechay Schlesinger, Milan Paunovic, "Modern electroplating," *John Wiley & Sons*, **4**: (2000).

99 Donald W. Baudrand, N. V. Mandich, "Troubleshooting electroplating installations: nickel sulfamate plating system," *Plating and Surface Finishing*, **89**: 68-76 (2002).

100 Y. Tsuru, M. Nomura, F. R. Foulkes, "Effects of boric acid on hydrogen evolution and internal stress in films deposited from a nickel sulfamate bath," *Journal of Applied Electrochemistry*, **32**: 629-634 (2002).

101 T. Saito, E. Sato, M. Matsuoka, C. Iwakura, "Electroless deposition of Ni-B, Co-B and Ni-Co-B alloys using dimethylamineborane as a reducing agent," *Journal of Applied Electrochemistry*, **28**: 559-563 (1998).

102 Daniel C. Harris, "Quantitative chemical analysis," *Freeman*, **5**: Chap.13 (1997).

103 N. V. Mandich, "pH, hydrogen evolution and their significance in electroplating operations," *Plating and Surface Finishing*, **89**: 54-58 (2002)

104 S. Wolf, R. N. Tauber, "Silicon processing for the VLSI era," *Lattic Press*, **1**: 531-532 (1986).

105 C. A. Harper, "Electronic packaging and interconnection handbook," *New York: McGraw-Hill*: (1991).

106 L. Ling, "MEMS post-packaging by localized heating and bonding," *IEEE Transactions on Advanced Packaging*, **23**: 608-616 (2000).

107 Alber K. Hu and Evan D. H. Green, "Packaging of MEMS devices," *Proceedings of SPIE - The International Society for Optical Engineering*, **2642**: 273-280 (1995).

108 G Li, A. A. Tseng, "Low stress packaging of a micromachined accelerometer," *IEEE Transactions on Electronics Packaging Manufacturing*, **24**: 18-25 (2001).

APPENDIX A: ANSYS LOG FILE FOR RELAY SIMULATION

```
/GRA,POWER
/GST,ON
/PLO,INFO,3
/GRO,CURL,ON
/CPLANE,1
WPSTYLE,,,,,,,,0
/REPLOT,RESIZE

!************
!Preferences
!************
/NOPR
/PMETH,OFF,0
KEYW,PR_SET,1
KEYW,PR_STRUC,1
KEYW,PR_THERM,0
KEYW,PR_FLUID,0
KEYW,PR_ELMAG,0
KEYW,MAGNOD,0
KEYW,MAGEDG,0
KEYW,MAGHFE,0
KEYW,MAGELC,0
KEYW,PR_MULTI,0
KEYW,PR_CFD,0
/GO
/COM,
/COM,Preferences for GUI filtering have been set to display:
/COM,  Structural
!*****************
!define parameters
!*****************
```

```
*SET,w,50e-6
*SET,h,2500e-6
*SET,g,200e-6
*SET,t,30e-6

!**************
!element type
!**************
/PREP7
ET,1,SOLID45

!************************
!material properties of Nickel
!******************** *****
MPTEMP,,,,,,,,
MPTEMP,1,0
MPDATA,EX,1,,206.843e9
MPDATA,PRXY,1,,0.31
MPTEMP,,,,,,,,
MPTEMP,1,0
MPDATA,DENS,1,,8.9e3

!********************
!modeling of springs
!********************
RECTNG,0,g,0,-w,        !spring units
RECTNG,g,g+w,0,-h,
RECTNG,g+w,2*g+w,-h,-h+w,
RECTNG,2*g+w,2*g+2*w,-h,0,
FLST,2,4,5,ORDE,2             !add spring units
FITEM,2,1
FITEM,2,-4
AADD,P51X
FLST,3,1,5,ORDE,1             !copy the added spring
```

```
FITEM,3,5
AGEN,2,P51X, , ,2*g+2*w, , , ,0
RECTNG,4*g+4*w,5*g+3*w,0,-w       !final spring part
RECTNG,5*g+3*w,5*g+4*w,0,-w
FLST,2,4,5,ORDE,3             !complete spring by adding
FITEM,2,1
FITEM,2,-3
FITEM,2,5
AADD,P51X
FLST,2,1,5,ORDE,1             !extrude
FITEM,2,4
VEXT,P51X, , ,0,0,t,,,,

!********************
!meshing
!********************
SMRT,6
MSHAPE,1,3D
MSHKEY,0
CM,_Y,VOLU
VSEL, , , ,       1
CM,_Y1,VOLU
CHKMSH,'VOLU'
CMSEL,S,_Y
VMESH,_Y1
CMDELE,_Y
CMDELE,_Y1
CMDELE,_Y2

***************
confine the area
***************
/SOL
FLST,2,1,5,ORDE,1
```

```
FITEM,2,9
/GO
DA,P51X,ALL,0

**********
Apply load and solve
**********
FLST,2,1,1,ORDE,1
FITEM,2,32
/GO
F,P51X,FZ,-0.0001
! /STATUS,SOLU
SOLVE
```

APPENDIX B: MATLAB CODE FOR THE DYNAMIC RESPONSE OF ACCELEROMETER

```
%--------------------------------------------------------------------------
%   File Name: HarmonicVib1DOF.m
%   Objective:  Response of the system
%   Usage:    [t,x]=HarmonicVib1DOF(xtime,xinitial,F0,w,m,c,k)
%--------------------------------------------------------------------------

function [t,x]=HarmonicVib1DOF(xtime,xinitial,F0,w,m,c,k)

% Caculation: Natural frequency, damping ratio
Wn=sqrt(k/m)
Cc=2*m*Wn
Zeta=c/Cc
Wd=sqrt(1-Zeta^2)*Wn;
r=w/Wn;
delta=F0/k;
Phi=atan((2*Zeta*r)/(1-r^2));
X=delta/sqrt((1-r^2)^2+(2*Zeta*r)^2);

% Initial condition
xd0=xinitial(1);
x0=xinitial(2);

% Simulation time
t0=xtime(1);
tf=xtime(2);
step=(tf-t0)/100;
t=t0:step:tf;
```

```
% underdamped
if(Zeta>0 & Zeta<1)
   A1=x0;
   B1=(xd0+Zeta*Wn*x0)/Wd;
   x=exp(-Zeta*Wn.*t).*(A1*cos(Wd*t)+B1*sin(Wd*t))+X*sin(w*t-Phi);

% critical damped
elseif(Zeta==1)
   A2=x0;
   B2=(xd0+Wn*x0);
   x=A2*exp(-Wn.*t)+B2*t.*exp(-Wn.*t)+X*sin(w*t-Phi);

% overdamped
else(Zeta>1)
   A3=(xd0+(Zeta+sqrt(Zeta^2-1))*Wn*x0)/(2*sqrt(Zeta^2-1)*Wn);
   B3=(-xd0-(Zeta-sqrt(Zeta^2-1))*Wn*x0)/(2*sqrt(Zeta^2-1)*Wn);
   x=A3*exp((-Zeta+sqrt(Zeta^2-1))*Wn*t)+B3*exp((-Zeta-sqrt(Zeta^2-
1))*Wn*t)+X*sin(w*t-Phi);
end

% velocity
dx=diff(x)./diff(t);
dt=t(2:length(t));

% acceleration
% ddx=diff(dx)./diff(dt);
% ddt=t(2:length(dt));
% Magnification factor
Magnification_factor=1/sqrt((1-r^2)^2+(2*Zeta*r)^2);
R=0:0.001:3;
X_delta=1./sqrt((1-R.^2).^2+(2.*Zeta.*R).^2);
```

```
% Phase angle
if(r<1)
   Phase_angle=atan((2*Zeta*r)/(1-r^2))*(180/pi);
elseif(r>1)
   Phase_angle=atan((2*Zeta*r)/(1-r^2))*(180/pi)+180;
end
R1=0:0.001:0.999;
Phase1=atan((2*Zeta*R1)./(1-R1.^2));
R2=1.0001:0.001:3;
Phase2=atan((2*Zeta*R2)./(1-R2.^2));
R3=[R1,R2];
Phase1=Phase1.*(180/pi);
Phase2=Phase2.*(180/pi)+180;
Phase3=[Phase1,Phase2];

subplot(2,2,1);
plot(t,x);
xlabel('t');
ylabel('Displacement');
subplot(2,2,2);
plot(dt,dx);
xlabel('t');
ylabel('Velocity');
subplot(2,2,3);
plot(R,X_delta,'r',r,Magnification_factor,'bo');
xlabel('r');
ylabel('M');
subplot(2,2,4);
plot(R3,Phase3,'r',r,Phase_angle,'bo');
xlabel('r');
ylabel('Phi');
```

APPENDIX C: SU-8 PROCESSING DATA

C.1 Spin Coating Process

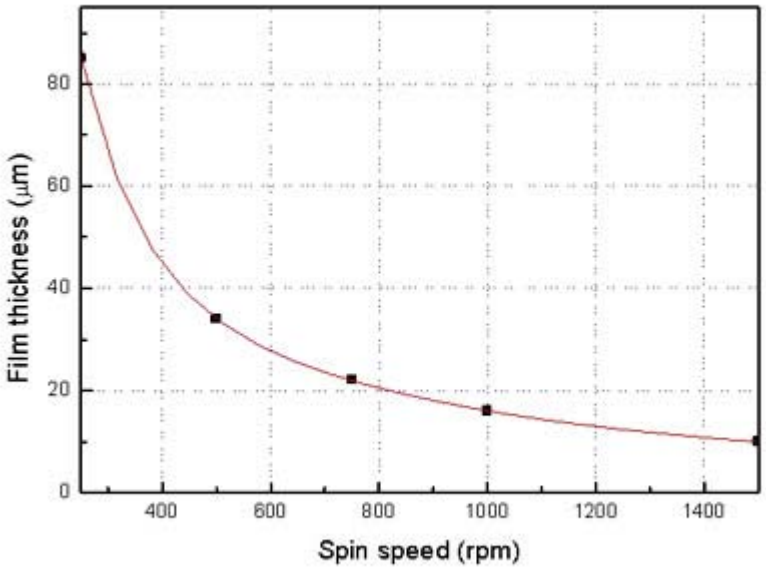

Figure A-1 Figure Spin speed vs. thickness curves for SU-8 5

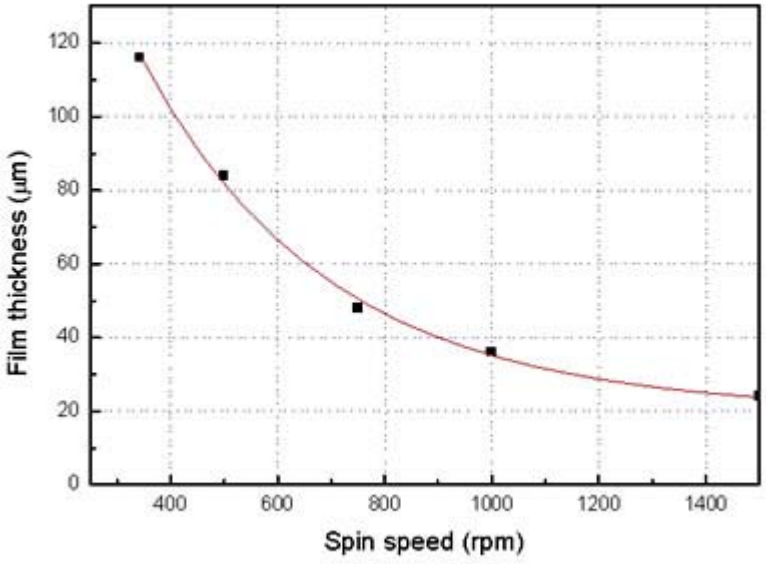

Figure A-2 Spin speed vs. thickness curves for SU-8 10

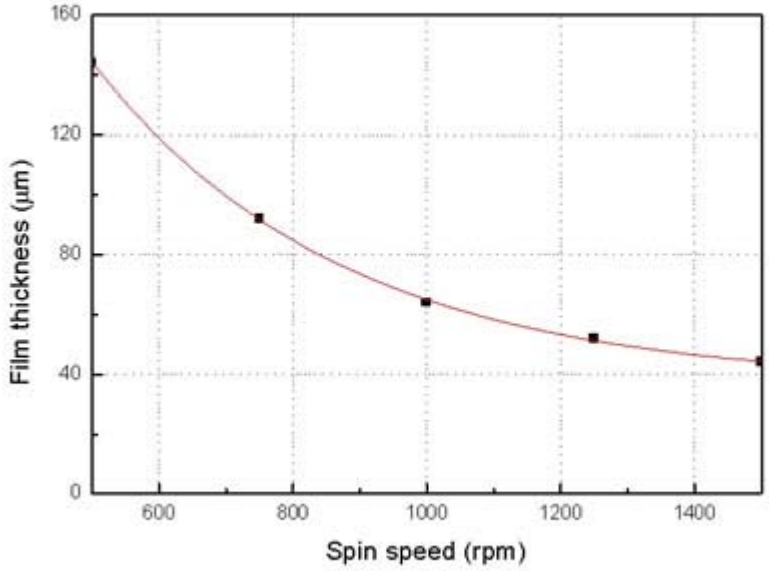

Figure A-3 Spin speed vs. thickness curves for SU-8 25

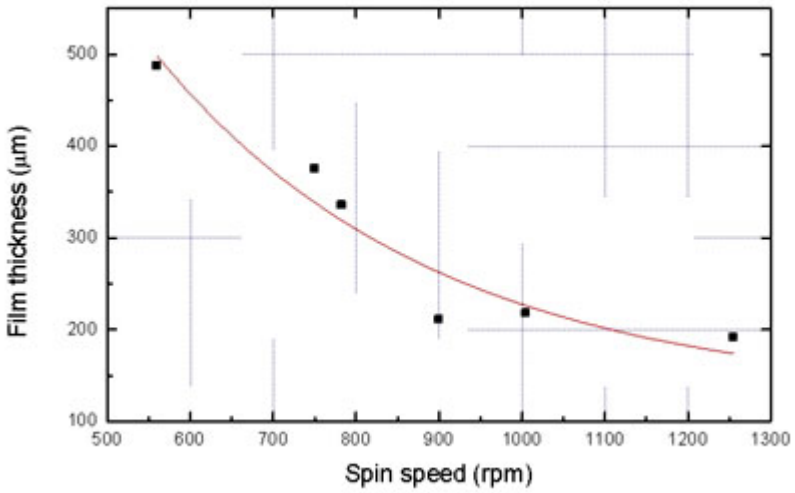

Figure A-4 Spin speed vs. thickness curves for SU-8 50

C.2 Soft Bake Process

Table A-1 Recommended soft bake process [MicroChem Inc.]

Product	Thickness (μm)	Soft Bake Time (m: minute)	
		Step 1: 65 °C	Step 2: 95 °C
SU-8 5	5	1 m	3 m
	7	2 m	5 m
	15	2 m	5 m
SU-8 10	10	2 m	5 m
	15	2 m	5 m
	30	2 m	7 m
SU-8 25	15	2 m	5 m
	25	3 m	7 m
	40	5 m	15 m
SU-8 50	40	5 m	15 m
	50	6 m	20 m
	100	10 m	30 m

C.3 Exposure Process

Table A-2 Exposure dose versus thickness [CAMD]

Thickness (μm)	Dose (mJ/cm^2)	Thickness (μm)	Dose (mJ/cm^2)	Thickness (μm)	Dose (mJ/cm^2)
10	210	240	900	520	1740
20	240	260	960	540	1800
40	300	280	1020	560	1860
50	330	300	1080	580	1920
60	360	320	1140	600	1980
70	390	340	1200	620	2040
90	450	360	1260	640	2100
100	480	380	1320	660	2160
140	600	400	1380	680	2220
160	660	420	1440	700	2280
180	720	460	1560	740	2400
200	780	480	1620	770	2490
220	840	500	1680	800	2580

C.4 Post-exposure Bake

Table A-3 Recommended PEB process [McroChem Inc.]

Product	Thickness (μm)	Soft Bake Time (m: minute)	
		Step 1: 65 °C	Step 2: 95 °C
SU-8 5	5	1 m	1 m
	7	1 m	1 m
	15	1 m	2 m
SU-8 10	10	1 m	2 m
	15	1 m	2 m
	30	1 m	3 m
SU-8 25	15	1 m	2 m
	25	1 m	3 m
	40	2 m	4 m
SU-8 50	40	2 m	4 m
	50	2 m	5 m
	100	3 m	10 m

APPENDIX D: NICKEL PLATING BATH

Table A-4 Nickel sulfamate solution

	Nickel sulfamate solution	
	1 liter base	6 liter base
$Ni(SO_3NH_2)_2$ (Nickel Sulfamate)	0.45 L	2.75 L
$NiCl_2 \cdot 6H_2O$ (Nickel Chloride)	2 g	12 g
$B(OH)_3$ (Boric Acid)	37.5 g	225 g
$CH_3(CH_2)_{11}OSO_3Na$ (Sodium Lauryl Sulfate)	1 g	6 g
Temperature	56-57 ℃	
Agitation rate	200 rpm	
pH	3.9-4.1	
Current density	20-50 mA/cm^2	
Deposition rate	10-85 μm/hr	

Starting up a new plating bath (sulfamate solution):

i. Put 2 liters of DI water in the plating tank first, and then add 2.75 liters of nickel sulfamate solution; put the plating tank in water bath at 60℃ with stirring.

ii. Add 18 g of nickel chloride and 6 g of sodium lauryl sulfate; allow it to settle down for 2 hours.

iii. When all solids have dissolved, the solution needs to be filtered using first a 5 μm filter and then 1.6 μm filter.

iv. Add and dissolve 225 g of boric acid; add DI water to bring the tank up to 6 liters.

v. Electrically purify by using a large area of nickel-plated corrugated steel sheet as cathode. The average cathode current density should be 0.5 A/dm^2 and treatment should continue until 0.5-1.5 A-h/liter (6-8 hours) have passed through the solution. The solution should be agitated and the temperature held at 49-60℃. Prepared deposits at normal current densities at some point to check appearance, stress, and sulfur content; if not acceptable, continue the electrolytic purification until the properties are acceptable.

vi. Remove the dummy cathodes and adjust pH 3.5-4.5 by controlling sulfuric acid or hydrochloric acid.

APPENDIX E: TITRATION METHODS OF NICKEL AND BORIC ACID

E.1 Titration of Nickel Ions by EDTA Method

Supplies:

- Erlenmeyer flask 250 ml wide neck
- Measuring cylinder 250 ml
- Volumetric flask 100 ml with stopper
- Measuring pipette 20 ml and 10 ml
- Burette 50 ml
- Pipette ball
- Spatula

Chemicals:

- Murexide (item#: 17865 in Alfa Aesar) 5 g
- Ammonium hydroxide, 25% NH_3 (item#: 87903) 250 ml
- Ethylenediaminetetraacetic acid (EDTA), disodium salt, 0.100N (0.050 M) Standardized solution. (item#: 39781)
- DI water

Preparation:

i. Ensure that all units used are clean and dry

ii. Fill the burette with EDTA

Operation:

i. Fill the measuring cylinder with 20 ml electrolyte by using the 20 ml measuring pipette, and add 200 ml DI water which corresponds to 1:10 dilution.

ii. Close the measuring cylinder with the stopper and thoroughly mix DI water and electrolyte.

iii. Fill the 100 ml volumetric flask with 10 ml diluted electrolyte by using the 10ml measuring pipette.

iv. Add 10 ml ammonia solution, and then the color will change from green to blue.

v. Add DI water to bring the 100 ml volumetric flask up to the 100 ml mark.

vi. Pour the solution in the 100 ml volumetric flask into Erlenmeyer flask.

vii. Add a spatula tip of Murexide indicator and agitate thoroughly by using a magnetic bar, and then color will change from blue to yellowish green.

viii. Drain a little amount of the solution in the burette in order to eliminate any air bubbles.

ix. Note down the amount of EDTA in the burette.

x. Drop the EDTA into the Erlenmeyer flask with stirring until the color changes from yellowish-brown to violet.

xi. Note down the amount of the used EDTA.

xii. Calculate the required amount of Ni from the used DETA.

Reaction	Ni^{2+}	+	EDTA	↔	NiY^{2-}
Used volume	1 ml		V_{EDTA} ml		
Moles	$\frac{W_{Ni}}{MW_{Ni}}$		0.05 M		

The required amount of Ni: $W_{Ni} = 0.05 \times MW_{Ni} \times V_{EDTA} = 2.935 \times V_{EDTA}$ $[g/l]$

Making addition:

The nickel and chloride concentrations are replenished by adding the appropriate nickel salts. Table A-5 lists conversion factors for nickel salts.

Table A-5 Nickel content of nickel salts

	Symbol	Ni
	Atomic weight	58.69
	Valency	2
	Specific gravity	8.90
Nickel Sulfate	$NiSO_4 \cdot 6H_2O$	Contains 22.3% nickel
Nickel Sulfamate	$Ni(SO_3NH_2)_2$	Contains 23.2% nickel
Nickel Chloride	$NiCl_2 \cdot 6H_2O$	Contains 24.7% nickel

It is preferable to pre-dissolve all solids in a separate mixing tank and to filter this solution into the main plating tank to avoid roughness problems. If this is not possible, additions can be made directly into the plating tank in small increments when the bath is not loaded. The solution will then require through stirring and filtering before recommencing production. Liquid additions can be added directly to the plating tank, but should be distributed as evenly as possible. Sulfuric acid for pH adjustment should be diluted before addition to assist in dispersion and to prevent possible oxidation of organic addition agents.

E.2 Titration of Boric Acid (H_3BO_3)

Supplies:

- D-Mannitol, ACS (item#: 33342)
- Erlenmeyer flask 250 ml, wide neck

- Measuring flask 200 ml, with stopper
- Pipette 20 ml
- Burette 25 ml
- Pipette ball
- Spoon

Chemicals:

- D-Mannitol, ACS, 99.0 % min (item#: 33342)
- Bromocresol green, sodium salt, 0.04% w/v aqueous solution (item#: 38696)
- Sodium hydroxide solution (NaOH), 0.1 N standardized solution (item#: 35625)
- DI water

Preparation:

i. Ensure that all units used are clean and dry.

ii. Fill the burette with sodium hydroxide.

Operation:

i. Fill the measuring cylinder with 20ml electrolyte by using the 20ml measuring pipette, and add 200ml DI water which corresponds to 1:10 dilution.

ii. Close the measuring cylinder with the stopper and thoroughly mix DI water and electrolyte.

iii. Fill the Erlenmeyer flask with 20ml diluted electrolyte by using the 20ml measuring pipette.

iv. Add about 5 teaspoons of D-Mannitol with agitating; settle down for a while and then D-Mannitol is added until the solution is saturated.

v. Add 4 drops of Bromocresol green solution; agitate thoroughly.

vi. Drain a little amount of the solution in the burette in order to eliminate any air bubbles.

xiii. Note down the amount of sodium hydroxide in the burette.

xiv. Drop sodium hydroxide into the Erlenmeyer flask with stirring until the color changes from green to blue.

xv. Note down the amount of the used sodium hydroxide.

vii. Calculate the required amount of boric acid from the used sodium hydroxide.

Reaction	$B(OH)_3$	+	NaOH	↔	BO_3H_5Na
Used volume	1 ml		V_{NaOH} ml		
Moles	$\frac{W_{Boric\ acid}}{MW_{Boric\ acid}}$		0.1 N		

The required amount of boric acid:

$$W_{Boric\ acid} = \frac{1}{2} \times 0.1 \times MW_{Boric\ acid} \times V_{NaOH} = 3.09 \times V_{NaOH} \quad [g/l]$$

For making the addition of boric acid, refer to the titration of nickel.

APPENDIX F: SPR-220 PROCESS

F.1 Spin Coating

i. Clean the substrate with acetone, IPA and DI water (long rinse); dehydration bake @ 120° C for 1/2 hour (convection oven)

ii. Spin-coat for 30 sec (See the Table A-6 and the graph to see the detail information)

iii. Remove the edge bead with a wipe (use a small piece of wipe for this)

iv. Let the wafer sit for 1/2 hour to allow the resist to relax

v. Bake cycle - put into oven @ 95° C for 1 min 30 sec and then hot plate @ 115° C for 2 min.

vi. Let the sample sit for about 1 hour

Table A-6 Thickness versus exposure dose

Photoresist	Thickness (μm)	Spin speed (rpm)	Photospeed (mJ/cm^2)
SPR 220-3	2.4	4000 × 1	80
	2.8	3000 × 1	105
	3.3	2000 × 1	130
	5.1	1000 × 1	210
SPR 220-7	9.5	2000 × 1	400
	13.0	1150 × 1	560
	23	2000 × 2	1000
	32	1500 × 2	1400
	36	1500 + 1000	1580
	43	1000 × 2	1900

F.2 Exposure

i. Expose using Quintel in vacuum mode

ii. See Table A-6 for the relationship between dose and thickness

iii. Let relax after exposure for at least 30 min

F.3 Development

By 50% MF-322 + 50% MF 321 developer

i. Use 2 baths of 50% MF-322 + 50% MF 321 developer

ii. 2 min in first bath (used developer can be used). Agitate mildly by moving the developer tray

iii. 2 min in second bath (fresh developer). While in this bath stop development soon after red clouds of resist stop coming off the wafer.

iv. Rinse in DI water

By PD523 AD developer

i Use 2 baths of PD523 AD developer

ii In the first bath (used developer can be used), agitate mildly by moving the developer tray

iii In the second bath (fresh developer), while in this bath stop development soon after red clouds of resist stop coming off the wafer.

iv Rinse in DI water

By MF84 MX developer

i Use 2 baths of MF84 MX developer

ii In the first bath (used developer can be used), agitate mildly by moving the developer tray

iii In the second bath (fresh developer), while in this bath stop development soon after red clouds of resist stop coming off the wafer.

iv Rinse in DI water

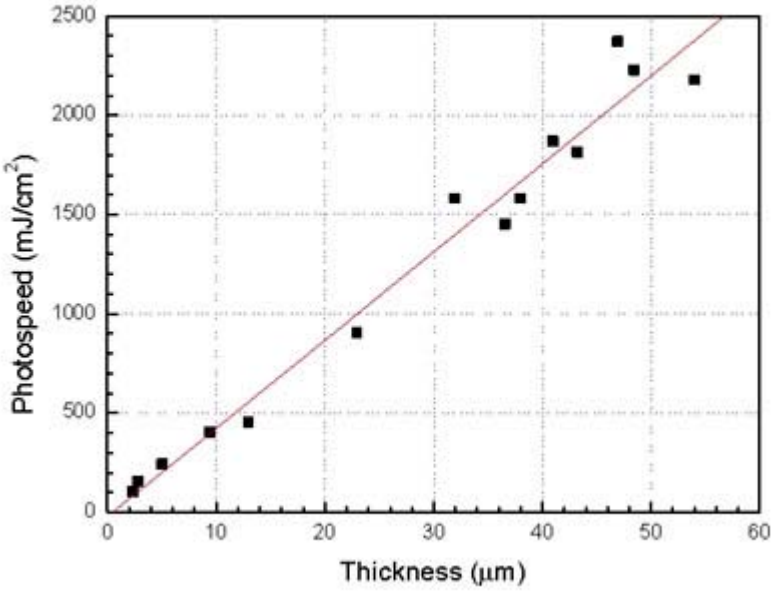

Figure A-5 Photospeed vs. thickness curve for SPR220-7

APPENDIX G: SC1827 PROCESS

G.1 Spin Coating

i Clean the substrate with acetone, IPA and DI water (long rinse); dehydration bake @ 120° C for 1/2 hour (convection oven)

ii Spin-coat for 30 sec (2.5 μm)

iii Let the wafer sit for 10 min to allow the resist to relax

iv Bake cycle - put into hot plate @ 95° C for 1.5 min.

v Let the sample sit for about 1/2 hour

G.2 Exposure

i Expose 100mJ/cm^2 using Quintel in vacuum mode

ii See the data sheet for the relationship between dose and thickness

Let relax after exposure for at least 30 min

G.3 Development by Microposit 354 Developer or PD523 AD

i Use 2 baths of Microposit 354 developer

ii 2 min in first bath (used developer can be used). Agitate mildly by moving the developer tray

iii 2 min in second bath (fresh developer). While in this bath stop development soon after red clouds of resist stop coming off the wafer.

iv Rinse in DI water

VITA

Seok Jae Jeong was born on August 26th, 1970, in Sangju, South Korea. He received the degree of Bachelor in Chemical Engineering in January of 1997 and the degree of Master in Chemical Engineering in January of 1999 from Sungkyunkwan University in Suwon, South Korea. In the fall of 2000, he entered Louisiana State University (LSU) in Baton Rouge. In August 2001 he joined the graduate program in mechanical engineering at Louisiana State University as a member of the Microsystems Engineering Team (μSET). He expects to receive the degree of Doctor of Philosophy in mechanical engineering in May 2006.